Methods and good practice guidelines for human joint kinematics estimation through magnetic and inertial wearable sensors

Thesis · July 2022

CITATIONS
0

READS
224

1 author:

Marco Caruso
Politecnico di Torino
60 PUBLICATIONS **377** CITATIONS

SEE PROFILE

Doctoral Dissertation
Doctoral Program in Bioengineering and Medical Surgical Sciences (34th Cycle)

Methods and good practice guidelines for human joint kinematics estimation through magnetic and inertial wearable sensors

By

Marco Caruso

Supervisors:
Prof. Marco. Knaflitz, Supervisor
Prof. Marco. Gazzoni, Supervisor
Prof. Andrea. Cereatti, Co-Supervisor

Doctoral Examination Committee:
Prof. Andrea Mannini, Referee, Fondazione Don Gnocchi
Prof. Raphael Dumas, Referee, Université de Lyon

Politecnico di Torino
2022

Declaration

I hereby declare that, the contents and organization of this dissertation constitute my own original work and does not compromise in any way the rights of third parties, including those relating to the security of personal data.

Marco Caruso

2022

* This dissertation is presented in partial fulfillment of the requirements for **Ph.D. degree** in the Graduate School of Politecnico di Torino (ScuDo).

Ai miei nonni Michele e Fifina che mi ascoltano da "remoto"

Alla mia mamma, al mio papà, alla mia nonna Marisa, alla mia famiglia
alla mia Dajana, ai miei amici di una vita

Abstract

According to the World Health Organization, the ability to move is recognized as a key factor for the human well-being. From the wearable Magnetic and Inertial Measurement Units (MIMUs) signals it is possible to extract several digital mobility outcomes including the joint kinematics. To this end, it is first required to estimate the orientation of the MIMUs by means of a sensor fusion algorithm (SFA). After that, the relative orientation is computed and then decomposed to obtain the joint angles. However, the MIMUs do not provide a direct output of the physical quantity of interest which can be only determined after an *ad hoc* processing of their signals. It follows that the joint angle accuracy mostly depends on multiple factors. The first one is the magnitude of the MIMU measurements errors and up to date there is still a lack of methods for their characterization. A second crucial factor is the choice of the SFA to use. Despite the abundance of formulations in the literature, no-well established conclusions about their accuracy have been reached yet. The last factor is the biomechanical model used to compute the joint angles. In this context, unconstrained methods offer a simple way to decompose the relative orientation using the Euler angles but suffer from the inherent issues related to the SFA. In contrast, constrained approaches aim at increasing the robustness of the estimates by adopting models in which an objective function is minimized through the definition of physiological constraints.

This thesis proposed the methods to accurately estimate the human joint kinematics starting from the MIMU signals. Three main contributions were provided. The first consisted in the design of a comprehensive battery of tests to completely characterize the sources of errors affecting the quality of the measurements. These tests rely on simple hypotheses based on the sensor working principles and do not require expensive equipment. Nine parameters were defined to quantify the signal accuracy improvements (if any) of 24 MIMUs before and after the refinement of their calibration coefficients. The second contribution was focused on the SFAs. Ten among the most popular SFAs were compared under different experimental conditions including different MIMU models and rotation rate magnitudes. To perform a “fair” comparison it was necessary to set the optimal parameter values for each SFA. The most important finding was that all the errors fall within a range from 3.8 deg to 7.1 deg thus making it impossible to

draw any conclusions about the best performing SFA since no statistically significant differences were found. In addition, the orientation accuracy was heavily influenced by the experimental variables. After that, a novel method was designed to estimate the suboptimal parameter values of a given SFA without relying on any orientation reference. The maximum difference between the errors obtained using optimal and suboptimal parameter values amounted to 3.7 deg and to 0.6 deg on average. The last contribution consisted in the design of an unconstrained and a constrained methods for estimating the joint kinematics without considering the magnetometer to avoid the ferromagnetic disturbances. The unconstrained method was employed in a telerehabilitation platform in which the joint angles were estimated in real time. Errors collected during the execution of a full-body protocol were lower than 5 deg (considered the acceptability threshold). However, this method may be inaccurate after few minutes since no solutions can be taken to mitigate the drift error. To overcome this limitation a constrained method was developed based on a robotic model of the upper limb to set appropriate constraints. Errors relative to a continuous robot motion for twenty minutes were lower than 3 deg at most suggesting the feasibility of employing these solutions in the rehabilitation programs to properly plan the treatment and to accurately evaluate the outcomes.

Contents

List of acronyms

Anatomical Coordinate System	ACS
Acceleration Random Walk	AcRW
Allan Deviation	ADEV
Angle Random Walk	ARW
Complementary Filter	CF
Denavit-Hartenberg	DH
Degree of Freedom	DoF
Forearm	FA
Global Coordinate System	GCS
Kalman filter from Guo *et al.*	GUO
Interquartile range	IQR
International Society of Biomechanics	ISB
Kalman Filter	KF
Local Coordinate system	LCS
Kalman filter from Ligorio *et al.*	LIG
Complementary filter from Madgwick *et al.*	MAD
Complementary filter from Mahony *et al.*	MAH
Kalman filter from MATLAB	MAK
Complementary filter from MATLAB	MCF
Magneto-Inertial Measurement Unit	MIMU
Rigid Constraint Method	RCM
Root Mean Square	RMS
Range of Motion	ROM
Rate Random Walk	RRW
Kalman filter from Sabatini	SAB
Complementary filter from Seel *et al.*	SEL
Sensor Fusion Algorithm (Filter)	SFA
Stereophotogrammetric system	SP
Standard Deviation	STD
Trunk	TR
Upper arm	UA
Complementary filter from Valenti *et al.*	VAC
Kalman filter from Valenti *et al.*	VAK
Velocity Random Walk	VRW

Chapter 1

Clinical relevance and general introduction

1.1 The importance of the human motion monitoring

In the new millennium, the World Health Organization has included the ability to move as a key factor for the human mental and physical well-being (World Health Organization, 2005). However, the ageing of the population is typically associated to a loss of mobility and therefore of lack of independency with a remarkable personal and society impact, also from an economic point of view (Mazzà et al., 2021). Instrumented movement analysis plays an important role for quantitatively assessing the mobility level and it represents a powerful tool for the early detection of pathologies before the onset of the main debilitating symptoms (Perera et al., 2016; Studenski et al., 2011). Moreover, real-time and accurate estimation of the upper and lower limb joint kinematics is required to develop home-based telerehabilitation applications which can have a positive impact for a better and more equal health care (Zedda et al., 2020).

At the current stage, the optical stereophotogrammetry is considered the reference for instrumented movement analysis due to its submillimeter accuracy in tracking the position of some markers attached to subject's skin and a high temporal resolution up to milliseconds. However, despite accurate, this technology is very costly, requires expert operators, specialized laboratories, and long-time patients' preparation, but, above all, limits the subject's movement in a

small capture volume. Recent literature has shown that stereophotogrammetry measurements, although useful to assess the mobility capacity, may not be representative of the mobility performance of people during daily life conditions (Brodie et al., 2017; Storm et al., 2018).

Miniaturized Magnetic and Inertial Measurement Units (MIMUs) have been increasingly employed in the movement analysis practice by leading the transition from the laboratory-based assessment to an unconstrained monitoring. The main key features are their relative low-cost, ease of use, and, most importantly, their wearability. From the accelerometer, gyroscope, and magnetometer signals it is possible to extract several digital mobility outcomes. In particular, joint angles can be obtained from the orientation of the MIMUs attached to the proximal and distal segments of the joint under analysis. To this purpose, it is first required to estimate MIMUs orientation by means of a sensor fusion algorithm which combines the complementary information of the MIMU measurements. After that, the relative orientation is computed and then decomposed based on an appropriate biomechanical model to obtain the joint angles. Some of the abovementioned operations can be also directly performed by the microcontrollers embedded in the MIMUs thus allowing the real-time tracking of the movement. Nonetheless, their employment is not without limitations. One of the most evident issues consists in the fact that the MIMUs do not provide a direct measurement of the physical quantity of interest which can be only obtained after a proper processing of the MIMU information. It follows that the accuracy of the final joint angle estimates mostly depends on multiple factors. The first one is represented by the quality of the MIMU measurements which may differ across the MIMU devices of different models available on the market (Grewal et al., 2007) and are in general up to three orders of magnitude inferior to those sensors employed for military, marine, and missile applications (Yazdi et al., 1998). Several procedures to refine the calibration coefficients of each sensor have been proposed in the literature over the years, but there is still a lack of methods to characterize the magnitude of the errors. A second crucial factor is the choice of the sensor fusion algorithm to use. Despite the abundance of formulations in the literature, no-well established conclusions about the accuracy and the best performing algorithm have been reached yet (Bergamini et al., 2014). The last important factor is the biomechanical model used to compute the joint angles starting from the orientation of the proximal and distal segments to the joint under analysis. In general, it is possible to group the kinematic methods in two categories based on the use of joint constraints. Unconstrained methods offer a simple way to

decompose the relative orientation into the joint angles of interest but suffer from the inherent issues related to the sensor fusion such as the orientation drift, linear acceleration, and ferromagnetic disturbances. Constrained approaches are designed to increase the robustness of the estimates by adopting a more complex model in which an objective function is minimized through the definition of physiological constraints in an optimization framework.

1.2 Aim of this thesis

The goal of this thesis is to provide the methods and the good practice guidelines to deal with each of the three above-mentioned factors involved. In particular, the manuscript organization follow a bottom-up approach as detailed below and graphically represented in Figure 1:

- In the second chapter the main sources of measurement errors affecting each type of sensor reading embedded in a MIMU are discussed and then characterized through a battery of *ad hoc* designed tests which do not require any specialized laboratories and can be conducted using simple equipment. These characterization tests were then applied to a set of 24 MIMUs to provide evidence of their effectiveness.
- In the third chapter, ten among the most popular sensor fusion algorithms are implemented and tested under optimal conditions to enable a meaningful and "fair" comparison. This means that the parameter values of each filter have been optimally set to minimize the difference from the gold standard orientation (best case scenario). Since the optimal tuning approach is not practicable outside the laboratory, in the second part of this chapter a novel heuristic method is designed to estimate the most suitable parameter values of each sensor fusion filter without relying on any orientation reference. This method exploits the rigid body assumption and it was validated using the same ten algorithms employed for the comparison.
- In the fourth chapter, the joint kinematics estimated using an unconstrained method was employed in a telerehabilitation platform conceived for stroke patients (DoMoMEA) to estimate a full-body joint kinematics. The joint angles estimated in real time are used both to animate the exergames and to provide feedback to correct the compensatory movements. The preliminary results obtained during a

validation session are then shown and discussed. Then, a constrained method exploiting a biomechanical model of the upper limb was designed to estimate the shoulder and elbow angles. This method allows the definition of physiological constraints to set the angular limit for each joint range and to restrict the maximum angular variation between two consecutive time steps. Model validity was assessed on both synthetic and robotic data over twenty-minute length acquisitions to test its robustness to the orientation drift.

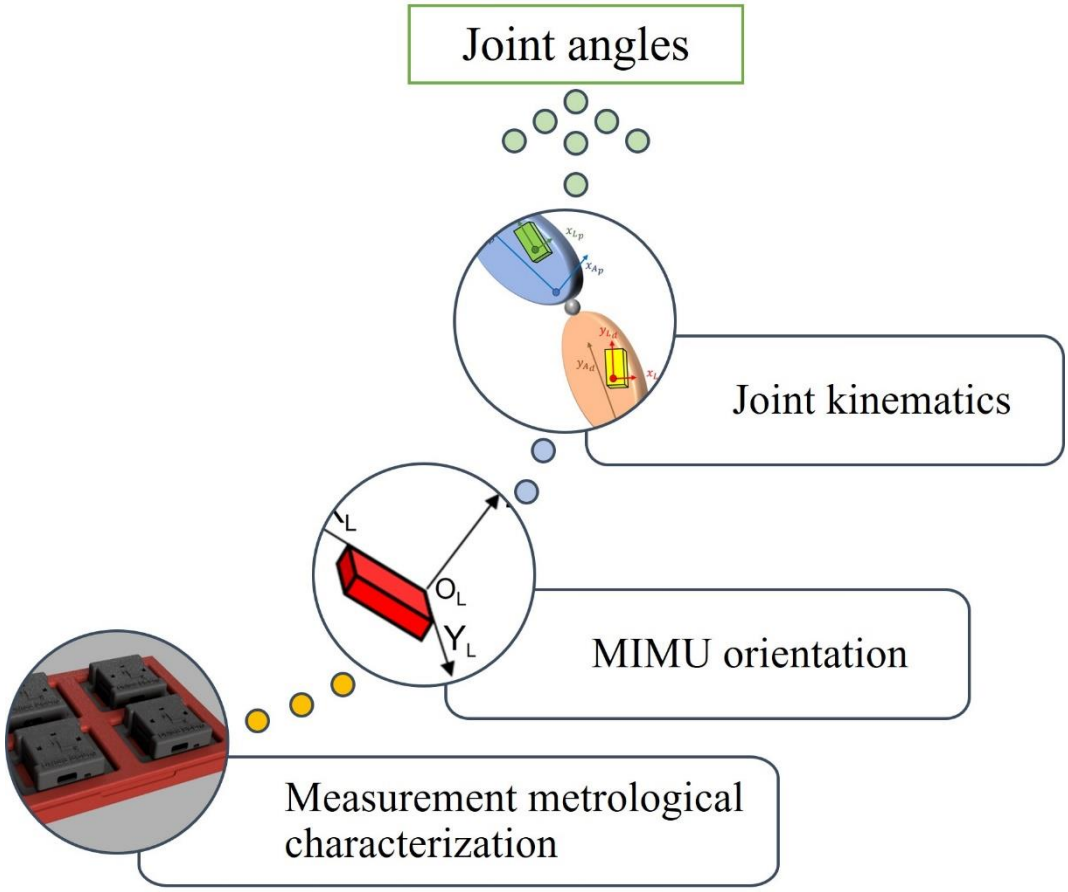

Figure 1: the bottom-up approach used in this thesis presentation.

References

Bergamini, E., Ligorio, G., Summa, A., Vannozzi, G., Cappozzo, A., & Sabatini, A. M. (2014). Estimating orientation using magnetic and inertial sensors and different sensor fusion approaches: Accuracy assessment in manual and locomotion tasks. *Sensors (Switzerland)*, *14*(10), 18625–18649. https://doi.org/10.3390/s141018625

Brodie, M. A., Coppens, M. J., Ejupi, A., Gschwind, Y. J., Annegarn, J., Schoene, D., Wieching, R., Lord, S. R., & Delbaere, K. (2017). Comparison between clinical gait and daily-life gait assessments of fall risk in older people. *Geriatrics and Gerontology International*, *17*(11), 2274–2282. https://doi.org/10.1111/ggi.12979

Grewal, M. S., Weill, L. R. (Lawrence R., & Andrews, A. P. (2007). *Global positioning systems, inertial navigation, and integration*. 525.

Mazzà, C., Alcock, L., Aminian, K., Becker, C., Bertuletti, S., Bonci, T., Brown, P., Brozgol, M., Buckley, E., Carsin, A.-E., Caruso, M., Caulfield, B., Cereatti, A., Chiari, L., Chynkiamis, N., Ciravegna, F., del Din, S., Eskofier, B., Evers, J., … Rochester, L. (2021). Technical validation of real-world monitoring of gait: a multicentric observational study. *BMJ Open*, *11*(12), e050785. https://doi.org/10.1136/bmjopen-2021-050785

Perera, S., Patel, K. v., Rosano, C., Rubin, S. M., Satterfield, S., Harris, T., Ensrud, K., Orwoll, E., Lee, C. G., Chandler, J. M., Newman, A. B., Cauley, J. A., Guralnik, J. M., Ferrucci, L., & Studenski, S. A. (2016). Gait Speed Predicts Incident Disability: A Pooled Analysis. *The Journals of Gerontology: Series A*, *71*(1), 63–71. https://doi.org/10.1093/GERONA/GLV126

Storm, F. A., Nair, K. P. S., Clarke, A. J., Van der Meulen, J. M., & Mazzà, C. (2018). Free-living and laboratory gait characteristics in patients with multiple sclerosis. *Plos One*, *13*(5), e0196463. https://doi.org/10.1371/journal.pone.0196463

Studenski, S., Perera, S., Patel, K., Rosano, C., Faulkner, K., Inzitari, M., Brach, J., Chandler, J., Cawthon, P., Connor, E. B., Nevitt, M., Visser, M., Kritchevsky, S., Badinelli, S., Harris, T., Newman, A. B., Cauley, J., Ferrucci, L., & Guralnik, J. (2011). Gait Speed and Survival in Older Adults. *JAMA*, *305*(1), 50–58. https://doi.org/10.1001/JAMA.2010.1923

World Health Organization. (2005). *Mental health atlas 2005*. World Health Organization.

Yazdi, N., Ayazi, F., & Najafi, K. (1998). Micromachined inertial sensors. *Proceedings of the IEEE*, *86*(8), 1640–1658. https://doi.org/10.1109/5.704269

Zedda, A., Gusai, E., Caruso, M., Bertuletti, S., Baldazzi, G., Spanu, S., Riboni, D., Pibiri, A., Monticone, M., Cereatti, A., & Pani, D. (2020). DoMoMEA: A Home-Based Telerehabilitation System for Stroke Patients. *Proceedings of the Annual International*

Conference of the IEEE Engineering in Medicine and Biology Society, EMBS, *2020-July*, 5773–5776. https://doi.org/10.1109/EMBC44109.2020.9175742

Chapter 2

The MIMU metrological characterization

2.1 Introduction

A Magneto-Inertial Measurement Unit (MIMU) generally integrates a triaxial accelerometer, a triaxial gyroscope, and a triaxial magnetometer. All the three sensors provide an output in their local coordinate system (LCS). In particular, the accelerometer measures the specific force, which is the vector difference between the body acceleration and the gravity, the gyroscope measures the angular velocity around its axes, and the magnetometer measures the local magnetic field which consists of the sum between the Earth's and external magnetic fields. The measurements of the MIMUs can be useful both to extract waveform-related parameters (e.g., peaks identification, to distinguish between stationary and dynamic periods, …) and to estimate some quantities of interest from a biomechanical point of view such as orientation and joint angles, velocity, and displacement. In the latter case, to compute meaningful quantities, it is usually required to integrate the measurements over a finite period (Aslan & Saranli, 2008). The inherent errors which inevitably affect each sensor output accumulate during the integration thus leading to inaccuracies growing unbounded over time (Cereatti et al., 2015). As highlighted in the literature, the errors can be classified as deterministic and stochastic (Hussen & Jleta, 2015). In particular, the former, including bias, non-orthogonality, misalignment, etc., can be compensated for by applying procedures to refine the calibration of the sensors. The stochastic

components, including random fluctuations, instability, etc., capture errors which are considered random and hence can be only statistically described (El-Sheimy et al., 2008) since there is not a clear relationship between the amplitude of the stochastic errors and the amount of errors affecting the physical quantity of interest. However, the knowledge of both errors components is central when using MIMU to accurately derive quantitative information. The process of quantifying the amount of errors of each measurement is called *characterization* and it is useful to create a model of the errors, to compare the performance of the sensor with those declared by the manufacturer in the datasheets, and to understand whether a refinement of the calibration coefficients is needed. Usually, the sensors embedded in a MIMU undergo to sensor-specific calibrations conducted during the manufacturing process (i.e., factory calibration). However, as an example, some misalignment between the sensor axes and the MIMU case could arise due to an imprecise assembling process. It should be also noted that the deterministic performances may deteriorates over time, and it is good practice to assess them on a routine basis. Implementation of procedures for ensuring that recorded signals are accurate and repeatable is urgent when sensor measurements are employed to derive specific parameters for clinical description mobility and quantification of the subject motor impairments (Aydemir & Saranli, 2012; Mazzà et al., 2021). In the literature, the evaluation of the measurement accuracy is mainly performed on the final estimate, usually in terms of position or Euler angles (Ailneni et al., 2019) obtained through a sensor fusion filter which, however, is influenced by the value of its parameters thus making the contribution of each source of error indistinguishable (Caruso, Sabatini, Laidig, et al., 2021). Hence, there is a lack of methodology to characterize the errors affecting the accelerometer, the gyroscope, and the magnetometer, separately.

The purpose of this chapter is to propose a battery of tests useful to characterize both the stochastic and the deterministic error components of the MIMU signals. To this end, an introduction about the measurement principle of each sensor is presented and the relevant errors are described. Finally, a case of study regarding the deterministic error characterization of a set of MIMUs before and after the refinement of their calibration coefficients is provided to show the usefulness of the proposed tests.

2.2 Description of the MIMU output

In the following, the bold notation refers to vector and matrix quantities.

2.2.1 Accelerometer

An accelerometer senses the so called "specific force" ($\boldsymbol{a}$) which is the vector difference between the acceleration of the body ($\boldsymbol{a}_{body}$) and the gravity acceleration ($\boldsymbol{g}$). All the quantities are resolved in the LCS of the sensor, and the output is reported in (1):

$$\boldsymbol{a} = (\boldsymbol{a}_{body} - \boldsymbol{g}) \tag{1}$$

From (1) it is possible to understand that when the device is not undergoing any accelerations, the $\boldsymbol{a}_{body}$ contribution is null, and the accelerometer works as an inclinometer by sensing the gravity acceleration only. On the contrary, when the accelerometer experiences a free-fall, the $\boldsymbol{a}_{body}$ term is equal to $\boldsymbol{g}$ and the accelerometer output is null. In other words, when the MIMU is moving the contribution of the $\boldsymbol{a}_{body}$ term is superimposed with $\boldsymbol{g}$ thus making it impossible the accurate estimate of the accelerometer inclination, unless some further sources of information are employed. In addition, the measured accelerometer output $\boldsymbol{a}$ is corrupted by errors whose modeling commonly includes matrix of scale factor error coefficients ($\boldsymbol{S}_a$), matrix of cross coupling error coefficients, also known as non-orthogonality, ($\boldsymbol{M}_a$), a vector a of bias error ($\boldsymbol{b}_a$) and the vector representing its fluctuations ($\boldsymbol{\delta b}_a$), and white Gaussian noise as stated in equation (2) (Aydemir & Saranli, 2012; Unsal & Demirbas, 2012):

$$\boldsymbol{a} = (\boldsymbol{S}_a + \boldsymbol{M}_a)\big(\boldsymbol{a}_{body} - \boldsymbol{g}\big) + \boldsymbol{b}_a + \boldsymbol{\delta b}_a + \boldsymbol{w}_a \tag{2}$$

More in detail, $\boldsymbol{S}_a$ is the diagonal 3x3 matrix of coefficients representing for each axis the deviation of the sensor sensitivity from ideal. This error usually contains a fixed part and temperature induced variation (Nez et al., 2018). $\boldsymbol{M}_a$ represents the 3x3 matrix of the non-orthogonality errors among the three accelerometer sensing axes due to the mounting of the mechanical components. The non-orthogonality leads to an undesired coupling of the axes output following the trigonometric formula. The $\boldsymbol{b}_a$ 3x1 vector represents the accelerometer bias which is defined as the axis output in absence of $\boldsymbol{g}$. The bias vector $\boldsymbol{b}_a$ contains a fixed part and temperature induced variation. $\boldsymbol{S}_a$, $\boldsymbol{M}_a$, and $\boldsymbol{b}_a$ can be compensated by using a calibration refinement algorithm (Aslan & Saranli, 2008). However, the bias error also contains run-to-run variations, turn-on to turn-on variations, and in general a slow change over time. These latter components of the errors are

represented by the $\boldsymbol{\delta b}_a$ 3x1 vector which represents one of the major problems when estimating the displacement since the accelerometer output is double integrated after the gravity subtraction. Finally, $\boldsymbol{w}_a$ is the 3x1 vector of white Gaussian noise with zero mean. The $\boldsymbol{\delta b}_a$ and $\boldsymbol{w}_a$ vectors belong to the stochastic error components and can be only statistically characterized, as described more in detail in the following sections.

2.2.2 Gyroscope

A gyroscope senses the angular velocity along its axes. Different gyroscope output models have been proposed in the literature over the years, the main differences are in the complexity of the slow-varying bias model $\boldsymbol{\delta b_g}$ (Aydemir & Saranli, 2012; Kirkko-Jaakkola et al., 2012; Parvis & Ferraris, 1995; Unsal & Demirbas, 2012). A general model, is proposed in (3):

$$\boldsymbol{\omega} = \left(\boldsymbol{S}_g + \boldsymbol{M}_g\right) \boldsymbol{\omega}_{body} + \boldsymbol{b_g} + \boldsymbol{\delta b_g} + \boldsymbol{w_g} \tag{3}$$

It has to be said that other models such as (Aslan & Saranli, 2008; Aydemir & Saranli, 2012; Parvis & Ferraris, 1995; Unsal & Demirbas, 2012) consider an additional term which links the bias dependency on the magnitude of the acceleration since the latter affects the gyroscope MEMS structure. However, as pointed out by (Parvis & Ferraris, 1995) the sensitivity to the acceleration is negligible with respect to the other error contribution.

As for the accelerometer, $\boldsymbol{S}_g$ and $\boldsymbol{M}_g$ represent the 3x3 scale factor and non-orthogonality error matrices, respectively. The $\boldsymbol{b_g}$ 3x1 vector contains the gyroscope bias which is defined as the axis output in absence of rotation. It is common to compute $\boldsymbol{b_g}$ during a static acquisition of a few minutes and then to subtract this value from the gyroscope readings (Caruso, Sabatini, Knaflitz, et al., 2021). However, despite easy to implement, this solution may not be completely effective in practice due to the significant changes of the gyroscope bias which are modeled by $\boldsymbol{\delta b_g}$. The origin of this fluctuations can be found in both the mechanical and electronic components (e.g., change in the drive frequency, flicker in the voltage generation of the digital-analog converters) of a MEMS gyroscope (Gulmammadov, 2009; Hiller et al., 2019; Walther et al., 2013). The $\boldsymbol{\delta b_g}$ is the most influencing source of errors when estimating the orientation. In fact, the integration of the angular velocity including a slow-varying bias leads to a drift of the orientation which grows unbounded over time. Moreover, this orientation drift

directly affects the displacement estimation since the gravity, before the subtraction from the accelerometer output, needs to be expressed in the LCS of the sensor using the orientation already computed. Errors in the gravity subtraction causes huge displacement drift after the double integration (Cereatti et al., 2015). Finally, the $\boldsymbol{w_g}$ vector models the white Gaussian noise with zero mean.

2.2.3 Magnetometer

A magnetometer senses the total magnetic field which is the vector sum between the Earth's magnetic field and the external fields generated by electrical appliances and ferromagnetic objects (Gebre-Egziabher et al., 2001). In fact, in the proximity of the ferromagnetic materials the latter influences the magnetometer output with two terms, namely the hard iron and the soft iron effects, which cannot be neglected according to (Kok et al., 2012). The hard-iron errors $\boldsymbol{h_{hi}}$ are time-invariant and represent an offset due to the permanent magnetization of the ferromagnetic materials which move in solidarity with the magnetometer. On the contrary, the soft-iron effects are a temporary magnetization of the material in response to both Earth's and external magnetic field and they can be seen as a varying bias affecting the magnetometer readings (Gebre-Egziabher et al., 2001). Therefore, the magnitude and the direction of the soft-iron effects depend on the relative orientation between the sensor and the external field and can be modelled by a 3x3 matrix $\boldsymbol{C_{si}}$. It is commonly assumed that the soft-iron response is linear to the external magnetic field and proportional to the magnetic susceptibility. Usually, the hysteresis is not considered except when the magnetometer is located within a very large magnetic field.

The measured magnetic field is also corrupted by both deterministic and stochastic sources of errors. Among the former it is possible to include the 3x3 diagonal scale factor matrix $\boldsymbol{S_m}$, the 3x3 non-orthogonality matrix $\boldsymbol{M_m}$, and a bias vector $\boldsymbol{b_m}$ (intended as a measured non-null magnetic field in absence of input). The bias instability is not usually included in the magnetometer models. Finally, the measurements are corrupted by a white Gaussian noise vector $\boldsymbol{w_m}$. A general magnetometer output model adapted from (Gebre-Egziabher et al., 2001) and (Kok et al., 2012) which accounts for all the aforementioned terms is reported below:

$$\boldsymbol{h} = \boldsymbol{S_m M_m C_{si}}(\boldsymbol{h_{Earth}} + \boldsymbol{h_{hi}}) + \boldsymbol{b_m} + \boldsymbol{w_m} \tag{4}$$

In an ideal case, the magnitude of $\boldsymbol{h}$ is constant over time regardless of the MIMU orientation. This means that the three components h_x, h_x, h_z of the $\boldsymbol{h}$ vector would lie on the surface of a sphere in a 3D plot with radius equal to the local Earth's magnetic field (e.g., 47.5 μT = 475 mG in Turin, Italy). In presence of disturbances and sensor errors, instead, the output lies on a distorted ellipsoid which in general differs from the sphere by a rotation, a translation, a skewness, and a scaling (Kok et al., 2012). The calibration refinement aims at finding the geometrical parameters to map the ellipsoid to the sphere. As an example, Figure 2 compares the results before and after the calibration refinement of a magnetometer embedded in a commercial MIMU (221e s.r.l., Padova, Italy, https://www.221e.com/ last accessed 26th March 2022). It is possible to appreciate that the STD of the magnetic norm has decreased from about 200 mG to only 20 mG.

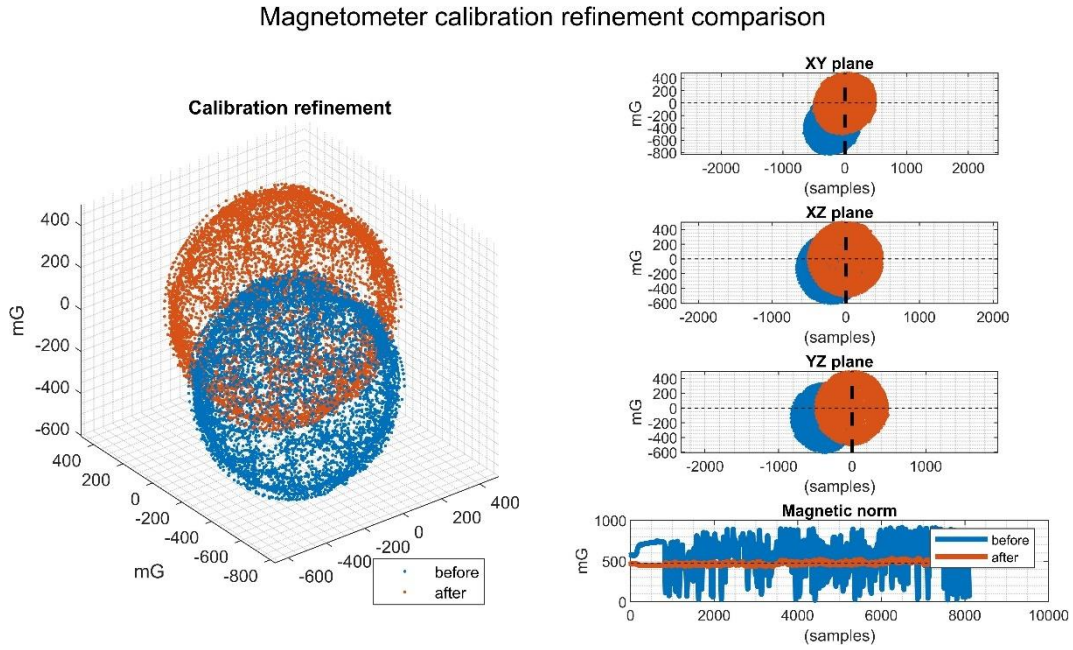

Figure 2: the magnetometer points clouds and the measurement magnitudes obtained before and after calibration refinement.

Among the three types of sensors included in a MIMU, the calibration refinement of the magnetometer is usually the most challenging since it should be conducted in an environment as clean as possible from the ferromagnetic disturbances or, at least, where the present magnetic distortions are stationary in time and space. However, as highlighted by different studies, this refinement is necessary to derive meaningful heading information. The reported results over the

years have shown large improvements in the magnetometer output after the calibration refinement especially in terms of variability of the measured magnitude (as also shown in Figure 2), which should be constant in a magnetic clean environment since only the Earth's field is sensed (Foster & Elkaim, 2008; Kok et al., 2012; Kok & Schon, 2016). Due to the intrinsic difficulties in handling the magnetometer data, sometimes it is preferred not to employ the latter information in the orientation estimation process thus requiring additional hypotheses to be exploited when estimating the joint kinematics, as discussed in Chapter 4. This is particularly convenient during tele-rehabilitation because of the various sources of ferromagnetic disturbances present in the domestic environment (Zedda et al., 2020).

2.3 Metrological characterization tests

In this section, the proposed battery of tests to characterize both the stochastic and deterministic components of the errors is described. In general, to limit the temperature influence on the sensor readings, it is strongly advisable to carry out a ten-minute warm-up before starting the tests (Kirkko-Jaakkola et al., 2012; Lebel et al., 2013).

2.3.1 Tests to assess the stochastic errors

According to IEEE 2700-2017 standard ("IEEE Standard for Sensor Performance Parameter Definitions," 2018), several parameters can be used to characterize the performance of the accelerometer, the gyroscope, and the magnetometer under static conditions. In particular, this characterization focuses on the noise terms corresponding to the white noise and the slowly varying fluctuations of the accelerometer and gyroscope offset, hereinafter generally referred to as $\boldsymbol{\delta b + w}$. The first parameter which can be computed to characterize the overall noise strength is the standard deviation (STD) over a short static acquisition to determine the amplitude of the noise $\boldsymbol{w_a}$, $\boldsymbol{w_b}$, and $\boldsymbol{w_m}$. On the contrary, by acquiring a long static acquisition it is possible to characterize the noise terms included in $\boldsymbol{\delta b}$.

- **Noise characterization during short acquisition**

As anticipated, under static conditions the sensor noise $\boldsymbol{w_a}$, $\boldsymbol{w_b}$, and $\boldsymbol{w_m}$ can be characterized in terms of "precision" by computing the STD values. To this end, the MIMUs are aligned on a wooden board which lies on a surface

completely still and under vibration isolation. Care should also be taken to reduce ferro-magnetic disturbance sources (e.g., at least one meter far from metal objects, smartphone, laptop, …). The IEEE standard suggests the sensor-specific indications which are summarized below.

- Accelerometer noise: it is defined as the smallest measurable change in acceleration calculated as the standard deviation of a minimum 10000 sample points under vibration isolation. The amount of noise must be specified for each orthogonal sensing axis, for each relevant full-scale range, and for each relevant output data rate. The unit of measure is mg.
- Gyroscope noise: It is the smallest measurable change in rotation as the standard deviation of a minimum of 10000 sample points under vibration isolation and zero rotation input. The amount of noise must be specified for each orthogonal sensing axis, for each full-scale range, and for each output data rate. The unit of measure is dps.
- Magnetometer noise: It is the smallest measurable change in magnetic field expressed as the standard deviation of a minimum of 10 seconds of measurements collected at a minimum of 20 samples per second under static magnetic field and vibration isolation. The amount of noise must be specified for each orthogonal sensing axis, for each full-scale range, and for each output data rate. The unit of measure is μT.

▪ **Noise characterization during long acquisition**

As anticipated, the characterization conducted over long period allows to know more in depth the different source of errors responsible for the bias random variations. Focusing on $\boldsymbol{\delta b}$, various model can be found in the literature. Ferraris *et al*. in 1995 described $\boldsymbol{\delta b}$ as a deterministic linear function of time thus needing two measurements to be performed immediately before and after the sensor use to estimate the slope coefficient. However, the most popular models such as Gauss-Markov Model, Random Walk Model, … belongs to the stochastic family. Overall, recent studies converge on the Gauss-Markov Model as the most appropriate mathematical representation of the bias variations (Bhatt et al., 2012; Flenniken et al., n.d.; Nikolic et al., 2016; Quinchia et al., 2013; Unsal & Demirbas, 2012). The Gauss-Markov model is described below for the gyroscope, but the discussion can be equivalently extended to the accelerometer.

When considering equation (3) in static conditions (i.e., absence of input) and after having subtracted the mean value output (i.e., $\boldsymbol{b} = 0$), the noisy gyroscope readings can be represented as follows:

$$\boldsymbol{\omega} = \boldsymbol{\delta b} + \boldsymbol{w} \tag{5}$$

The white noise $\boldsymbol{w}$ is responsible for the random walk process which affects the angle (or velocity in the case of the accelerometer) after the time integration of the angular velocity (acceleration). The strength of $\boldsymbol{w}$ amounts to $\boldsymbol{\sigma_w}$ and it is often referred as angle (velocity) random walk ARW (VRW) as reported in IEEE standards (IEEE Aerospace and Electronic Systems Society. Gyro and Accelerometer Panel. & Institute of Electrical and Electronics Engineers., 1998) or more simply to the noise density of the sensor output computed over a short period and usually reported in the sensor datasheets. The Gauss-Markov model describes the variation of $\boldsymbol{\delta b}$ as an exponentially time-correlated slow varying process with zero-mean, a correlation time τ, and driven by the noise $\boldsymbol{v}$. Mathematically, the $\boldsymbol{\delta b}$ variations are represented in the continuous time domain by the following equation:

$$\frac{d(\boldsymbol{\delta b})}{dt} = -\frac{\boldsymbol{\delta b}}{\tau} + \boldsymbol{v} \tag{6}$$

The vector $\boldsymbol{v}$ is assumed to be white Gaussian noise process, uncorrelated from $\boldsymbol{w}$, and whose variance amounts to $\boldsymbol{\sigma_b^2}$. The integration of (6) in the discrete time domain, in addition to first order Taylor approximation due to $\tau \gg \Delta t$ leads to:

$$\boldsymbol{\delta b}[k] = \boldsymbol{\delta b}[k-1]e^{\left(-\frac{\Delta t}{\tau}\right)} + \boldsymbol{v}\Delta t \tag{7}$$

By analyzing equations (6) and (7), it is possible to notice that the bias variations at the current time point is correlated with its value at the previous time point by means of τ and these variations are driven by a random walk which arises after the integration of the white noise. The variance of the random walk under analysis is simply given by $\boldsymbol{\sigma_b^2}\Delta t$ which therefore is not constant but increases with time. In addition, when τ approaches to zero, $\boldsymbol{\delta b}$ is equivalent to the ARW (VRW), while when τ approaches to infinite $\boldsymbol{\delta b}$ is equivalent to a "pure" random walk bias model. In the latter case, $\boldsymbol{\sigma_b}$ is termed as the angular velocity (acceleration) random walk, also known as rate random walk, namely RRW (AcRW).

The Gauss-Markov model has gained popularity due to its expressive power despite the limited number of parameters ($\boldsymbol{\sigma_w^2}$, $\boldsymbol{\sigma_b^2}$, τ) which can be incorporated within an optimal state-space estimator, such as a Kalman filter (Nikolic et al., 2016). These parameters can be directly identified on the Allan deviation plot, which is based on the Allan variance method. The Allan variance method was first proposed in the 60s to analyze the frequency stability of precision oscillators (Allan, 1966), later it was adapted to characterize the inertial sensors, especially by computing its square root, i.e., the Allan Deviation (ADEV). The basic idea is to take a long sequence of data and divided it into bins based on an averaging time (τ). The data are averaged in each bin and the difference in average between successive bins is computed. Finally, the Root Mean Square (RMS) of this value is obtained. This value is a quantitative information of how much the average value changes at that specific τ. These operations are repeated by increasing τ and the typical Allan Variance graphical representation ($\log_{10}\tau$, $\log_{10}$ ADEV) is obtained (Figure 3). The ADEV description is also adopted for assessing gyroscope bias instability generated by the so called "flicker noise" which is difficult to predict and handled mathematically (Han et al., 2006).

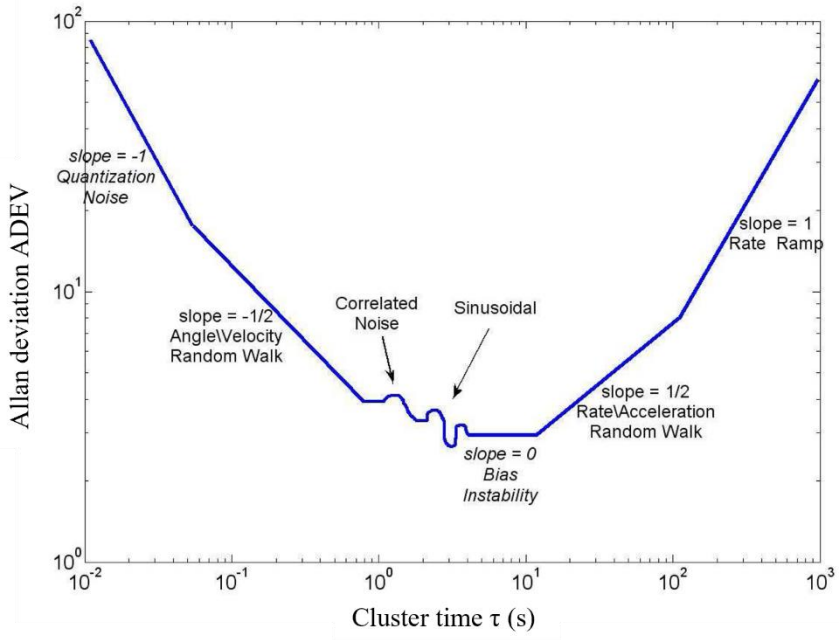

Figure 3: typical ADEV graphical representation for a gyroscope/accelerometer. Picture adapted from (Quinchia et al., 2013). IEEE Std 952-1997.

The IEEE standard suggests the gyroscope and the accelerometer parameters to be extracted from ADEV which are summarized below and graphically represented in Figure 3Figure 3.

- Angle Random Walk (ARW) and Velocity Random Walk (VRW): the high-frequency noise terms that have correlation time much shorter than the sample time can contribute to the ARW and VRW for the gyroscope and accelerometer, respectively. It is represented by a slope = -1/2 in the Allan Deviation plot. The ARW (VRW) coefficient is named N and it can be read off as the slope of the line at τ = 1 s. The unit of measure is deg/√h for the gyroscope and m/s/√h for the accelerometer.
- Bias Instability: also known as "flicker noise". This is a low frequency bias fluctuation in the measured rate data. The origin of this noise is the electronics or other components susceptible to random flickering. It is represented by a slope = 0 in the Allan Deviation plot and its coefficient B can be read directly from this line with a scaling of 0.664. The unit of measure is deg/h for the gyroscope and m/s/h for the accelerometer.
- Rate Random Walk (RRW) and Acceleration Random Walk (AcRW): the drift in the angular velocity and acceleration due to model presented in (7). It is represented by a slope = 1/2 in the Allan Deviation plot. The RRW (AcRW) coefficient is named K and it can be read off as the slope of the line at τ = 3 s. The unit of measure is m/s/h$^{3/2}$ for the accelerometer and deg/h$^{3/2}$ for the gyroscope.

The Allan Variance of the total process $\boldsymbol{\sigma_{AV}^2}$ can be represented as the sum of all the terms since they are uncorrelated belonging to different regions (El-Sheimy et al., 2008):

$$\boldsymbol{\sigma_{AV}^2} = N^2 \frac{\mathbf{1}}{\tau} + B^2 \frac{2}{\pi} ln2 + K^2 \frac{\tau}{3} \tag{8}$$

It has to be said that the ADEV allows also to estimate the quantization noise and the rate ramp errors which, however, are not of interest in this work.

2.3.2 Tests to assess the deterministic errors

As previously mentioned, the deterministic parts of the measurement errors can be corrected by means of a recalibration refinement process. Prior to this, it is therefore necessary to understand when a device should be recalibrated. The tests

proposed in this section aims at assessing the amount of the deterministic sources of errors for the accelerometer, the gyroscope, and the magnetometer. These novel tests have been designed by the author based on the recommendations adapted from the procedures commonly proposed in the literature for the calibration refinement. Since the majority of this tests requires the accurate alignment of the sensor axes along the vertical direction (Nez et al., 2016), an *ad hoc* case was designed and 3D-printed to host up to four MIMUs. The 3D printing process was carried out by Help3D company (https://help3d.it/, Padova, Italy). The case was designed to have flat faces and sharp edges to facilitate the positioning along the vertical direction. In addition, the axis orientation was marked on each surface (Figure 4). This case is particularly helpful for those MIMUs manufactured with rounded surfaces which could not be accurately aligned otherwise. Additional technical specifications are reported in the appendix of this chapter.

Figure 4: the 3D printed case (left). Bottom view (center). Top cover bottom view (right).

Accelerometer

The ideal and noisy accelerometer output is described by the equations (1) and (2), respectively. The deterministic tests are conceived for assessing how much the ideal output deviates from the ideality due to $\boldsymbol{S}_a$, $\boldsymbol{M}_a$, and $\boldsymbol{b}_a$ during both static and dynamic conditions. The random sources of errors $\boldsymbol{\delta b}_a + \boldsymbol{w}_a$ are neglected since in each test the measurements are averaged over a certain number of samples long enough to mitigate the effect of the white noise but, at the same time, adequately short to ensure that the bias fluctuations do not have time to considerably jeopardize the output.

- **Gravity test in static**

In the gravity test the influence of the deterministic sources of errors is assessed during a multi-orientation static acquisition. This test is adapted from the calibration refinement procedure usually employed for the accelerometer e.g., (Stančin & Tomažič, 2014) and it consists in acquiring the accelerometer

measurements for each of the six orientations (+x, -x, +y, -y, +z, -z), one at a time. In particular, for each orientation the case hosting up to four MIMUs is aligned with the corresponding axis along the gravity direction (the horizontality of the surface could be verified with a spirit level) and a two-minute static recording is acquired (Figure 5). For each i-th orientation, the accelerometer measurements are averaged over time.

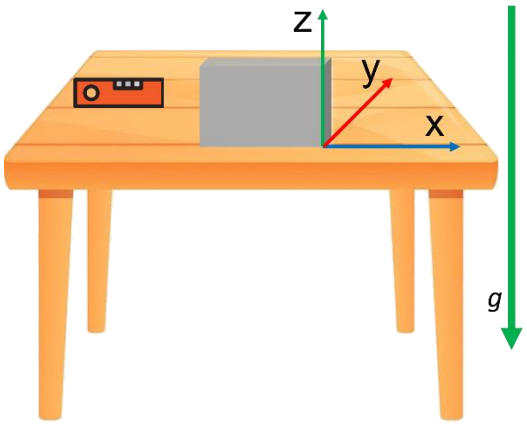

Figure 5: the setup for the gravity test. The case hosting up to four MIMUs is orientated to have one axis at a time aligned along the gravity direction (in this case $\boldsymbol{i}$-th = +z). A spirit level is employed to verify that the surface is horizontal.

This test assesses the hypothesis that in absence of motion the accelerometer output should be equal to $\boldsymbol{g}$, both in terms of magnitude and direction, as highlighted in (1). For this reason, the two following conditions must be verified:

1. The accelerometer norm must be equal to $|\boldsymbol{g}|$. The norm difference is evaluated for each i-th orientation as follows:

$$d_{norm} = \sqrt{a_x^2 + a_y^2 + a_z^2} - |\boldsymbol{g}| \tag{9}$$

   The d_{norm} is expressed in mg and it should amount to zero in case of an ideal situation.
2. The average signal output should be close to g for the vertical axis and close to zero for the two other horizontal axes. A summary quantity is represented by the angular deviation from the ideal vector expressed in the accelerometer LCS which can be computed for each i-th orientation using

the following trigonometric formula (· denotes the scalar product operator):

$$\delta = \cos^{-1}\left(\frac{\boldsymbol{a}_i}{|\boldsymbol{a}_i|} \cdot \frac{\boldsymbol{g}_i}{|\boldsymbol{g}|}\right) \tag{10}$$

The δ is expressed in *deg* and it should amount to zero in case of an ideal accelerometer. The values of the ideal gravity vector $\boldsymbol{g}_i$ are reported in Table I for each i-th orientation.

Table I: the ideal gravity vector expressed in the accelerometer LCS for each $\boldsymbol{i}$-th orientation.

i-th orientation	Ideal $\boldsymbol{g}_i$
+ x	[*g* 0 0]
- x	[*-g* 0 0]
+ y	[0 *g* 0]
- y	[0 *-g* 0]
+ z	[0 0 *g*]
- z	[0 0 *-g*]

Between the two proposed metrics, the d_{norm} is not sensitive to the non-accurate alignment along the vertical direction since it is based on the magnitude of the measurements (Nez et al., 2016). On the contrary, δ is more informative about the direction of the sensed quantity. These two complementary metrics are useful for a complete characterization of the accelerometer output in static.

- **Free-falling test**

This test aims at characterizing the accelerometer output during dynamic conditions by exploiting the gravity acceleration. In fact, during a free-falling the output should be null as stated by equation (1). This test is performed by dropping the MIMU under only the gravity acceleration, i.e., initial velocity = 0 m/s, on a soft surface (so as not to damage it), as depicted in Figure 6.

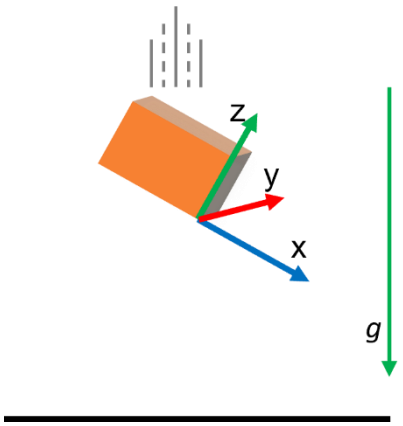

Figure 6: during the free-falling test the MIMU is dropped on a soft surface without initial velocity under the gravity acceleration.

The norm of the accelerometer output is computed as follows:

$$d_{ff} = \sqrt{a_x^2 + a_y^2 + a_z^2} \tag{11}$$

The d_{ff} is expressed in mg and should approaches to zero during this test. An example of d_{ff} is reported in Figure 7 for an experiment conducted with a Xsens-MTw (Xsens, Enschede, The Netherlands).

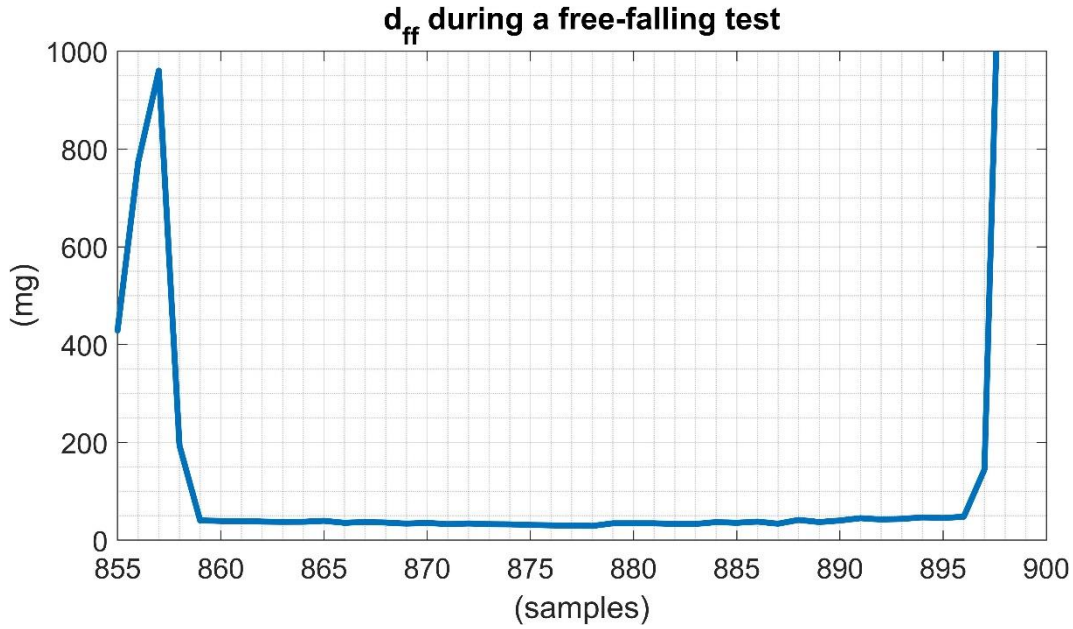

Figure 7: the d_{ff} is reported during a free-falling test.

Gyroscope

The typical gyroscope output is described by the equation (3). The proposed deterministic tests are conceived for assessing how much the ideal output deviates from the ideality due to $\boldsymbol{S}_g$, $\boldsymbol{M}_g$, and $\boldsymbol{b}_g$ during both static and dynamic conditions. As for the accelerometer, the random sources of errors $\boldsymbol{\delta b}_g + \boldsymbol{w}_g$ are neglected.

- **Gyroscope bias test**

In this test the gyroscope readings are averaged over three minutes of static acquisition to compute the so-called bias (or offset), represented by $\boldsymbol{b}_g$.

- **Angular velocity accuracy test**

This test aims at assessing how accurate the measured angular velocity is with respect to a reference value. To compute the latter value, it is sufficient to rotate the MIMU over a known amount of angle φ (usually multiple integers of 360 deg) along a single axis for a certain amount of time and to compute the ratio between these two quantities (Stančin & Tomažič, 2014). In general, it is advisable to perform several complete rotations since the higher the angle is, the lower it is the amount of uncertainty affecting the measurement of the elapsed time (based on the identification of the starting and the ending of motion) during the rotation. Although this test does not require any instrument, e.g., the rotations could be performed by hand, a rotation plate could be adopted to facilitate the execution of several rotations for longer time. An *ad hoc* rotation plate was designed and 3D printed in polylactic acid. Additional details can be found in the Appendix at end of this chapter.

In this test, the MIMU is placed over the plate to have one axis aligned along the rotation axis direction. The plate is programmed to execute 100 complete rotations (φ = 360 deg x 100) at 33 rpm. The elapsed time is then computed using a thresholding approach on the angular velocity signal under consideration. This test is repeated for each i-th axis (x, y, z) and the relative difference $d_{\omega\%}$ is computed as follows:

$$d_{\omega\%} = 100 \frac{\overline{\omega_i} - \frac{\varphi}{\Delta T}}{\frac{\varphi}{\Delta T}} \tag{12}$$

In (12), $\overline{\omega_i}$ represents the average measured angular velocity for a given i-th MIMU axis, while φ and ΔT are the rotation angle and elapsed rotation time, respectively. In general, the difference between the measured and the actual angular velocity is not simply represented by $\boldsymbol{b}_g$. In fact, as it can be observed in (3), the non-null output is scaled by $\boldsymbol{S}_g + \boldsymbol{M}_g$.

- **Rotation angle accuracy test**

This test is designed to assess how accurate the angle obtained by the integration of the angular velocity during a single-axis rotation is with respect to a reference value. The same value acquired during the previous test could be used. The relative difference $d_{\varphi\%}$ is computed as follows:

$$d_{\varphi\%} = 100\frac{\int_{t=0}^{t=\Delta T}\omega_i dt - \varphi}{\varphi} \tag{13}$$

Compared to the "angular velocity accuracy test", in this one the presence of $\boldsymbol{b}_g$ has a greater influence on the estimated angle due to the integration operator and this could result in a linear drift growing with time.

Magnetometer

The typical magnetometer output is described by the equation (4). The proposed deterministic tests are conceived for assessing how much the ideal output deviates from the ideality due to $\boldsymbol{S}_m$, $\boldsymbol{M}_m$, $\boldsymbol{C}_{si}$, $\boldsymbol{h}_{hi}$, and $\boldsymbol{b}_m$. As for the inertial sensors, the random source of errors $\boldsymbol{w}_m$ is neglected. To the best of author's knowledge, the only metrics suggested to evaluate the accuracy of the magnetometer output is the variability of the magnetic norm in a magnetically homogenous environment. This paragraph proposes an additional test to evaluate the magnetometer accuracy by computing the geometric parameters to quantify the deviation from the ideality.

- **Ellipse test**

As anticipated, the magnetometer measurements should lie on a sphere surface of radius equal to the strength of the local Earth's magnetic field in absence of disturbances. This means that, in an ideal situation, when the magnetometer undergoes a complete planar rotation around one of its axes, the recorded data should lie on a circumference centered in the origin with radius *r*

equal to the magnitude of the Earth's field projected onto the horizontal plane. In practice, by graphing the signals, an ellipse with axes $a > b \neq r$ (i.e., eccentricity $e \neq 0$) rotated with respect to the horizontal of an angle φ, and center $\boldsymbol{c} \neq (0,0)$ is obtained, as illustrated in Figure 8. The distance $|\boldsymbol{d}|$ of $\boldsymbol{c}$ from the origin can be attributed to hard iron errors, while the different axis length and φ are due to the combined effect of scale factors, misalignment, and soft-iron errors.

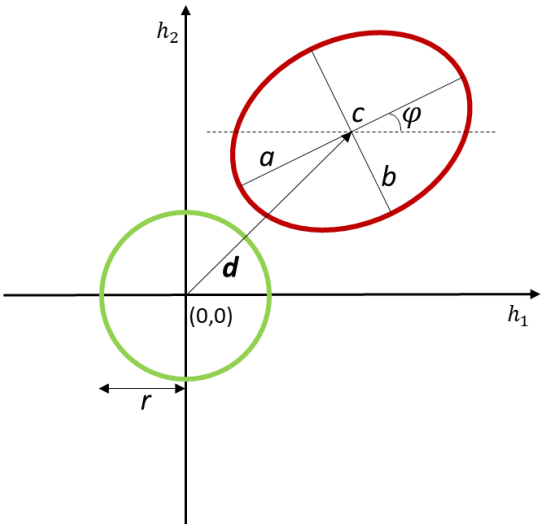

Figure 8: the comparison between the ideal output (in green) and the measured (red) occurring during a complete rotation about a generic magnetometer axis. The ellipse is obtained after the Earth's magnetic field distortion and the sensor deterministic errors. *a* and *b* are the ellipse major and minor axes, respectively.

In this test, the MIMU is placed over the plate to have one axis aligned along the rotation axis direction. One complete rotation is performed without constraint on the angular velocity provided that the latter allows to collect a sufficient number of samples given the sampling frequency. Then an ellipse is fitted to the magnetometer data by following a least-square approach, e.g., (Gander et al., 1994), to estimate a, b, $\boldsymbol{c}$, and φ. In addition to φ, the synthetic parameters $|\boldsymbol{d}|$ and e can be computed to characterize of the magnetometer deterministic errors as follows:

$$|\boldsymbol{d}| = \sqrt{c(1)^2 + c(2)^2} \tag{14}$$

$$e = \sqrt{1 - \frac{b^2}{a^2}} \tag{15}$$

In presence of an ideal magnetometer $|\boldsymbol{d}|$, φ, and e should be null. The test is repeated for each magnetometer axis.

- **Sphere test**

This test is proposed to evaluate the magnetic norm variability in absence of ferromagnetic disturbances. In this condition, the norm should remain constant and amount to a value equal to the strength of the local Earth's magnetic field, which can be assessed by available geomagnetic maps. The MIMU is rotated by hands around its three-axes at the same time to trace as much of a full sphere as possible (Figure 9).

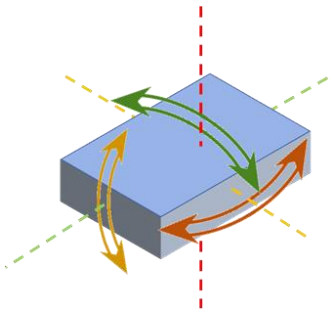

Figure 9: the 3D simultaneous rotation of the MIMU around its three axes.

In the sphere test, the characterization of the deterministic errors is provided in terms of STD of the magnetic norm collected during the entire test, as follows:

$$h_{n_{STD}} = STD(|\boldsymbol{h}|) \tag{16}$$

An example is shown in Figure 2 where the STD amounted to 200 mG before performing the calibration refinement.

2.3.3 Application: effects of calibration refinement

This section aims at implementing the presented deterministic tests to assess the quality improvement of the signals collected before and after the calibration refinement from a set of 24 INDIP MIMUs (manufactured by the University of Sassari, Sassari, Italy and 221e https://www.221e.com/it/, Padova, Italy). Each INDIP includes a triaxial accelerometer (full-scale up to ±16 g), a triaxial gyroscope (full scale up to ± 2000 dps), and a triaxial magnetometer (full scale up to ±50 G). Data are processed by an ultra-low-power microcontroller (ARM® 32-

bit Cortex®-M4 CPU) and stored in an on-board 128 MB flash storage for up to four hours of all sensors data logging. All the data were recorded at 100 Hz.

The tests were performed immediately before and after one week from the calibration refinement. All the refinement procedures aimed at estimating one correction matrix $\boldsymbol{C}$ and one bias vector $\boldsymbol{q_0}$ of the measured quantity $\boldsymbol{q_s}$ to match the latter to the ideal case in a least-square sense. The corrected measurements $\boldsymbol{q}$ were then obtained based on the following calibration model (Stančin & Tomažič, 2014):

$$\boldsymbol{q} = \boldsymbol{C}(\boldsymbol{q_s} - \boldsymbol{q_0}) \tag{17}$$

The characterization tests before the calibration refinement were made on $\boldsymbol{q_s}$, while on $\boldsymbol{q}$ after the refinement. The experiments concerning the accelerometer coefficients were based on the procedure described in (Stančin & Tomažič, 2014) involving the multi-orientation acquisition. Moreover, to overcome the problem of the non-perfectly horizontality of the base plane, four acquisitions for each axis were conducted, each time rotating the case by 90 deg. The experiments needed to refine the gyroscope calibration coefficients exploited the principles described in (Stančin & Tomažič, 2014) using the developed rotation plate to facilitate the execution of the rotations whose angular velocity was set to 33 rpm (i.e., the same value of the characterization test). Finally, the magnetometer refinement procedure was implemented following the algorithm proposed in (Gebre-Egziabher et al., 2001). In this case, the experiments consisted in the sphere rotation identical to that described in the "sphere test" paragraph. For each test, the comparison before/after the refinement was carried out by means of the notched boxplots which are a synthetic representation of the distribution, as graphically explained in Figure 10. The 25^{th} and 75^{th} percentiles are denoted by Q_1 and Q_3, respectively and their difference defines the inter quartile range (IQR). The notch is represented as a narrowing around the median value, and it offers quick evidence of the significance of the median differences of the boxplots. In fact, when the notches do not overlap it is possible to conclude that the median are statistically different with 95% confidence. The width of the notch is given by $\pm 1.5\, IQR/\sqrt{n}$, where n is the sample size.

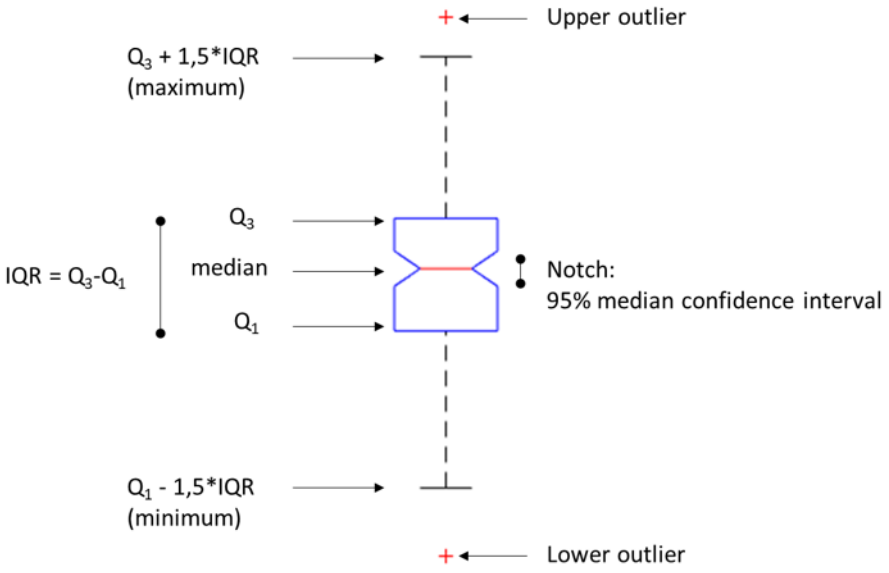

Figure 10: the boxplot representation. The notch defines the 95% of the median confidence interval. Elements which exceed the minimum and maximum are defined outliers and represented with red crosses.

The results are reported below for each test.

- **Gravity test in static**

The boxplots for d_{norm} and δ are reported in Figure 11 and Figure 12, respectively.

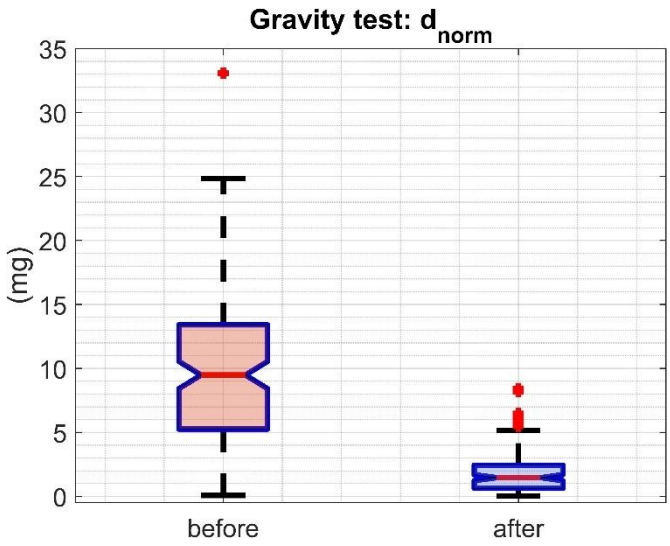

Figure 11: the comparison between $\boldsymbol{d_{norm}}$ computed before and after the accelerometers' calibration refinement.

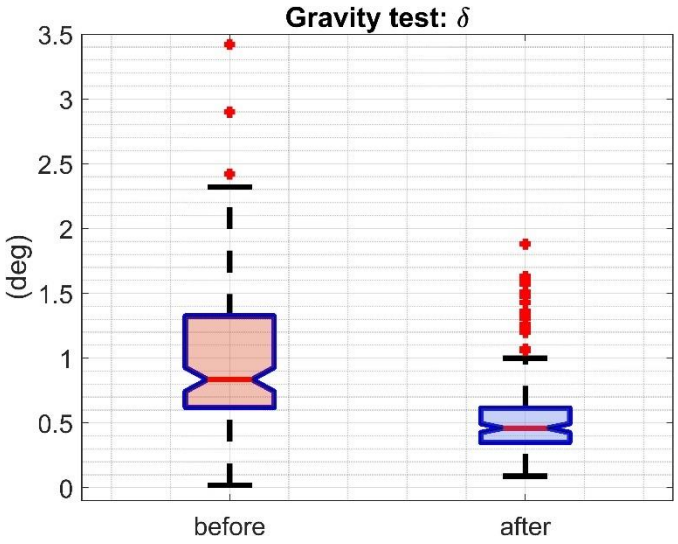

Figure 12: the comparison between $\boldsymbol{\delta}$ computed before and after the accelerometers' calibration refinement.

- **Free-falling test**

The boxplots for d_{ff} are reported in Figure 13.

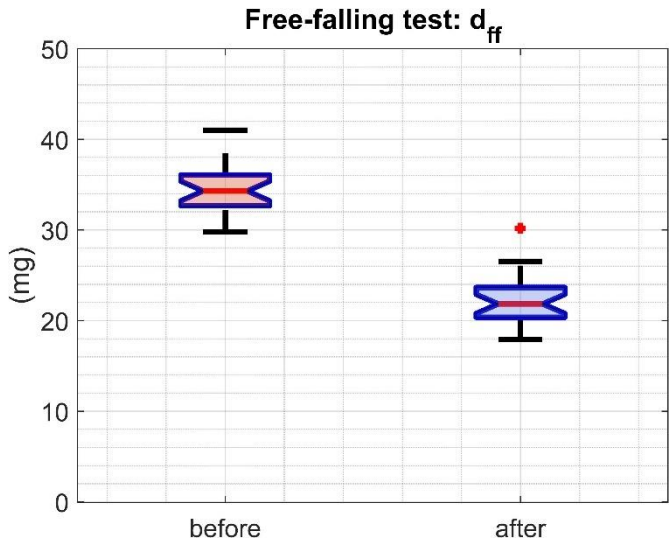

Figure 13: the comparison between $\boldsymbol{d_{ff}}$ computed before and after the accelerometers' calibration refinement.

- **Gyroscope bias test**

The boxplots for $|\boldsymbol{b_g}|$ are reported in Figure 14.

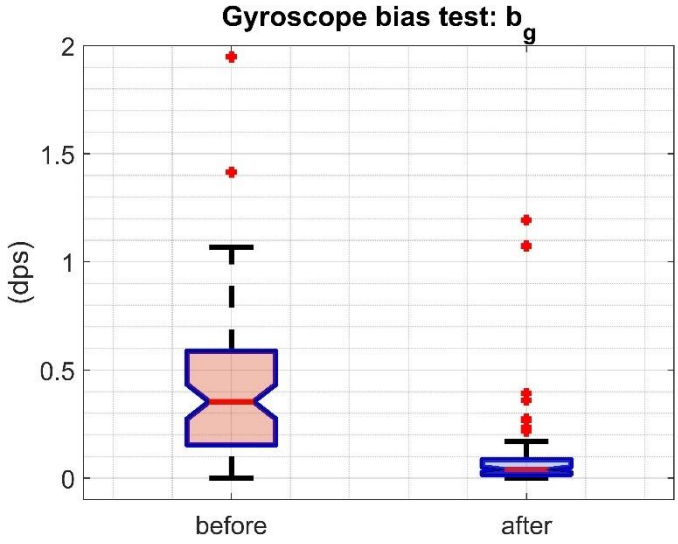

Figure 14: the comparison between $|\boldsymbol{b_g}|$ computed before and after the gyroscopes' calibration refinement.

- **Angular velocity accuracy test**

The boxplots for $d_{\omega\%}$ are reported in Figure 15.

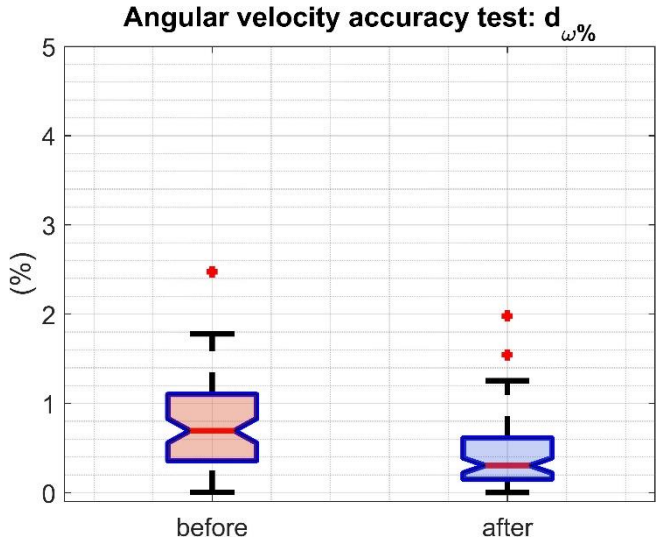

Figure 15: the comparison between $\boldsymbol{d_{\omega\%}}$ computed before and after the gyroscopes' calibration refinement.

- **Rotation angle accuracy test**

The boxplots for $\boldsymbol{d_{\varphi\%}}$ are reported in Figure 16.

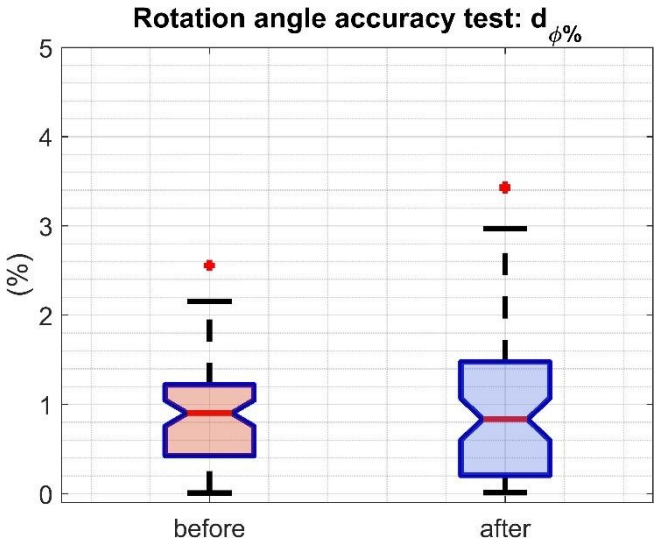

Figure 16: the comparison between $\boldsymbol{d_{\varphi\%}}$ computed before and after the gyroscopes' calibration refinement.

- **Ellipse test**

The boxplots for φ and e are reported in Figure 17 and Figure 18, respectively. Instead, the results for the hard-iron effects $|\boldsymbol{d}|$ are listed in Table II due to the different order of magnitude.

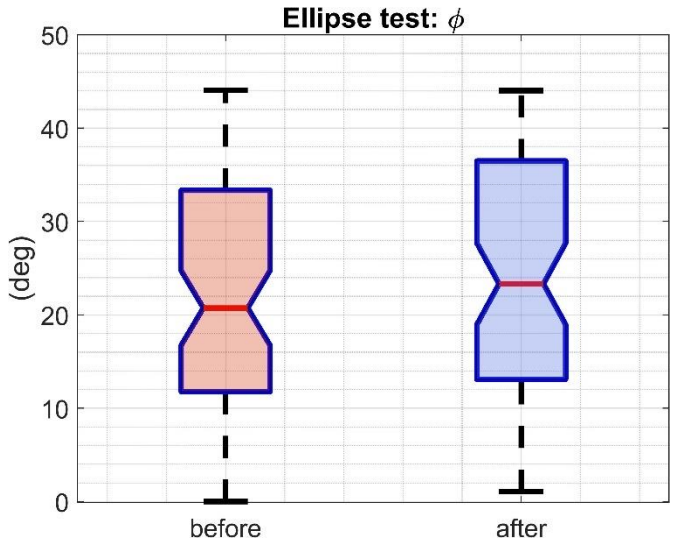

Figure 17: the comparison between $\boldsymbol{\varphi}$ computed before and after the magnetometers' calibration refinement.

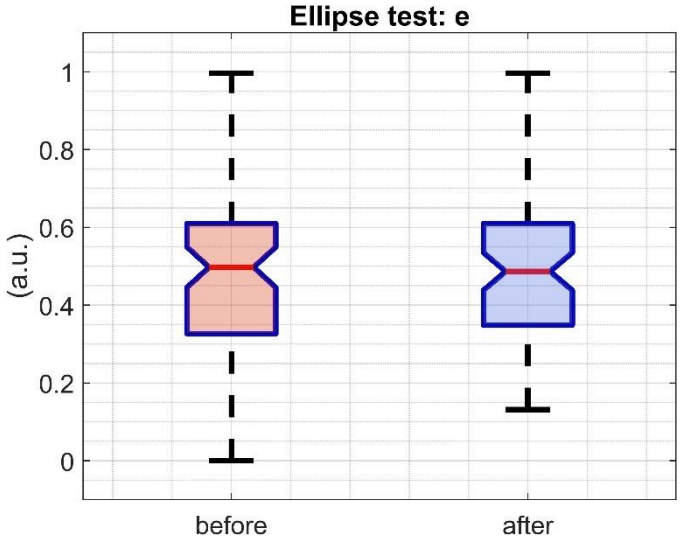

Figure 18: the comparison between $\boldsymbol{e}$ computed before and after the magnetometers' calibration refinement.

Table II: the comparison between $|\boldsymbol{d}|$ computed before and after the magnetometer calibration refinement.

(μT)	$\boldsymbol{d}$
before	8802.8 ± 4776.4
after	3.3 ± 2.8

- **Sphere test**

The results for the magnetic norm variability $h_{n_{STD}}$ are listed in Table III due to the different order of magnitude.

Table III: the comparison between $\boldsymbol{h_{norm_{STD}}}$ computed before and after the magnetometers' calibration refinement.

(μT)	$h_{n_{STD}}$
before	1569.7 ± 773.6
after	7.2 ± 8.7

2.3.4 Discussion

The presented results highlight the effectiveness of the proposed test to assess and quantify the improvement, if any, of the MIMU metrological performance before and after the calibration refinement. In particular, for what concerns the accelerometer, all the three parameters d_{norm}, $\boldsymbol{\delta}$, and d_{ff} exhibited a significant difference between the two assessments. In particular, the median values were lower after the refinement (1.0 mg vs 9.0 mg for d_{norm}, 0.8 deg vs 0.5 deg for $\boldsymbol{\delta}$, and 34 mg vs 22 mg for d_{ff}) and the IQR decreased for all but for d_{ff} where it remained approximatively constant. The gyroscope $\boldsymbol{b}_g$ decreased from 0.3 dps to less than 0.1 *dps* with an IQR five times lower. This is of particular interest when estimating the MIMU orientation using a sensor fusion algorithm. In fact, a higher value of $\boldsymbol{b}_g$ would lead to a higher orientation drift. It is advisable to perform a calibration refinement to reduce the $\boldsymbol{b}_g$ value before integrating the angular velocity. A particular attention must be paid to $d_{\omega\%}$ and $d_{\varphi\%}$ which showed two different behaviors despite being computed from the same measurements. In fact,

the former median was lower after the refinement (0.7 % vs 0.3 %), while the $d_{\varphi\%}$ distribution after the refinement was characterized by the same median value but an increased IQR. This could be justified by the fact that the calibration model (17) does not compensate for the stochastic errors such as the bias run-to-run variations which have a considerable influence during the integration of the angular velocity over three minutes. In other words, the benefit due to the calibration refinement (which are visible on both $\boldsymbol{b}_g$ and $d_{\omega\%}$) are balanced by the detrimental stochastic effects thus compromising the effectiveness of the refinement procedure. For the results obtained for the magnetometer, the only significant differences were found for $|\boldsymbol{d}|$ and for $h_{norm_{STD}}$ (2600 and 200 times lower, respectively). The $\boldsymbol{\varphi}$ and $\boldsymbol{e}$ remained substantially unchanged and this was expected since the implemented algorithm for the calibration refinement (Gebre-Egziabher et al., 2001) considers $\boldsymbol{M}_m$ and $\boldsymbol{C}_{si}$ to be ideal. This means that neither the eccentricity nor the rotation of the ellipse could be corrected.

To conclude, the proposed battery of tests may be useful to characterize the metrological accuracy of the MIMU signals by exploiting simple hypotheses based on their physical working principles. In addition, each test could be conducted without the need of specialized laboratories and expensive equipment.

2.4 Limitations

Some limitations prevent the proposed characterization tests from being general. In fact, the accelerometer is tested only in static conditions, i.e., $\boldsymbol{a}_{body} = 0$, and at $\boldsymbol{a}_{body} = \boldsymbol{g}$ which are easy to replicate and do not require any instrument. A complete analysis would also include measurements for both intermediate values of $\boldsymbol{a}_{body}$ and higher than $\boldsymbol{g}$ which can be imposed using a rotor. However, this would come with inherent uncertainty since the gravity vector must be removed from the accelerometer readings to compare the $\boldsymbol{a}_{body}$ with the reference value. For this purpose, the inclination should be computed using a sensor fusion algorithm which in turn is affected by the choice of its parameter values (Caruso, Sabatini, Laidig, et al., 2021). For values of $\boldsymbol{a}_{body}$ different from zero, the evaluation is limited to the measurement norm only. As for the accelerometer, also the gyroscope tests should be repeated at different angular velocities. In this case, the rotation plate could be programmed to provide the reference values for a range of $\boldsymbol{\omega}_{body}$. The only disadvantage is represented by the long time required to acquire all the data since it is advisable to perform the

rotations for a long enough period to minimize the uncertainty in the identification of the starting and ending points. Furthermore, the magnetometer tests require a constant and clean magnetic field, which is a reasonable hypothesis when experiments are conducted outdoor but more difficult to fulfill indoor where usually the tests are executed (Kok & Schon, 2016). Finally, the MIMU output model described by equations (2), (3), and (4) do not consider the temperature influence on the sensor readings. Some commercial models directly embed a temperature compensation algorithm in their firmware (such as https://apdm.com/wearable-sensors/). However, the characterization at different temperatures would require a thermal chamber to accurately control the temperature thus resulting in a more expensive experimental setup and in a longer required to repeat the acquisitions at different temperature levels.

Despite some limitations, the characterization tests have the potentiality to assess whether a device should undergo a refinement of its calibration coefficients. Unfortunately, it is difficult to define the values of the acceptability thresholds for each test since up to date it is not completely clear how they affect the final biomechanical outcome. In the future, it could be helpful to follow the inverse approach which means to definite the acceptability range of the biomechanical outcome and then to derive (going backwards) the corresponding accuracy limits for each test. In this way, by performing the characterization test it would be immediately clear which sensor calibration should be refined.

References

Ailneni, S., Kashyap, S. K., Shantha Kumar, N., David Livingstone, D., Aishwarya, N., Varghese, N., & Karthik, K. v. (2019). Characterization of MEMS based Inertial Measurement Unit. *1st International Conference on Range Technology, ICORT 2019*. https://doi.org/10.1109/ICORT46471.2019.9069669

Allan, D. W. (1966). Statistics of Atomic Frequency Standards. *Proceedings of the IEEE*, *54*(2), 221–230. https://doi.org/10.1109/PROC.1966.4634

Aslan, G., & Saranli, A. (2008). Characterization and calibration of MEMS inertial measurement units. *European Signal Processing Conference*, *Eusipco*.

Aydemir, G. A., & Saranli, A. (2012). Characterization and calibration of MEMS inertial sensors for state and parameter estimation applications. *Measurement: Journal of the International Measurement Confederation*, *45*(5), 1210–1225. https://doi.org/10.1016/j.measurement.2012.01.015

Bhatt, D., Aggarwal, P., Bhattacharya, P., & Devabhaktuni, V. (2012). An Enhanced MEMS Error Modeling Approach Based on Nu-Support Vector Regression. *Sensors 2012, Vol. 12, Pages 9448-9466*, *12*(7), 9448–9466. https://doi.org/10.3390/S120709448

Caruso, M., Sabatini, A. M., Knaflitz, M., Gazzoni, M., Croce, U. della, & Cereatti, A. (2021). Orientation Estimation through Magneto-Inertial Sensor Fusion: A Heuristic Approach for Suboptimal Parameters Tuning. *IEEE Sensors Journal*, *21*(3), 3408–3419. https://doi.org/10.1109/JSEN.2020.3024806

Caruso, M., Sabatini, A. M., Laidig, D., Seel, T., Knaflitz, M., della Croce, U., & Cereatti, A. (2021). Analysis of the Accuracy of Ten Algorithms for Orientation Estimation Using Inertial and Magnetic Sensing under Optimal Conditions: One Size Does Not Fit All. *Sensors*, *21*(7), 2543. https://doi.org/10.3390/s21072543

Cereatti, A., Trojaniello, D., & Croce, U. della. (2015). Accurately measuring human movement using magneto-inertial sensors: Techniques and challenges. *2nd IEEE International Symposium on Inertial Sensors and Systems, IEEE ISISS 2015 - Proceedings*, 1–4. https://doi.org/10.1109/ISISS.2015.7102390

El-Sheimy, N., Hou, H., & Niu, X. (2008). Analysis and modeling of inertial sensors using allan variance. *IEEE Transactions on Instrumentation and Measurement*, *57*(1), 140–149. https://doi.org/10.1109/TIM.2007.908635

Flenniken, W. S., Wall, J. H., & Bevly, D. M. (n.d.). *Characterization of Various IMU Error Sources and the Effect on Navigation Performance*.

Foster, C. C., & Elkaim, G. H. (2008). Extension of a two-step calibration methodology to include nonorthogonal sensor axes. *IEEE Transactions on Aerospace and Electronic Systems*, *44*(3), 1070–1078. https://doi.org/10.1109/TAES.2008.4655364

Gander, W., Golub, G. H., & Strebel, R. (1994). Least-squares fitting of circles and ellipses. *BIT Numerical Mathematics 1994 34:4*, *34*(4), 558–578. https://doi.org/10.1007/BF01934268

Gebre-Egziabher, D., Elkaim, G. H., Powell, J. D., & Parkinson, B. W. (2001). A non-linear, two-step estimation algorithm for calibrating solid-state strapdown magnetometers. *International Conference on Integrated Navigation Systems*, 290–297.

Gulmammadov, F. (2009). Analysis, modeling and compensation of bias drift in MEMS inertial sensors. *RAST 2009 - Proceedings of 4th International Conference on Recent Advances Space Technologies*, 591–596. https://doi.org/10.1109/RAST.2009.5158260

Han, J., Ge, S., Shen, Y., & Li, X. (2006). Modeling and simulation of digital closed-loop fiber optic gyroscope. *Proceedings of the World Congress on Intelligent Control and Automation (WCICA)*, *1*, 1659–1663. https://doi.org/10.1109/WCICA.2006.1712634

Hiller, T., Pentek, Z., Liewald, J. T., Buhmann, A., & Roth, H. (2019). Origins and Mechanisms of Bias Instability Noise in a Three-Axis Mode-Matched MEMS Gyroscope. *Journal of Microelectromechanical Systems*, *28*(4), 586–596. https://doi.org/10.1109/JMEMS.2019.2921607

Hussen, A. A., & Jleta, I. N. (2015). Low-Cost Inertial Sensors Modeling Using Allan Variance. *International Scholarly and Scientific Research & Innovation*, *9*(5), 1069–1074.

IEEE Aerospace and Electronic Systems Society. Gyro and Accelerometer Panel., & Institute of Electrical and Electronics Engineers. (1998). *IEEE standard specification format guide and test procedure for single-axis interferometric fiber optic gyros*. 75.

IEEE Standard for Sensor Performance Parameter Definitions. (2018). *IEEE Std 2700-2017 (Revision of IEEE Std 2700-2014)*, 1–64. https://doi.org/10.1109/IEEESTD.2018.8277147

Kirkko-Jaakkola, M., Collin, J., & Takala, J. (2012). Bias prediction for MEMS gyroscopes. *IEEE Sensors Journal*, *12*(6), 2157–2163. https://doi.org/10.1109/JSEN.2012.2185692

Kok, M., Hol, J. D., Schön, T. B., Gustafsson, F., & Luinge, H. (2012). Calibration of a magnetometer in combination with inertial sensors. *2012 15th International Conference on Information Fusion*, 787–793.

Kok, M., & Schon, T. B. (2016). Magnetometer calibration using inertial sensors. *IEEE Sensors Journal*, *16*(14), 5679–5689. https://doi.org/10.1109/JSEN.2016.2569160

Lebel, K., Boissy, P., Hamel, M., & Duval, C. (2013). Inertial measures of motion for clinical biomechanics: Comparative assessment of accuracy under controlled conditions - Effect of velocity. *PLoS ONE*, *8*(11). https://doi.org/10.1371/journal.pone.0079945

Mazzà, C., Alcock, L., Aminian, K., Becker, C., Bertuletti, S., Bonci, T., Brown, P., Brozgol, M., Buckley, E., Carsin, A.-E., Caruso, M., Caulfield, B., Cereatti, A., Chiari, L., Chynkiamis, N., Ciravegna, F., del Din, S., Eskofier, B., Evers, J., … Rochester, L. (2021). Technical validation of real-world monitoring of gait: a multicentric observational study. *BMJ Open*, *11*(12), e050785. https://doi.org/10.1136/bmjopen-2021-050785

Nez, A., Fradet, L., Laguillaumie, P., Monnet, T., & Lacouture, P. (2016). Comparison of calibration methods for accelerometers used in human motion analysis. *Medical Engineering and Physics*, *38*, 1289–1299. https://doi.org/10.1016/j.medengphy.2016.08.004

Nez, A., Fradet, L., Laguillaumie, P., Monnet, T., & Lacouture, P. (2018). Simple and efficient thermal calibration for MEMS gyroscopes. *Medical Engineering & Physics*, *55*, 60–67. https://doi.org/10.1016/J.MEDENGPHY.2018.03.002

Nikolic, J., Furgale, P., Melzer, A., & Siegwart, R. (2016). Maximum Likelihood Identification of Inertial Sensor Noise Model Parameters. *IEEE Sensors Journal*, *16*(1), 163–176. https://doi.org/10.1109/JSEN.2015.2476668

Parvis, M., & Ferraris, F. (1995). Procedure for effortless in-field calibration of three-axial rate gyro and accelerometers. *Sensors and Materials*, *7*(5), 311–330.

Quinchia, A. G., Falco, G., Falletti, E., Dovis, F., & Ferrer, C. (2013). A Comparison between Different Error Modeling of MEMS Applied to GPS/INS Integrated Systems. *Sensors (Basel, Switzerland)*, *13*(8), 9549. https://doi.org/10.3390/S130809549

Stančin, S., & Tomažič, S. (2014). Time- and computation-efficient calibration of MEMS 3D accelerometers and gyroscopes. *Sensors (Switzerland)*, *14*(8), 14885–14915. https://doi.org/10.3390/s140814885

Unsal, D., & Demirbas, K. (2012). Estimation of deterministic and stochastic IMU error parameters. *Record - IEEE PLANS, Position Location and Navigation Symposium*, 862–868. https://doi.org/10.1109/PLANS.2012.6236828

Walther, A., le Blanc, C., Delorme, N., Deimerly, Y., Anciant, R., & Willemin, J. (2013). Bias contributions in a MEMS tuning fork gyroscope. *Journal of Microelectromechanical Systems*, *22*(2), 303–308. https://doi.org/10.1109/JMEMS.2012.2221158

Zedda, A., Gusai, E., Caruso, M., Bertuletti, S., Baldazzi, G., Spanu, S., Riboni, D., Pibiri, A., Monticone, M., Cereatti, A., & Pani, D. (2020). DoMoMEA: A Home-Based Telerehabilitation System for Stroke Patients. *Proceedings of the Annual International Conference of the IEEE Engineering in Medicine and Biology Society, EMBS*, *2020-July*, 5773–5776. https://doi.org/10.1109/EMBC44109.2020.9175742

Appendix (Chapter 2)

The case dimensions are reported in Figure 19. The case was manufactured using a fused deposition modeling.

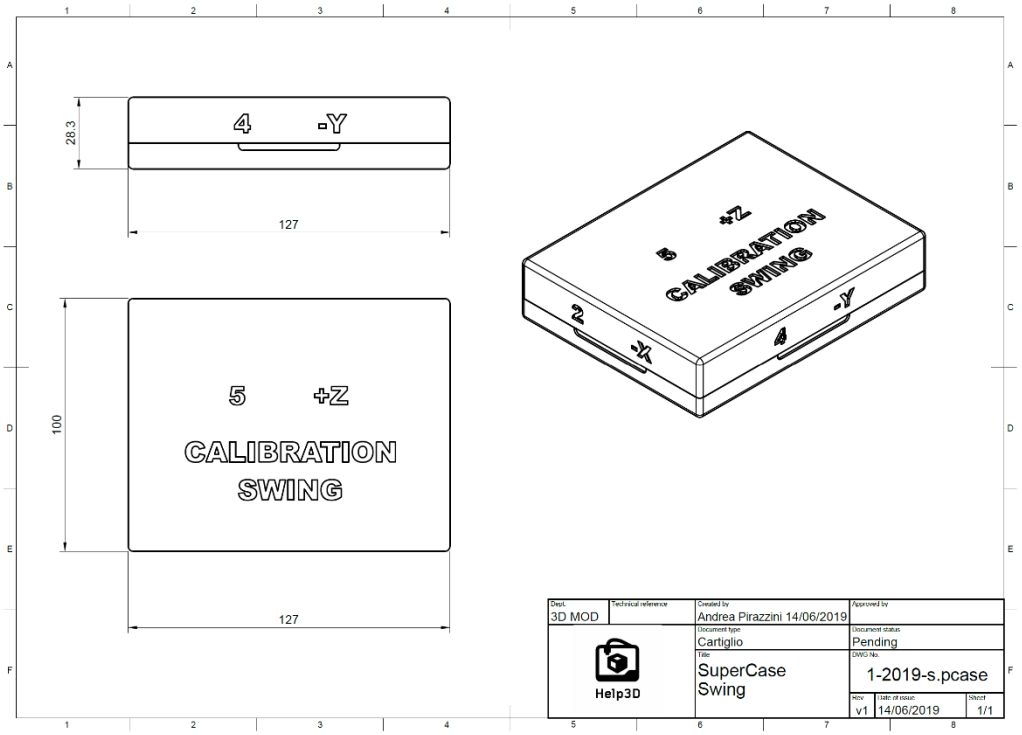

Figure 19: the specifications of the case developed to host up to 4 MIMUs.

The 3D model of designed rotation plate is reported in Figure 20. The servo motor SPT5325lv-360 was selected since it allows continuous rotations and reported in Figure 21, more specifications are available at (https://www.teknistore.com/en/rc-helicopter-parts/52233-spt-servo-spt5325lv-360-25kg-digital-servo-360-large-torque-dual-bearing-linear-change-metal-gear-servo.html, last accessed 25th March, 2022).

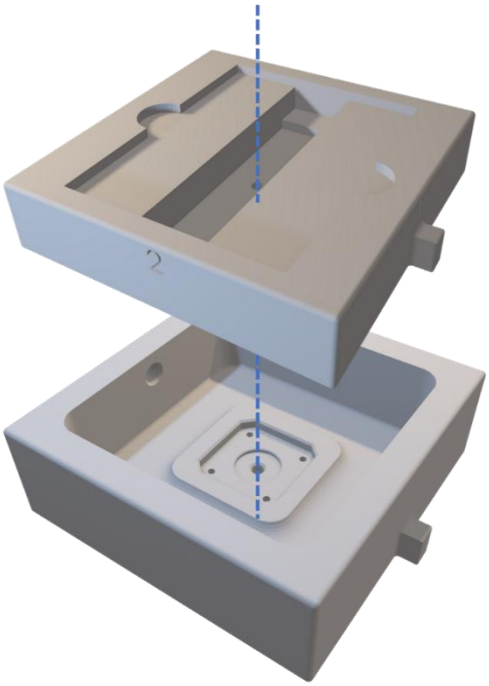

Figure 20: the designed part of the rotation plate.

Figure 21: the digital servo SPT5325LV-360

Chapter 3

Orientation estimation: the sensor fusion approach

3.1 Introduction

The methods and the results presented in this chapter have been published in (Caruso, Sabatini, Knaflitz, della Croce, et al., 2021; Caruso, Sabatini, Knaflitz, Gazzoni, et al., 2021; Caruso, Sabatini, Laidig, et al., 2021; Laidig et al., 2021).

The measurements of the accelerometer, gyroscope, and magnetometer can be combined to estimate the three-dimensional orientation of a MIMU and, in general, of the rigid body on which it is attached. This step is fundamental to compute joint angles but also to remove the gravity vector from the accelerometer signals so that linear velocity and displacement can be calculated. The orientation is usually estimated using a sensor fusion algorithm (SFA), also known as filter, which exploits the strengths and weakness of each sensor embedded in a MIMU. Several SFAs have been proposed in the literature and the large majority of them belongs to the complementary or Kalman filtering families. The difference among the implementations consists in the orientation parametrization (such as orientation matrices, quaternions, Euler angles, …) different formulations of the Kalman filter (e.g., linear, extended, unscented, direct, indirect, …), and different fusing strategy (i.e., optimization or algebraic). A lot of studies have been published over the decades to compare the performance of the different SFAs, but contradictory results have been obtained up to date and no conclusions can be found about the potential orientation accuracy when using MIMUs (Bergamini et

al., 2014; Lebel et al., 2013, 2015; Ludwig & Burnham, 2018; Nazarahari & Rouhani, 2020; Ricci et al., 2016; Weber et al., 2020; Young, 2009). These differences can be explained by the fact that, to work efficiently, each SFA requires that the values of the parameters which govern the sensor fusion process are properly set. In fact, it has been observed that several intrinsic and extrinsic factors affect the parameter value choice, including amplitude of motion, sensors noise strength, and the intensity of ferromagnetic disturbances (Cavallo et al., 2014). However, the selection of the most suitable values is not trivial, and no common procedure exists thus making the generalization of the results impossible. One possible approach consists in finding the so-called optimal values by minimizing the error between the estimated and the ground truth orientation for a specific recording. The first part of this chapter deals with a comprehensive comparative evaluation of the orientation accuracy of ten SFAs chosen among the most popular algorithms proposed in the literature. To ensure a "fair" and generalizable comparison, all the SFA parameters were selected based on the optimal tuning performed on the specific dataset. This ensured that the performance of each SFA was tested under its best possible conditions. Moreover, to assess the error dependency on the specific experimental scenarios, three different pairs of commercial MIMUs and three rotation intensities were considered. The orientation reference was provided by a multi camera SP system used as a ground-truth. To conclude this part, the computation time required by each SFA to execute a single orientation was also evaluated.

The second part of this chapter shows the results of a procedure aimed at estimating the most suitable SFA parameter values without using the gold standard orientation. In fact, despite the optimal approach provides the lowest possible errors, it may not be feasible for a lot of applications where the ground-truth orientation is not available, e.g., during the real-world assessment of the patients' mobility which is typically performed out of the laboratory (Mazzà et al., 2021). To this end a heuristic procedure for a suboptimal estimation of the parameter values was designed by the author without relying on any orientation reference. This approach, called "rigid-constraint" exploits the hypothesis that two MIMUs aligned on a rigid body have a null orientation during the entire recording. Given a generic SFA, by computing the orientation of each MIMU for different values of its parameter it is assumed that the values which minimize the relative orientation difference could be selected as the one which also guarantee for small absolute errors. The rigid-constraint method was tested on the same ten

SFAs and on the same experimental scenarios considered for the comparative analysis.

To help the reader's attention, before going through the main concept of this chapter, the first paragraph provides a brief introduction about the fundamentals of the sensor fusion approach to estimate the orientation starting from the MIMU measurements. All the SFAs described in this thesis are based on the quaternions, which is a convenient and fast parametrization of the orientation having only four parameters.

3.2 Sensor fusion fundamentals

To estimate the three-dimensional absolute orientation of a MIMU means to define the rotation between its local coordinate system and the global coordinate system (GCS). The latter is usually defined to have the vertical axis aligned with the gravity direction and one horizontal axis (usually the x-axis) pointing in the direction defined by the projection of the Earth's magnetic north onto the horizontal plane. To this end, the complementary characteristics of the accelerometer, gyroscope, and magnetometer signals are exploited within a sensor fusion framework. A general and schematic overview is provided in Figure 22 which consists of two steps. In the first one, an approximation of the orientation estimate is obtained by the integration of the kinematics equation which links the angular rate with the orientation change over time. The initial conditions for the integration can be set by following an algebraic approach which provides the absolute orientation by using the accelerometer and the magnetometer measurements (Valenti et al., 2015). It is worth pointing out that this operation is reliable only in absence of acceleration and in a magnetic clean environment. Deviations from this condition may result in a poor estimate of the initial orientation. The orientation resulting after the integration of the angular velocity, however, is prone to drift which grows unbounded over time due to the integration of the slow-varying bias affecting the gyroscope signal (Sabatini, 2011). The sensor fusion approach tries to compensate for such drift by exploiting the information of the accelerometer and the magnetometer. The accelerometer is useful for estimating the inclination (resulting from the combination of the roll and pitch angles) by sensing the Earth's gravity in its local coordinate frame, while the magnetometer can be employed to estimate the orientation (i.e., the yaw angle, also known as declination or heading) of the MIMU with respect to the

Earth's magnetic North, acting as a compass. However, these additional observations are not sufficient to free the resulting orientation estimate from the drift. In fact, the inclination estimate is accurate only when the MIMU is stationary, since when the MIMU is in motion, the accelerometer signals are the result of the combination of gravity and the body acceleration. Moreover, the heading information estimated from the magnetometer output can be corrupted by the ferromagnetic disturbances, which arise from the surrounding metallic objects and electric appliances, therefore limiting its indoor use. During the fusion process, the two pieces of orientation (the estimates resulting from the integration of the angular velocity and from the accelerometer/magnetometer, respectively) are then weighted to provide the final estimate. The SFA parameters play a key role at this point by giving more importance to the most reliable sources of information. In general, the parametrization of a SFA is usually employed to communicate the *a-priori* knowledge of the amount of the disturbances affecting each sensor.

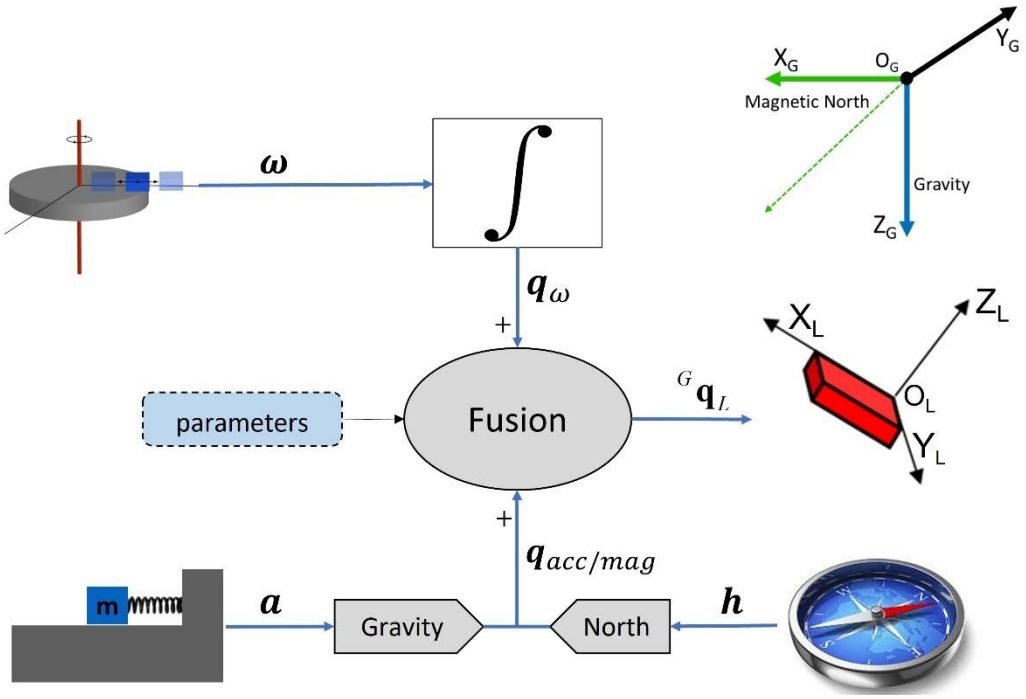

Figure 22: a general overview of the sensor fusion framework.

3.3 A comparative accuracy analysis under optimal conditions

3.3.1 Introduction

As anticipated, the aim of this section is to perform a thorough comparative evaluation of the accuracy of ten of the most popular SFAs proposed in the literature using the orientation provided by a SP system as a reference. For the sake of analysis generalizability, the SFAs performance was assessed under optimal and default parameters tuning. In the optimal tuning configuration, parameters were set by minimizing the absolute orientation error with respect to the ground-truth for each experimental scenario, allowing for the assessment of the filter performance under its best possible conditions. In addition, the errors obtained using the default parameter values as defined by the SFA proponents were also computed to highlight the impact of using non-tuned and generic parameter values for different experimental scenarios. The experimental setup included nine experimental scenarios considering six MIMUs from three different manufacturers and three rotation rate magnitudes. The motions consisted in a mix of 2D and 3D rotations.

3.3.2 Optimal working conditions

To work properly, each SFA requires the tuning of a certain number of parameters (Cavallo et al., 2014). In the present context, optimal working conditions referred to the parameter values which provided the lowest absolute average orientation error for a given experimental data recording (i.e., they were specialized for each dataset) and hence the best achievable performance (best case scenario). In other words, for each SFA each parameter value was optimally tuned on each of the nine experimental scenarios (three rotation rates for three commercial device). The selection of the optimal parameter values was performed relying on the SP orientation. This strategy was implemented exclusively for comparative purposes and may be replicated only with the aid of an orientation reference which in this case was represented by a SP system with sub-millimeter accuracy.

3.3.3 Considered SFAs

A total of ten SFAs were considered to carry out the comparison. The MATLAB (R2020a, The MathWorks Inc., Natick, MA, USA) implementations for each SFA were made available on on MATLAB Exchange (at https://it.mathworks.com/matlabcentral/fileexchange/90351-orientation_estimation_sensor_fusion_algorithm_codes, accessed on 5 April 2022). In summary, five complementary filters (CFs) and five Kalman filters (KFs) were considered, chosen among the most popular:

Complementary filters:

- Mahony et al., 2008 (MAH), with 2 parameters (Mahony et al., 2008).
- Madgwick et al., 2011 (MAD), with 1 parameter (Madgwick et al., 2011).
- Valenti et al., 2015 (VAC), with 9 parameters (Valenti et al., 2015).
- Seel et al., 2017 (SEL), with 4 parameters (Seel & Ruppin, 2017).
- MATLAB complementary filter R2020a (MCF), the implementation of VAC by the MathWorks with only two parameters.

Kalman filters:

- Sabatini 2011 (SAB), with 6 parameters (Sabatini, 2011).
- Ligorio and Sabatini 2015 (LIG), with 6 parameters (Ligorio & Sabatini, 2015).
- Valenti et al., 2016 (VAK), with 3 parameters (Valenti et al., 2016).
- Guo et al., 2017 [20] (GUO), with 3 parameters (Guo et al., 2017).
- MATLAB Kalman filter R2020a (MKF), the implementation by MathWorks of the filter by Roetenberg et al., 2005, with 8 parameters (Roetenberg et al., 2007).

As stated in the introduction, all the SFAs are based on the angular velocity integration to obtain a first approximation of the orientation estimate. The differences are related to how the accelerometer and magnetometer measurements are used to compensate for the drift caused by the time integration of the angular velocity and to additional strategies designed to deal with the linear acceleration and the ferromagnetic disturbances. For the sake of completeness, a short description of each filter is given. This description is entirely taken from (Caruso, Sabatini, Laidig, et al., 2021).

"MAD is a CF in which the accelerometer and the magnetometer measurements are fused by means of a gradient descent algorithm. For the magnetic readings, only the horizontal projection is used to correct the orientation. The fusion process is governed by a unique parameter. A low value of it gives more weight to the gyroscope measurements. MAH is a CF which considers the discrepancy between the measured Earth's fixed vector (gravity and magnetic field) and their estimates obtained using the previous orientation. This discrepancy (called error) is then weighted by a parameter and subtracted from the gyroscope signal before its integration. As opposite to MAD the magnetic readings influence both the attitude and heading. In neither filter it is possible to weigh differently the accelerometer and the magnetometer contributions and no strategy is implemented to compensate for the linear acceleration or the magnetic disturbances. SEL is a CF with independent accelerometer-based inclination correction and magnetometer-based heading correction. The latter is purely horizontal, which ensures that magnetic disturbances cannot affect the inclination. The algorithm is parameterized via two correction constants for the inclination and heading disagreements, one optional bias estimation parameter and an adaptation factor that reduces the weight of the accelerometer readings during dynamic motions. VAC is a CF which employs the accelerometer readings to correct the inclination by comparing the actual and the observed gravity direction. The magnetometer readings are then projected onto the horizontal plane and the angle between the observed magnetic North and the estimated one is used to correct the heading. The two correction processes are governed by two independent gains. VAC implements a linear two-thresholds method to progressively reject the measurements whereas their magnitude exceeds the expected value (i.e., 9.81 m/s2 and the local magnetic norm, respectively). MCF is the implementation of VAC by MathWorks from Sensor Fusion and Tracking Toolbox. VAK, LIG GUO, SAB, and MCF belong to the class of the KFs. As a general rule, the weight given to the information provided by each of the three sensors is governed by dedicated parameters. In particular, the higher is the value of these parameters the less the information provided is trusted. For this reason, they are called "inverse weight". A typical feature of the KF is the possibility to track the disturbances with the "state-vector augmentation technique". While on one hand it represents an advantage, on the other hand each quantity tracked in the state vector must be weighted with dedicated parameters to account for the uncertainty in their modelling and, above all, a large state vector dimension may result in observability problem (i.e., the information contained in the output variables is no longer sufficient to completely describe the system behavior).

VAK employs the same algebraic approach of VAC to correct the orientation, but as opposite to VAC no thresholds are used to reject linear accelerations or ferromagnetic disturbances which are instead employed in SAB. In addition, SAB allows the modelling of the ferromagnetic disturbances, seen as a time-variant bias superimposed to the magnetometer readings. LIG consists of two KFs which separately estimate the inclination and the heading, using the information provided by the gyroscope/accelerometer and gyroscope/magnetometer, independently. The two pieces of information are then merged by using an algebraic method. Linear accelerations and ferromagnetic disturbances are modelled as a first order Gauss-Markov model. GUO is a KF explicitly designed to perform fast. To this end, an algebraic approach which fuses the accelerometer and magnetometer measurements for the orientation correction is adopted and no additional strategy to filter out the linear accelerations and ferromagnetic disturbances is implemented. MKF is the MathWorks implementation (Sensor Fusion and Tracking Toolbox) of the filter originally proposed by Luinge et al., (Luinge & Veltink, 2004)and extended by Roetenberg et al., (Roetenberg et al., 2007) which is also embedded in the Xsens software. Differently from the other four KFs described, MKF is an indirect KF, which means that it minimizes the uncertainty of the orientation error rather than of the absolute orientation (direct formulation). In this filter, the inclination and heading errors are separately computed by comparing the actual and the estimated directions of the gravity and global magnetic field using the information provided by gyroscope/accelerometer and gyroscope/magnetometer, respectively. These two orientation errors are then included in the state vector to be minimized. MKF augments its state vector with the gyroscope bias, acceleration errors (seen as the linear acceleration component in the accelerometer output) and the ferromagnetic disturbances".

For each SFA the two most influencing parameters, namely p_1 and p_2 (selected from those that caused the greatest variation in orientation as their values changed) were tuned following a grid-search approach. The choice of limiting the tuning to at most two parameters was a compromise between the dimension of the search-space and the computational time. The parameter related to the weight given to the gyroscope was always tuned, when exposed by the SFA, since the angular velocity is the most important information in a sensor fusion framework. The additional parameter tuned, when relevant, was selected to weight differently the accelerometer or magnetometer readings, depending on the SFA. As a general consideration, it is not advisable to set the accelerometer and magnetometer related parameters based on the sensor electrical noise only. In fact, the latter is

usually negligible compared to errors due to linear accelerations and the additional magnetic fields. This is also supported by (Nez et al., 2017) where the parameters related to the accelerometer and magnetometer noise were tuned following a grid search approach spanning a large set of values instead of choosing the values corresponding to the amount of electrical noise. The remaining parameters of the ten SFAs have been set to the default values reported in the original articles. Table IV reports the details of the parameters tuned for each SFA together with the default values provided by the SFA authors.

Table IV: the details of the two parameters selected for the optimal tuning along with their default values. #p = number of parameters. Def = default Adapted from [10].

CF	*#p*	p_1	*Def*		p_2	*Def*	
MAH	2	k_p: inverse gyroscope weight	1	rad/s	k_i—weight for online bias estimation	0.3	rad/s
MAD	1	β—inverse gyroscope weight	0.1	rad/s	/	/	
VAC	9	g_{mag}— magnetometer weight	0.01	a.u.	a_{th2}—threshold for accelerometer vector selection	0.2	a.u.
SEL	4	τ_{acc}— accelerometer time constant	1	s	τ_{mag}—magnetometer time constant	3	s
MCF	2	g_{mag}— magnetometer weight	0.01	a.u.	/	/	
KF	*#p*	p_1	*Def*		p_2	*Def*	
SAB	6	σ_{gyr}—inverse gyroscope weight	0.007	rad/s	a_{th}—threshold for accelerometer vector selection	40	mg
LIG	6	σ_{gyr}—inverse gyroscope weight	1	rad/s	c_b—Gauss-Markov variance of external acceleration and ferromagnetic disturbances	1	a.u.

VAK	3	σ_{gyr}—inverse gyroscope weight	0.004	rad/s	σ_{acc}—inverse accelerometer weight	0.014	m/s^2
GUO	3	σ_{gyr}—inverse gyroscope weight	0.001	rad/s	/	/	
MKF	8	σ^2_{gyr}—inverse gyroscope weight	9.14×10^{-5}	$(rad/s)^2$	/	/	

3.3.4 Experimental setup and protocol

Two MIMUs from Xsens – MTw (Xsens, Enschede, The Netherlands), two MIMUs from APDM – OPAL (APDM INC., Portland OR, USA), and two MIMUs from Shimmer – Shimmer3 (Shimmer Sensing, Dublin, Ireland) were aligned on a wooden board at a relative distance of 50 mm. To ensure an accurate positioning of the MIMUs, a T-square was employed to draw the lines. The alignment error due to the orthogonal tolerance of the instrument can be assumed to be lower than 0.2 deg. Eight passive reflective markers (diameter equal to 14 mm, minimum inter-distance of 85 mm) were also placed on the board. In particular, the three central markers (M_0, M_x, M_y) were used to define the SP local coordinate system (LCS), while the redundancy of the remaining makers was exploited to strengthen the orientation estimate obtained using the singular value decomposition technique (Cappozzo et al., 1997). The LCS of the SP was aligned to that of the MIMUs. The board LCS was made to align as the LCS of both MIMUs and SP. The complete board setup is shown in Figure 23. Marker trajectories were acquired by a 12-camera SP system (Vicon T20, VICON, Yarnton, England) to provide the gold-standard orientation. To synchronize the MIMU and SP systems, a force platform integrated with the SP was used. The idea was to exploit a mechanical shock to be recorded simultaneously from the accelerometers and the platform. To this end, the board was placed over an aluminum tripod (to limit the magnitude of the ferromagnetic disturbances).

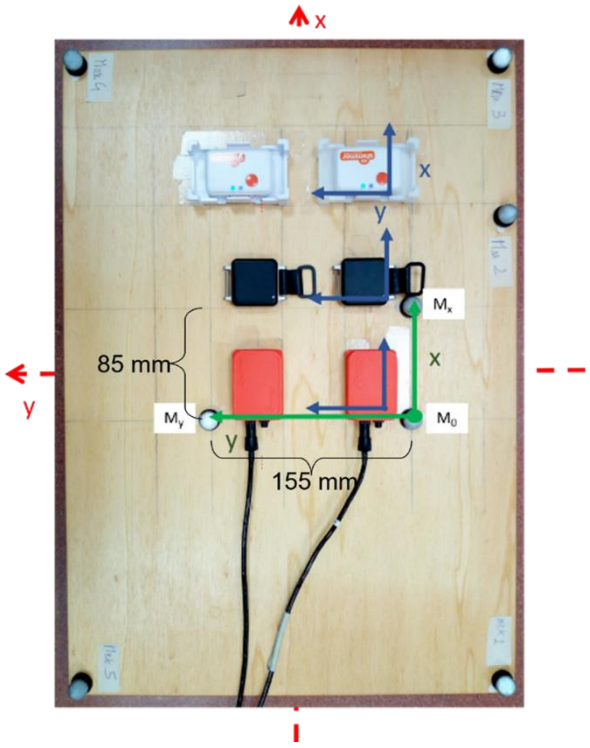

Figure 23: the experimental setup. The LCS of the MIMUs is represented in blue while the LCSs of the SP and of the board are represented in green and red, respectively and were arranged to be parallel with the LCS of the MIMUs. This figure is taken from (Caruso, Sabatini, Knaflitz, della Croce, et al., 2021).

To limit the temperature effects on the sensor readings a ten-minute instrument warm-up was carried out before starting the experiments. After that, a first one-minute measure was acquired to compute the gyroscope bias which was then subtracted from the angular velocities' readings. All the experiments were executed at a constant temperature of about 20 °C. The board was first kept still and horizontal for one minute to allow the filter initialization, then a dynamic trial was recorded while an operator held the board at both ends and performed both single-axis and multiaxial rotations to continuously change the board orientation in space. This protocol was executed at low (RMS 120 dps for 70 s), medium (RMS 260 dps for 45 s), and high rotation rate (RMS 380 dps for 30 s). At the beginning and at end of each recording, two knocks were given to the board to allow the identification of the synchronization points. An example of the performed motion is provided in Figure 24 where the SP orientation is represented using the corresponding Euler angles for the medium rotation rate magnitude.

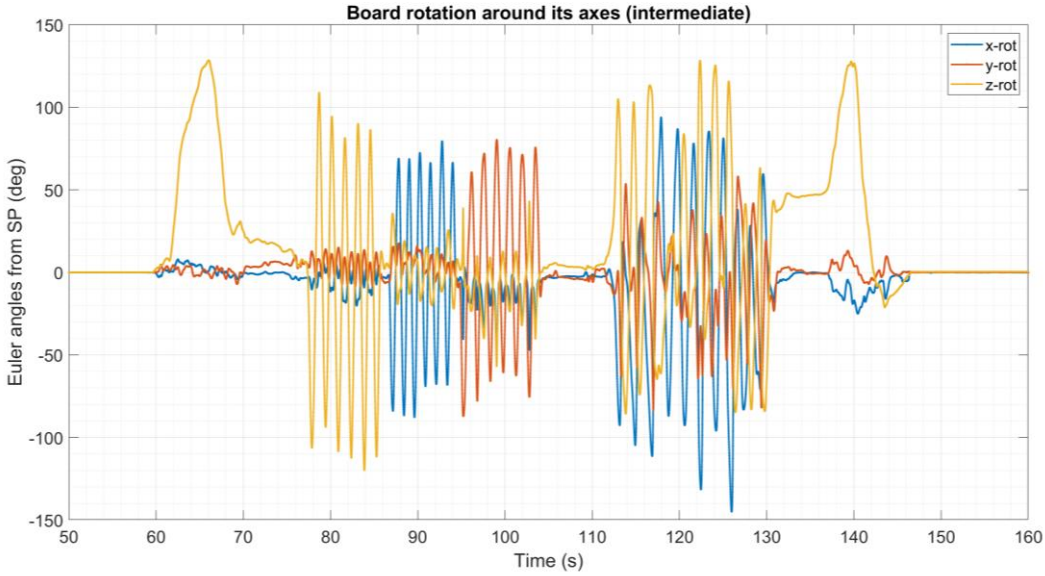

Figure 24: the Euler angles obtained from the SP for the intermediate trial. It is possible to observe that the first three rotations were performed around one axis at a time, while the last is a combination of the movement around the three axes. Figure taken from (Caruso, Sabatini, Knaflitz, della Croce, et al., 2021).

The volume in which the experiments were conducted amounted at about 1 m^3 at a distance greater than 1 m from the floor. For this reason, it was possible to neglect the ferromagnetic disturbances as it was also observed in the post processing. In fact, the magnetometer norm was almost constant, and its maximum difference was limited to 1 μT. All the data were acquired using the proprietary software listed in Table V. The synchronized dataset and the videos of the experimental setup can be found on MATLAB Exchange (https://it.mathworks.com/matlabcentral/fileexchange/91200-mimu_optical_dataset_caruso_sassari, accessed on 5 April 2022).

Table V: the details of the acquisition software and the corresponding sampling frequency for each system

System	***Software***	***Sampling frequency***
SP – Vicon	Nexus v2.7	100 Hz
MIMU – Xsens	MT Manager Version 1.7	100 Hz
MIMU – APDM	Motion Studio Version 1.0.0.201712300	128 Hz (resampled at 100 Hz)
MIMU – Shimmer	Consensys v.1.5.0	100 Hz

The noise of each sensor was characterized during a short static acquisition. Results are reported in Table VI in terms of STD. In addition, the gyroscope bias test was repeated using the samples collected during static at the beginning and at the end of each recording. The differences for each gyroscope and for each axis are reported in Table VII.

Table VI: the noise STD for each sensor. Table adapted from (Caruso, Sabatini, Laidig, et al., 2021).

STD	Accelerometer (mg)			Gyroscope (dps)			Magnetometer (μT)		
	x	y	z	x	y	z	x	y	z
Xsens-MTx (A)	0.86	0.80	0.85	0.38	0.39	0.37	0.06	0.04	0.04
Xsens-MTX (B)	0.82	0.86	0.80	0.44	0.40	0.40	0.05	0.06	0.06
APDM-OPAL (A)	0.38	0.33	0.38	0.16	0.23	0.11	0.26	0.23	0.20
APDM-OPAL (B)	0.34	0.32	0.35	0.16	0.27	0.19	0.26	0.25	0.20
Shimmer-Shimmer 3 (A)	1.06	0.97	1.26	0.09	0.08	0.09	0.84	0.84	0.69
Shimmer-Shimmer 3 (B)	1.12	1.09	1.29	0.06	0.06	0.06	0.97	0.97	0.58

Table VII: results of the difference between the gyroscope bias tests conducted at the beginning and at the end of each recording. Table adapted from (Caruso, Sabatini, Laidig, et al., 2021).

Gyroscope bias difference (dps)	Accelerometer (mg)			Gyroscope (dps)			Magnetometer (μT)		
	x	y	z	x	y	z	x	y	z
Xsens-MTx (A)	0.00	–0.05	0.00	–0.01	0.00	–0.02	–0.01	–0.01	–0.02
Xsens-MTX (B)	0.01	0.01	0.02	0.03	0.00	0.03	–0.01	–0.02	–0.02
APDM-OPAL (A)	0.08	0.04	–0.02	–0.12	–0.02	0.00	–0.02	0.12	–0.01
APDM-OPAL (B)	0.07	0.01	–0.03	–0.17	–0.17	–0.05	–0.09	–0.03	–0.10
Shimmer-Shimmer 3 (A)	–0.01	–0.03	0.00	–0.01	0.00	0.00	0.00	–0.01	0.00
Shimmer-Shimmer 3 (B)	–0.01	–0.03	0.01	–0.01	–0.03	0.01	–0.01	–0.03	0.03

3.3.5 Data processing

Signal pre-processing and synchronization

Data processing was entirely carried out in MATLAB except for the optical data which, after being labelled and gap-filled in Nexus, were low-pass filtered using a zero-phase Butterworth filter of the 6th order (cut-off frequency set to 6 Hz as suggested in (Bergamini et al., 2014)) to remove high frequency noise. The synchronization between the SP and the MIMU signals was performed in two steps: firstly, all data were delimited by finding the two acceleration and force

peaks recorded by the vertical axes of the accelerometer and force plate, respectively. Afterward, the signals were linear interpolated at 100 Hz. To refine the synchronization, the signals of each MIMU were aligned with the SP data by cross-correlating the angular velocity recorded by each gyroscope and that estimated by the central markers as described in (Chardonnens et al., 2012). As anticipated, the SP orientation was estimated by means of a singular value decomposition-based technique (Cappozzo et al., 1997). The resulting gold standard orientation ($\boldsymbol{q}_{SP_G}$) was expressed using quaternion. By considering the cluster size of the three central markers and that the errors in the recorded marker position amounted to about 0.1 mm (Chiari et al., 2005), after trigonometry considerations it was possible to assume that the uncertainty which affected the gold standard was limited to 0.5 deg. The accuracy of each accelerometer calibration was assessed by performing the gravity test in static. Since the d_{norm} did not exceed 2 mg, all the accelerometers were considered as properly calibrated. The accuracy of the magnetometer calibration was assessed by performing the sphere test. Since the $h_{norm_{STD}}$ never exceeded 0.1 μT, the magnetometers were considered as properly calibrated.

MIMU orientation estimation and error computation under optimal conditions

The grid-search procedure used to obtain the set of orientations for each SFA for each of the nine experimental scenarios (i.e., 3 rotation rates × 3 device models) is detailed below and graphically represented in Figure 25. Quantities highlighted in bold are intended to be vectors or matrices.

An algebraic quaternion, obtained with the algorithm described in (Valenti et al., 2015) was used to initialize the orientation of each MIMU to reduce the convergence time. For each MIMU (A and B) the absolute orientation ($\boldsymbol{q}_{\mathbf{A}_G}$ and $\boldsymbol{q}_{\mathbf{B}_G}$) was computed separately for every combination of the values of the two parameters (stored in $\boldsymbol{p}_{\mathbf{1vec}}$ and $\boldsymbol{p}_{\mathbf{2vec}}$, respectively) from 0 to $upper_1$ and from 0 to $upper_2$, respectively. In general, the two upper limits were chosen large enough to ensure that all the relevant search space was explored. The values of $upper_1$ and $upper_2$ can be observed in the figures of the Appendix at the end of this chapter. The lower limit for all the SFAs was set to zero but for a_{th2} of VAC which was set to the value of the first threshold for the accelerometer measurements (a lower value would be meaningless since for the constraint is $a_{th2} \geq a_{th1}$). The average number of combinations explored, i.e., length($\boldsymbol{p}_{\mathbf{1vec}}$) × length($\boldsymbol{p}_{\boldsymbol{2vec}}$), was not the same for all the SFAs since it was a trade-off between

computational costs and the search space size (on average it amounts to 360 combinations). Since the GCSs of the MIMU and SP were not aligned on the horizontal plane, to enable a meaningful comparison between the orientation obtained for the two systems, it was necessary to refer the latter to a common GCS. To this end, it was possible to benefit from the accurate alignment of the LCS of each system. Therefore, $\boldsymbol{q}_{\mathbf{A}_G}$, $\boldsymbol{q}_{\mathbf{B}_G}$, and $\boldsymbol{q}_{\boldsymbol{SP}_G}$ were separately referred to their initial frame to obtain $\boldsymbol{q}_{\mathrm{A}}$, $\boldsymbol{q}_{\mathbf{B}}$, and $\boldsymbol{q}_{\boldsymbol{SP}}$, respectively, as follows (the $\otimes$ and * operators represent the product and complex conjugate operator in the quaternion algebra, respectively):

$$\begin{aligned} \boldsymbol{q}_{\mathrm{A}} &= \boldsymbol{q}_{\mathbf{A}_G}(1)^* \otimes \boldsymbol{q}_{\mathbf{A}_G}, \\ \boldsymbol{q}_{B} &= \boldsymbol{q}_{B_G}(1)^* \otimes \boldsymbol{q}_{B_G}, \\ \boldsymbol{q}_{\mathrm{SP}} &= \boldsymbol{q}_{\mathbf{SP}_G}(1)^* \otimes \boldsymbol{q}_{SP_G}. \end{aligned} \tag{18}$$

The absolute orientation errors $\Delta\boldsymbol{q}_{\boldsymbol{abs}\,\mathbf{A}}$ and $\Delta\boldsymbol{q}_{\boldsymbol{abs}\,\mathbf{B}}$ were computed in the quaternion form as follows:

$$\begin{aligned} \Delta\boldsymbol{q}_{\boldsymbol{abs}\,\mathbf{A}} &= \boldsymbol{q}_{\mathbf{A}}^* \otimes \boldsymbol{q}_{\boldsymbol{SP}}, \\ \Delta\boldsymbol{q}_{\boldsymbol{abs}\,\mathbf{B}} &= \boldsymbol{q}_{\mathbf{B}}^* \otimes \boldsymbol{q}_{\boldsymbol{SP}}. \end{aligned} \tag{19}$$

To obtain a compact and interpretable representation of $\Delta\boldsymbol{q}_{\boldsymbol{abs}\,\mathbf{A}}$, $\Delta\boldsymbol{q}_{\boldsymbol{abs}\,\mathbf{B}}$ and $\Delta\boldsymbol{q}_{\boldsymbol{rel}\,\mathrm{A},\mathbf{B}}$, the scalar part of each quaternion was converted into the corresponding rotation described using the axis-angle representation. Then, the RMS of the dynamic parts of the recordings were considered to obtain a single value for each of the three quantities. The two absolute errors (in degrees) were then averaged to obtain $\mathrm{e}_{i,\mathrm{j}}$, which is the absolute mean error for a given combination of the two parameter values. The matrix $\boldsymbol{e}$ was populated for each combination of the values contained in $\boldsymbol{p}_{\mathbf{1vec}}$ and $\boldsymbol{p}_{\mathbf{2vec}}$. All values were rounded to a 0.1 deg resolution.

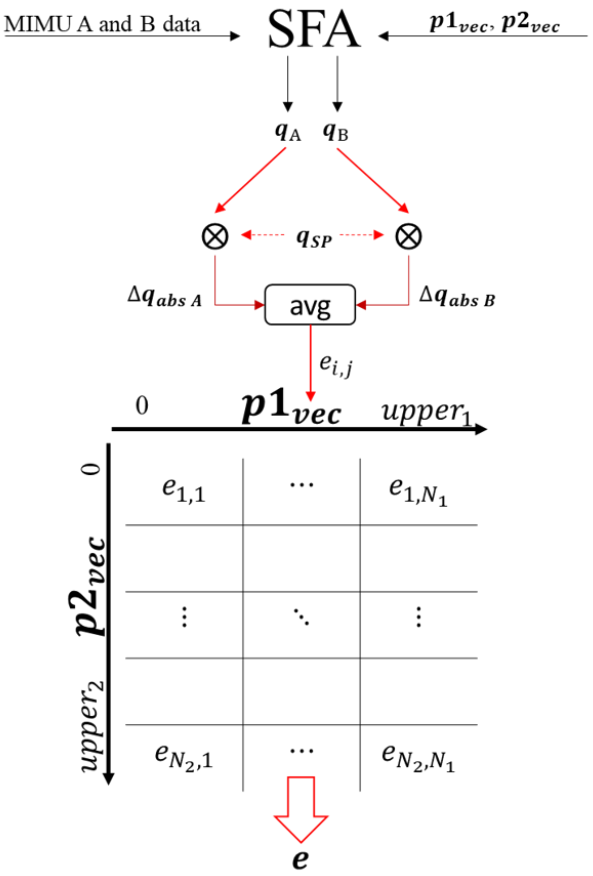

Figure 25: the optimal grid search approach adopted to obtain the absolute orientation error for a given combination of the two parameter values. This process has been applied to each SFA for each of the nine experimental scenarios. avg = average. Figure adapted from (Caruso, Sabatini, Knaflitz, della Croce, et al., 2021).

3.3.6 Data analysis

This section describes the evaluation of the algorithms' performance. Firstly, the optimal regions and the corresponding errors were identified for each SFA and for each experimental scenario. This resulted in 90 optimal errors in total (i.e., 10 SFAs × 3 rotations rates × 3 commercial devices). In parallel, the errors corresponding to the default value were also computed thus obtaining 90 additional values. The default parameters were set as indicated by the proponent in their papers or in the original implementations of their SFAs. Then, considering the optimal errors, the influence of the following factors on the absolute orientation accuracy was analyzed:

- SFA analytical formulation.
- Rotation rate magnitude
- Different commercial devices.

To this extent, a statistical analysis was performed by aggregating data according to the influencing factor under inspection. Finally, the time needed by each SFA to compute a single update iteration was measured and compared among all the SFAs.

Optimal region identification and corresponding errors

The optimal region, for each scenario, is defined as the combination of $\boldsymbol{p_1}$ and $\boldsymbol{p_2}$ which corresponds to the minimum of absolute orientation error.

For each scenario, the following quantities were determined:

- Minimum absolute orientation error which corresponds to the selection of the optimal parameter values: $e_{opt} = \min(\boldsymbol{e})$. In other words, e_{opt} is the lowest error achievable when both parameter values are optimally tuned.

- Optimal parameter region is defined as the range of parameter values whose combinations provide errors within [e_{opt}, e_{opt} + 0.5 deg], where 0.5 is the uncertainty related to the ground-truth errors: $\{p_{opt_1}, p_{opt_2}\} = \{(\boldsymbol{p_{1vec}}, \boldsymbol{p_{2vec}}) \mid \boldsymbol{e} \leq e_{opt} + 0.5\, deg\}$. When only one parameter was tuned (MAD, VAC, GUO, MKF) $\boldsymbol{e}$ was a vector and the optimal region degenerated into a 1D interval.

An example of optimal region is illustrated in Figure 26 for the VAK filter.

Default errors identification

The absolute error corresponding to the default values of $(p_{1_{DEF}}, p_{2_{DEF}})$ was obtained as: $e_{DEF} = \boldsymbol{e}(p_{1_{DEF}}, p_{2_{DEF}})$.

Statistical analysis to evaluate the influence of the SFAs and of the experimental factors

To evaluate the influence of the different factors on the orientation accuracy the 90 values of e_{opt} were aggregated as follows.

- SFA: 10 distributions (one for each SFA) consisting of 9 values each (3 rotation rates × 3 commercial devices).

- Rotation rate: 3 distributions (one for each rotation rate) consisting of 30 values each (10 SFAs × 3 commercial devices).
- Commercial device: 3 distributions (one for each commercial device) consisting of 30 values each (10 SFAs × 3 rotation rates).

The Shapiro-Wilk's test was employed to test the normality of the distributions for each influencing factor. Since the normality condition was not fulfilled, the nonparametric Friedman's test was applied to assess whether significant differences existed among the error distributions. When the null hypothesis was rejected, post-hoc multiple comparison tests were applied to perform pairwise comparisons. More in detail, to test the SFA influence, the Tukey's honest significant difference criterion was used since it is less strict than Bonferroni having 10 distributions (Lee & Lee, 2018). On the contrary, Bonferroni's correction was used when testing the rotation rate and commercial device effects.

Computation time for each SFA

The average time required by each SFA to perform for a single iteration was measured for an Intel® Core™ i7-10510U CPU @ 1.80 GHz (Intel ©, Santa Clara CA, U.S.A.) —Microsoft™ Windows 10 (Microsoft ©, Redmond, WA, U.S.A.) when processing a dataset of 25386 samples without executing any other programs.

3.3.7 Results

Optimal vs default errors

The minimum absolute errors (e_{opt}) and the errors corresponding to default parameter values (e_{def}) are reported in Table VIII for each SFA and for each experimental scenario.

Table VIII: the optimal and default errors obtained for each SFA and for each experimental scenario. All the units are in degrees.

		CF	e_{opt}	e_{def}	**KF**	e_{opt}	e_{def}
Xsens	Slow	MAH	2.5	4.2	SAB	2.2	67.9
	Medium		2.4	11.9		2.1	96.6
	Fast		4.0	13.0		2.4	53.9
APDM	Slow		3.8	3.9		5.0	77.5
	Medium		4.8	17.7		5.7	62.6
	Fast		8.2	12.3		8.3	9.9
Shimmer	Slow		3.4	5.9		4.5	71.1
	Medium		4.6	38.2		4.9	14.5
	Fast		7.6	17.0		8.5	30.0
Xsens	Slow	MAD	2.7	4.7	LIG	1.9	3.7
	Medium		2.5	5.2		2.0	3.9
	Fast		4.0	6.8		2.9	4.8
APDM	Slow		3.8	4.1		3.6	3.6
	Medium		4.6	4.6		4.9	5.0
	Fast		8.1	8.2		4.6	4.6
Shimmer	Slow		3.9	4.3		4.4	4.4
	Medium		4.9	5.2		4.0	4.2
	Fast		8.8	8.9		6.3	6.5
Xsens	Slow	VAC	4.0	4.1	VAK	1.2	22.3
	Medium		5.0	5.9		1.6	21.4
	Fast		7.2	10.0		2.5	72.8
APDM	Slow		3.5	3.6		3.6	29.6
	Medium		6.1	11.8		6.0	30.4
	Fast		8.3	15.1		9.2	81.9
Shimmer	Slow		3.8	3.8		4.0	32.6
	Medium		10.2	19.2		4.4	48.8
	Fast		11.5	23.6		8.2	100,1
Xsens	Slow	SEL	3,1	4,0	GUO	2,3	3,7

	Medium		2,5	4,6	2,3	4,9
	Fast		5,1	6,7	5,7	10,6
APDM	Slow		3,7	3,8	4,2	4,5
	Medium		7,1	7,3	5,1	5,3
	Fast		8,0	8,8	9,4	12,0
Shimmer	Slow		3,4	3,5	4,0	4,0
	Medium		5,0	8,4	5,1	5,7
	Fast		9,4	11,8	13,7	16,7
Xsens	Slow		3,3	4,5	4,2	4,9
	Medium		6,1	6,2	4,8	8,7
	Fast		6,6	7,8	6,7	10,9
APDM	Slow	MCF	3.8	4.2	3.6	4.8
	Medium		12.3	12.3	5.3	14.3
	Fast		7.9	9.3	7.2	10.7
Shimmer	Slow		5.0	5.2	3.9	5.8
	Medium		10.0	10.1	8.4	45.2
	Fast		8.6	12.0	9.9	19.0

Optimal regions

The optimal regions for each SFA are reported in the figures in Appendix of this chapter (left column) for sake of completeness. In particular, the optimal regions are diversified using different colors for experimental scenario. Figure 26 provides an example of the optimal regions identified by p_{opt_1} and p_{opt_2} determined for each of the nine experimental scenarios in the case of VAK.

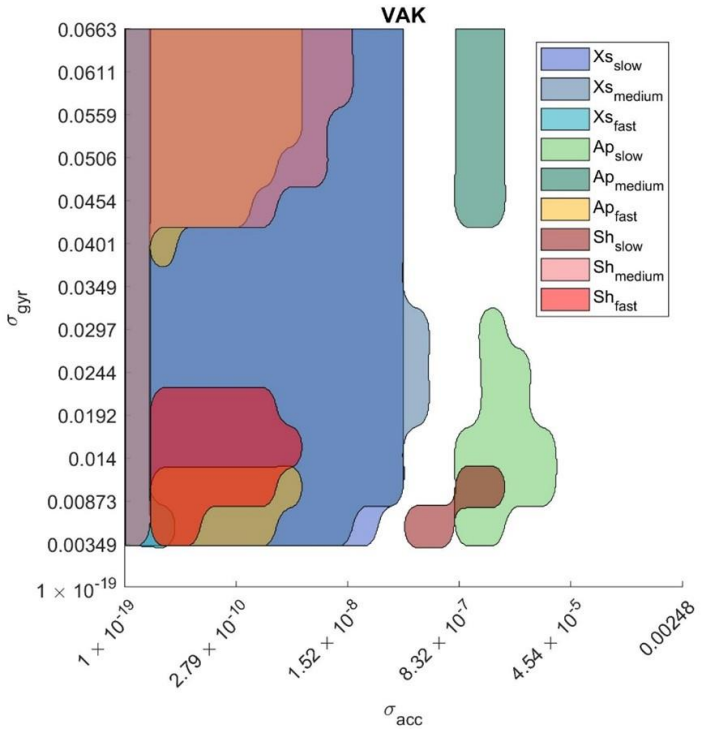

Figure 26: the optimal regions identified for VAK using different colors for each experimental scenario. Figure taken from (Caruso, Sabatini, Laidig, et al., 2021).

Influence of the specific SFA (3 rotation rates × 3 commercial devices)

Mean ± STD of the e_{opt} values obtained by each SFA are represented in ascending order in Figure 27.

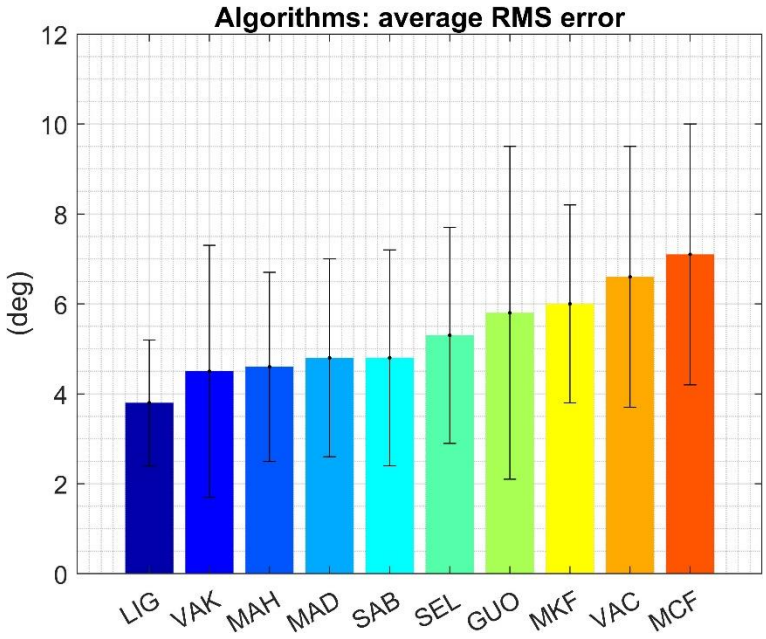

Figure 27: the mean ± STD of the optimal errors obtained by each SFA.

For what concerns e_{def}, by observing Table VIII, it is evident that the default parameters led to high errors in many situations. For this reason, the investigation of the rotation rate and commercial device influence, performed in the following sections, was limited to e_{opt} distributions only (it would be meaningless for those of e_{def}).

The Shapiro-Wilk test, ($\alpha = 0.05$) revealed that not all the e_{opt} distributions were normal ($p < 0.05$). The small p-value (0.0035) resulting from the Friedman's test cast doubts on the validity of the null hypothesis. A multiple comparison test with Tukey's correction ($\alpha = 0.05$) revealed that no statistically significant differences existed among the 10 SFAs under optimal working conditions.

Influence of the rotation rate (10 SFAs × 3 commercial devices)

The mean ± STD errors for slow, medium, and fast rotation rate magnitude are reported in Table IX.

Table IX: the mean ± STD of the optimal errors obtained for each rotation rate magnitude

(deg)	Slow	Medium	Fast
e_{opt}	3.5 ± 0.9	5.2 ± 2.5	7.3 ± 2.6

The Shapiro-Wilk test, ($\alpha = 0.05$) revealed that not all distributions were normal ($p < 0.05$). The small p-value ($<1 \times 10^{-9}$) resulting from the Friedman's test cast doubts on the validity of the null hypothesis. A multiple comparison test with Bonferroni's correction ($\alpha = 0.05$) revealed a statistically significant difference among the three distributions (Table X).

Table X: Results of Friedman's test with Bonferroni's correction to investigate the differences among the three rotation rate conditions.

Scenario	Optimal conditions
Slow vs fast	Significantly different ($p < 1\times 10^{-4}$)
Slow vs medium	Significantly different ($p < 1\times 10^{-4}$)
Fast vs medium	Significantly different ($p = 0.013$)

Influence of the commercial device (10 SFAs × 3 rotation rates)

The mean ± STD errors obtained for the Xsens, APDM, and Shimmer are reported in Table XI.

Table XI: the mean ± STD of the optimal errors obtained for each commercial device.

(deg)	Xsens-MTx	APDM-Opal	Shimmer-Shimmer 3
e_{opt}	3.5 ± 1.7	6.0 ± 2.3	6.5 ± 2.8

The Shapiro-Wilk test, ($\alpha = 0.05$) revealed that not all the distributions were normal ($p < 0.01$). The small p-value ($<1\times 10^{-7}$) resulting from the Friedman's test cast doubts on the validity of the null hypothesis. A multiple comparison test with Bonferroni's correction ($\alpha = 0.05$) revealed a statistically significant difference among the three distributions (Table 8).

Table XII: Results of Friedman's test with Bonferroni's correction to investigate the differences among the three commercial device conditions.

Scenario	Optimal conditions
Xsens vs APDM	Significantly different ($p < 1\times 10^{-5}$)
Xsens vs Shimmer	Significantly different ($p < 1\times 10^{-6}$)
APDM vs Shimmer	Not significantly different ($p = 1$)

Average computation time of each SFA

The average computation time required by each SFA to perform a single update iteration is reported in Figure 28.

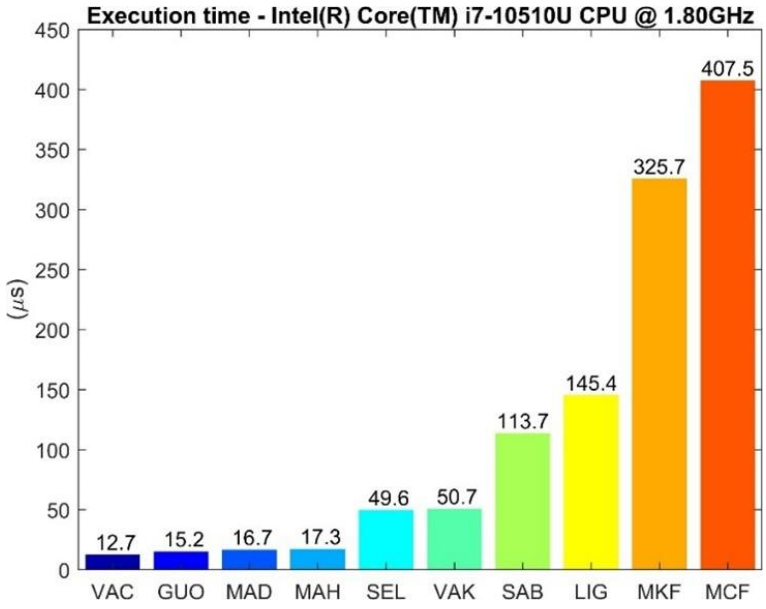

Figure 28: average computation time for each SFA. Figure taken from (Caruso, Sabatini, Laidig, et al., 2021).

3.3.8 Discussion

The importance of an appropriate tuning for each SFA

One of the main findings of this study consisted in the confirmation that the selection of appropriate parameter values is central in determining the level of orientation accuracy and that parameters must be tuned differently based on the experimental conditions under analysis (Olivares et al., 2016; Ricci et al., 2016),

to obtain high performance. In addition, it was observed that each SFA exhibits its optimal performance only for a limited interval of its parameter values. When varying the experimental conditions, the parameters optimized for a different scenario may lead to huge errors. This was noticed for all the SFA but for the MKF which exhibited a common intersection between σ_{gyr}^2 = [0.0125, 0.0275] (rad/s)^2. The figures reported in the left column of the Appendix highlighted the absence of a common intersection among the optimal regions for different experimental scenarios. For some SFAs this was particularly critical since the optimal regions overlapped for a very limited portion. Furthermore, the errors computed using the default parameter values (e_{def}) demonstrated the inadequacy to estimate the orientation using fixed parameter values for a given SFA in different experimental conditions. Thus, it is worth noting that when the performance of the SFAs is compared, it is necessary to find a common strategy to properly tune the relevant SFA parameter values otherwise the comparison would be meaningless (errors can amount to more than 100 deg). Finally, the e_{opt} reported in Table VIII represent the minimum values achievable in these specific conditions. Lower errors could be only obtained when considering less challenging scenarios and/or using MIMUs with higher performance. It would also be interesting from a practical point of view to verify the generalizability of the parameter values in similar experimental scenarios. The recent publication of a large dataset including 39 experimental scenarios as described in (Laidig et al., 2021) could help in this perspective. In fact, it is possible to exploit one recording as training data to compute the optimal parameter values for a given SFA and use the same values to assess the orientation errors on the second recording (used as validation data) acquired in the same experimental conditions.

Influence of the specific SFA and experimental conditions on the absolute accuracy

Despite errors ranged from 3.8 deg to 7.1 deg at most no statistically significant differences were found. This was not surprising and may highlight the fact that the best performing SFA could not be identified. Instead, when the parameter values were properly tuned, the obtained performance were similar, regardless of the filtering class or the number of parameters exposed by the SFAs. In this respect, SFAs with a higher number of parameters were not necessarily corresponding to lower errors compared to SFAs with only one parameter. In fact, despite a large number of parameters ideally allow for a better modelling of the different sources of errors, on the other hand, their tuning could be more difficult due to a possible mutual influence. Among the considered SFAs, LIG showed the

lowest average errors while MCF and VAC the highest amounting the differences to lower than 0.5 deg (this was expected being the implementations of the same filter). It is worth pointing out that this experimental design was not conceived to enhance small differences across the performance of ten algorithms due to the weak statistical power. If of interest, several repetitions for each experimental scenario would need to be collected.

It was also observed that the experimental scenario had a strong influence in determining the SFA accuracy level. In particular, different studies have already reported a link between an increase of the rotation rate magnitude and a worsening of the orientation accuracy (Caruso et al., 2019; Cavallo et al., 2014; Lebel et al., 2013, 2015). However, these papers considered only a limited number of SFAs. This effect can be explained by considering the rigid body mechanics in which the acceleration of a generic point (except the center of rotation) is proportional to the amount of the angular velocity. The body acceleration, in turn, is directly reflected on the recorded accelerometer output since it is summed to the gravity vector whose direction can no longer be distinguished. However, in a sensor fusion framework, the gravity direction information is essential to mitigate the inclination drift, in fact when high accelerations are superimposed to the gravity vector the accelerometer contribution becomes detrimental. Some SFAs implement a workaround to avoid this negative effect by rejecting the accelerometer information when the magnitude of its measures overcome a determined threshold value. Despite the simplicity of this solution, the problem is just shifted to the selection of a proper value adding an additional parameter (Fan et al., 2018). Moreover, accelerometer values close to the thresholds may lead to instability problems in the resulting orientation estimates. The effect of the rotation rate magnitude can be observed in the results reported in Table IX where the differences between errors obtained at high and slow rotation rate were always positive amounting to of 3.8 ± 2.1 deg on average. The combination which provided the minimum and maximum worsening were SAB-Xsens and GUO-Shimmer, respectively (0.2 deg vs 9.7 deg, respectively). Furthermore, the three distributions were statistically different (Table X).

Finally, the effect of using different commercial devices was assessed because of the influence that the different noise specifications have on the orientation accuracy (Lebel et al., 2013, 2015). In fact, it is evident from Table VI and Table VII that sensors embedded in different units of the same commercial device have different noise levels despite sharing similar specifications (e.g., resolution,

sensitivity, range, …). This difference is even more evident when sensors embedded in different commercial devices are considered. In particular, the most critical factor is represented by the difference exhibited by the gyroscope bias in the limited amount of elapsed time between the beginning and the end of each recording. The APDM MIMUs exhibited the highest variation (up to two orders of magnitude higher than Xsens) and this could partially explain the significant difference observed in Table XII. In fact, during the sensor fusion process the angular velocity is the most important source of information for estimating the orientation and any instability in the gyroscope measurements would be directly reflected on the resulting orientation estimates. However, these differences in the gyroscope bias could not completely explain the obtained results since exact mechanism with which the noise level is reflected on the absolute accuracy is still not completely clear. Overall, as highlighted in Table XI, the smallest average errors were obtained using Xsens (3.5 deg), while the highest using Shimmer (6.5 deg). To conclude, it is necessary to highlight, as a limitation, that the different MIMU positioning on the board may have an influence on the final orientation accuracy since the body acceleration magnitude is strictly dependent on the relative distance between the body itself and the center of rotation. However, in this work this effect can be considered small since the mean values of the APDM and Shimmer distributions are extremely similar Table XI despite the different locations on the board.

Computation time of the SFAs

In some applications, the estimation of the orientation in "near" real-time is a fundamental requirement, especially in those applications providing feedback to the patient such as tele-rehabilitation and neuroprosthesis systems. The average time reported in Figure 22 for each SFA highlight that the majority of the fastest SFAs among those tested belong to the complementary filtering class. However, two exceptions were found: GUO, which is a KF explicitly designed by the authors to perform fast, and MCF, which is the MATLAB implementation of VAC, the CF by Valenti *et al.*, 2015 (Valenti et al., 2015). Despite the mathematical formulation is the same, MCF performed 32 times slower than VAC. This could be explained by the fact that the quaternion library used by MATLAB is particularly slow, more specifically the creation of a quaternion object is the limiting factor (results obtained through the MATLAB profiler). The same applies to MKF which was the slowest KF. In general, the higher computation time of Kalman filters can be ascribed to the matrix operations including multiplications and inversions. Finally, it was possible to observe a

monotonic relationship between the dimension of the state vector and the time required by each SFA to perform an update. This is reasonable since an increase in the state vector dimension involves matrices of higher dimensions (e.g., process and measurement covariance matrices, state transition, etc.) with a consequent increase of the computational burden. However, higher speeds could be achieved when using the same SFAs written in different programming languages such as C++.

3.4 A heuristic method to estimate the suboptimal parameter values

3.4.1 The impracticability of the optimal tuning approach

The results obtained in the previous section suggest the possibility of an accurate orientation tracking given a generic SFA, in fact no statistically significant differences were found among the ten tested algorithms provided that its parameter value(s) are properly tuned. The latter, in that case, were set following the optimal tuning approach. However, this requires the knowledge of the ground-truth orientation (for example provided by a SP system) which contrasts with the targeted use of the MIMUs. In fact, an increasing number of applications aim at monitoring the patients in their ecological environment under unconstrained conditions, i.e., out of specialized laboratory for human movement analysis (Mazzà et al., 2021). For the best of the author's knowledge, there are no published solution to estimate the most suitable parameter values without using the orientation reference.

The aim of this section is to propose an alternative strategy to the optimal approach for the selection of reasonable parameter values for a generic SFA. This procedure, called Rigid-Constraint Method (RCM) was designed to suboptimally estimate the parameter values without relying on any reference data. The RCM assumes that two MIMUs have a null relative orientation reference during the entire motion when aligned on the same rigid body. The suboptimal parameter values are identified among the combinations which provide the lowest relative orientation difference. It is hypothesized that the suboptimal values also guarantee for an acceptable absolute orientation error. This can be supported by considering that the disturbance (i.e., body acceleration and ferromagnetic disturbances) and measurement error (e.g., noise, bias fluctuations) characteristics affecting the sensors embedded in the two MIMUs are independent. This will be discussed

more in detail in section 3.4.3 *RCM description*. The validity of the RCM was tested on the same ten algorithms employed for the accuracy comparison under the same experimental conditions. For each experimental scenario and for each SFA, the suboptimal error corresponding to the identified suboptimal parameter values was compared with that obtained under optimal tuning. The RCM was considered successful if the discrepancy amounted to 0.5 deg at most.

3.4.2 Suboptimal working conditions

Compared to the optimal conditions defined in section 3.3.2, suboptimal working conditions refer to the case in which reasonable parameter values for each experimental scenario are identified without relying on any orientation reference. Under appropriate assumptions, *ad hoc* methods are designed to obtain errors close to those obtained under optimal working conditions. In this favorable but realistic situation, the orientation errors of each SFA are in general higher than the minimum achievable, as expected. In this work, the RCM is employed to provide the suboptimal values for each of the 10 SFAs.

3.4.3 RCM description

This paragraph describes the RCM and its underlying assumptions to estimate the most suitable parameter values (i.e., suboptimal) for a given SFA starting from the orientation of two aligned MIMUs and without using the refence data. As anticipated, the RCM aims at finding the combination of parameter values which provide the minimum relative orientation difference since the same combination is also assumed to provide low absolute orientation errors. This assumption can be considered valid in case of difference between the sources of errors which affect the gyroscopes, the accelerometers, and the magnetometers embedded in two different MIMUs. This thesis is discussed for each pair of sensors, separately, referring to the situation illustrated in Figure 29 where two MIMUs are equally orientated on the same rigid body at a relative distance $\boldsymbol{r}$ (i.e., the distance between the origins of the relevant LCSs).

Starting from the gyroscopes, as widely discussed in Chapter 2, the angular velocity readings are affected by both deterministic and stochastic noise. The latter, in particular, represent the main source of errors in the orientation estimation process due to the unpredictability of the bias fluctuations. When considering two different gyroscopes, it is possible to assume without loss of generality that the stochastic sources of errors are uncorrelated being mounted on

different chips, with different sensing elements and different read-out and conditioning circuits (Chang et al., 2008).

For what concerns the accelerometers, they provide a reliable estimate of the inclination only during static (see eq (1) of Chapter 1). During the rigid body movement, the $\boldsymbol{a}_{body}$ term is superimposed to $\boldsymbol{g}$ and their contributions cannot be distinguished. However, if the two accelerometers are separated by a distance $\boldsymbol{r}$ the $\boldsymbol{a}_{body}$ term sensed by each accelerometer is different as expressed by the following equation:

$$\boldsymbol{a_{body2}} = \boldsymbol{a_{body1}} + \dot{\boldsymbol{\omega}} \times \boldsymbol{r} + \boldsymbol{\omega} \times (\boldsymbol{\omega} \times \boldsymbol{r}), \tag{20}$$

where $\boldsymbol{\omega}$ and $\dot{\boldsymbol{\omega}}$ are the body angular velocity and acceleration, respectively. By assuming a perfectly null orientation difference between the LCSs of the two accelerometer and combining the (20) with the accelerometer characteristic equation, it yields to:

$$\boldsymbol{a_2} - \boldsymbol{a_1} = \dot{\boldsymbol{\omega}} \times \boldsymbol{r} + \boldsymbol{\omega} \times (\boldsymbol{\omega} \times \boldsymbol{r}), \tag{21}$$

In practice, this assumption cannot be completely fulfilled due to imperfections in the alignment and the non-orthogonality errors proper of each sensor. However, it is possible to neglect this non-ideality due to its limited magnitude and since it would further enhance the difference between the two accelerometers output thus not preventing the hypothesis on which the RCM is based from holding. It is possible to understand from equation (21) that in case of a roto-translational motion the difference between the two accelerometers output becomes more pronounced as $\boldsymbol{r}$ increases (except when the two LCSs are coincident, which is an impossible condition to meet in practice).

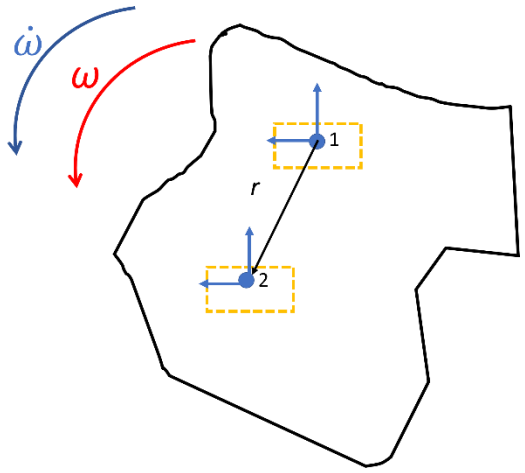

Figure 29: the two accelerometers aligned on a rigid body sense two different acceleration due to their relative distance $\boldsymbol{r}$. Figure taken from (Caruso, Sabatini, Knaflitz, Gazzoni, et al., 2021).

Regarding the magnetometers, in absence of ferromagnetic disturbances, they sense the same Earth's local magnetic field (Figure 30a). However, in a more realistic case of additional magnetic fields superimposed to the Earth's field (in this case referred as $\boldsymbol{h_{1\,ext}}$ and $\boldsymbol{h_{2\,ext}}$), the readings of the two magnetometers can be different depending on their relative position with respect to the source of magnetic disturbance, and this is more likely as $\boldsymbol{r}$ increases as shown in Figure 30b (Genovese & Sabatini, 2006). Assuming that the Earth's magnetic field is equally sensed between the two magnetometers, the difference in their readings can be expressed as follows:

$$\boldsymbol{h}_2 - \boldsymbol{h}_1 = \boldsymbol{h_{2\,ext}} - \boldsymbol{h_{1\,ext}} \propto \boldsymbol{r}. \tag{22}$$

In two cases the difference can be null: 1) in absence of magnetic disturbances (but this would be a favorable situation for the sensor fusion) and 2) when $\boldsymbol{r}$ approaches to zero (i.e., the two LCSs would be coincident and $\boldsymbol{h_{1\,ext}} = \boldsymbol{h_{2\,ext}}$).

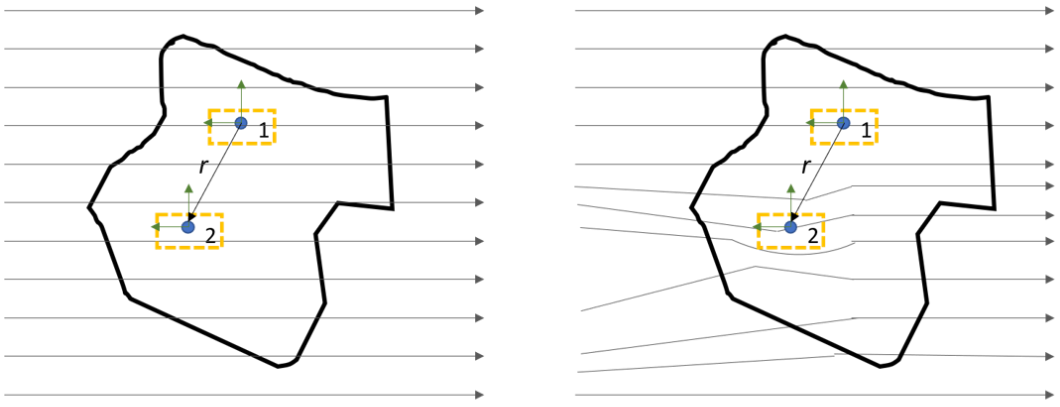

(a) (b)

Figure 30: (a) two magnetometers sense the same local Earth's magnetic field in absence of additional external fields. (b) in presence of disturbances, the two magnetometers sense two different local magnetic fields due to their relative distance $\boldsymbol{r}$. Figure taken from (Caruso, Sabatini, Knaflitz, Gazzoni, et al., 2021).

To sum up, the RCM assumes that the source of errors and disturbances which affect the two MIMUs aligned on the same rigid body can be different during the movement. Whereas this is certainly true for the gyroscopes, the validity of this assumption depends on the experimental conditions in terms of both acceleration magnitude and external magnetic fields. In general, differences between relevant signals are expected to grow as their relative distance $\boldsymbol{r}$ increases. Although this is required by the RCM, from a practical point of view a higher value of $\boldsymbol{r}$ would be unfeasible being the setup too bulky.

3.4.4 Validation session

The validity of the RCM was tested using the same ten SFAs and the same dataset collected and described in section 3.3 *A comparative accuracy analysis under optimal conditions*. For each SFA, for each experimental scenario, and for each combination of the values contained in $\boldsymbol{p_{1vec}}$ and $\boldsymbol{p_{2vec}}$, the relative orientation difference $\Delta\boldsymbol{q_{rel\,A,B}}$ was computed together with $\Delta\boldsymbol{q_{abs\,A}}$ and $\Delta\boldsymbol{q_{abs\,B}}$, as described in (23). The $\Delta\boldsymbol{q_{rel\,A,B}}$ is defined as the relative difference between the LCSs of the two MIMUs.

$$\Delta\boldsymbol{q_{rel\,A,B}} = \boldsymbol{q_A}^* \otimes \boldsymbol{q_B} \tag{23}$$

Then, the scalar part of $\Delta \boldsymbol{q}_{\boldsymbol{rel\ A,B}}$ was converted into the corresponding rotation in degrees to obtain $\delta_{i,j}$. The matrix $\boldsymbol{\delta}$ collecting all the relative orientation errors $\delta_{i,j}$ for each combination for the parameter values was populated following the similar approach adopted to compute the matrix of the optimal errors $\boldsymbol{e}$. This process is summarized in Figure 31.

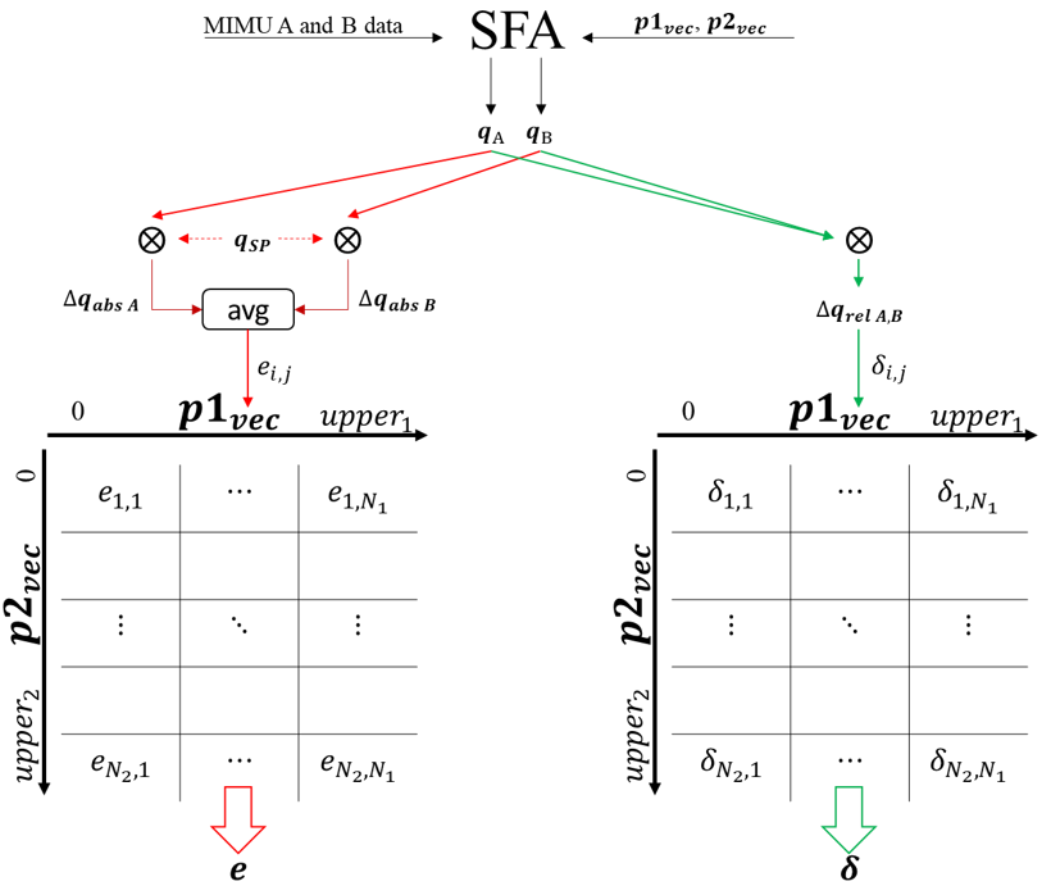

Figure 31: the grid search approach adopted to obtain the absolute orientation error for a given combination of the two parameter values. This process has been applied to each SFA for each of the nine experimental scenarios. avg = average. Figure adapted from (Caruso, Sabatini, Knaflitz, della Croce, et al., 2021).

3.4.5 Data analysis

The analysis was aimed at assessing the effectiveness of the RCM in providing suboptimal parameter values which lead to absolute orientation errors close to the optimal. For this reason, the first step consisted in extracting the suboptimal parameter values from the $\boldsymbol{\delta}$ matrix. The corresponding suboptimal absolute error was then compared with the optimal one. As stated in the introduction, the RCM

was considered successful when this difference, called Δe, was lower than 0.5 deg which is assumed to be the uncertainty band of the SP errors. The Δe was computed for each of the 90 cases (i.e., 10 SFAs × 3 rotation rate magnitudes × 3 commercial devices).

Suboptimal region identification

For each of the 90 cases, the following suboptimal quantities were computed:

- Minimum relative orientation difference: $\delta_{sub} = \min(\boldsymbol{\delta})$.
- The suboptimal region is defined by the values of $\boldsymbol{p_{1vec}}$ and $\boldsymbol{p_{2vec}}$ corresponding to δ_{sub}: $\{\boldsymbol{p_{sub_1}}, \boldsymbol{p_{sub_2}}\} = \{(\boldsymbol{p_{1vec}}, \boldsymbol{p_{2vec}}) \mid \boldsymbol{\delta} = \delta_{sub}\}$. When the region, $\{\boldsymbol{p_{sub_1}}, \boldsymbol{p_{sub_2}}\}$ was formed by two or more separated sub-regions, only the largest was considered.
- The suboptimal parameter values (p_{1c} and p_{2c}) are the values of $\boldsymbol{p_{1vec}}$ and $\boldsymbol{p_{2vec}}$ corresponding to the centroid of the suboptimal region: $\{p_{1c}, p_{2c}\} = \text{centroid}(\boldsymbol{p_{sub_1}}, \boldsymbol{p_{sub_2}})$.
- The suboptimal absolute orientation error is the absolute orientation error corresponding to p_{1c} and p_{2c}: $e_{sub} = \boldsymbol{e}(p_{1c}, p_{2c})$.

Metric to validate the RCM

For each of the 90 cases, the residual between the optimal and suboptimal error was computed as follows:

$$\Delta e = e_{sub} - e_{opt} \tag{24}$$

The 90 values of Δe were collected and then analyzed by means of the boxplot representation.

3.4.6 Results

Suboptimal errors and residuals

The suboptimal orientation error (e_{sub}) and the residual (Δe) are reported in Table XIII for each of the 90 cases under consideration. The bold notation is used for Δe exceeding 0.5 deg. The boxplot distribution of the 90 values of Δe is represented in Figure 32.

Table XIII: the suboptimal and the residual values obtained for each SFA and for each experimental scenario. Table adapted from (Caruso, Sabatini, Knaflitz, della Croce, et al., 2021). The bold notation is used for Δe exceeding 0.5 deg.

		CF	e_{sub}	Δe	KF	e_{sub}	Δe
Xsens	Slow	MAH	2.5	0	SAB	2.2	0
	Medium		3.8	**1.4**		2.1	0
	Fast		4.2	0.2		2.4	0
APDM	Slow		5.6	**1.8**		5.1	0.1
	Medium		4.9	0.1		5.8	0.1
	Fast		9.2	**1**		10.0	**1.7**
Shimmer	Slow		3.7	0.3		4.5	0
	Medium		5.3	0.7		4.9	0
	Fast		10.6	**3**		9.6	**1.1**
Xsens	Slow	MAD	2.7	0	LIG	2.4	0.5
	Medium		4.0	**1.5**		3.8	**1.8**
	Fast		4.0	0		3.4	0.5
APDM	Slow		3.8	0		3.9	0.3
	Medium		4.8	0.2		5.1	0.2
	Fast		8.2	0.1		4.9	0.3
Shimmer	Slow		4.1	0.2		4.6	0.2
	Medium		5.1	0.2		4.2	0.2
	Fast		10.8	**2**		6.5	0.2
Xsens	Slow	VAC	4.0	0	VAK	1.5	0.3
	Medium		5.1	0.1		1.7	0.1
	Fast		7.2	0		2.5	0
APDM	Slow		4.4	**0.9**		4.1	0.5
	Medium		6.4	0.3		6.9	**0.9**
	Fast		11.3	**3**		10.4	**1.2**
Shimmer	Slow		3.8	0		4.6	**0.6**
	Medium		10.8	**0.6**		5.7	**1.3**

	Fast		15.2	**3.7**		10.6	**2.4**
Xsens	Slow		3.5	0.4		2.3	0
	Medium		3.9	**1.4**		2.3	0
	Fast		5.1	0		5.7	0
APDM	Slow	SEL	3.8	0.1	GUO	4.5	0.3
	Medium		7.1	0		5.7	**0.6**
	Fast		10.0	**2**		9.4	0
Shimmer	Slow		3.5	0.1		4.2	0.2
	Medium		6.3	**1.3**		5.1	0
	Fast		10.8	**1.4**		14.4	**0.7**
Xsens	Slow		3.4	0.1		4.3	0.1
	Medium		6.1	0		4.8	0
	Fast		7.5	**0.9**		6.9	0.2
APDM	Slow	MCF	4.8	**1**	MKF	3.8	0.2
	Medium		12.5	0.2		5.3	0
	Fast		9.6	**1.7**		7.2	0
Shimmer	Slow		5.2	0.2		4.2	0.3
	Medium		13.3	**3.3**		9.8	**1.4**
	Fast		8.8	0.2		10.0	0.1

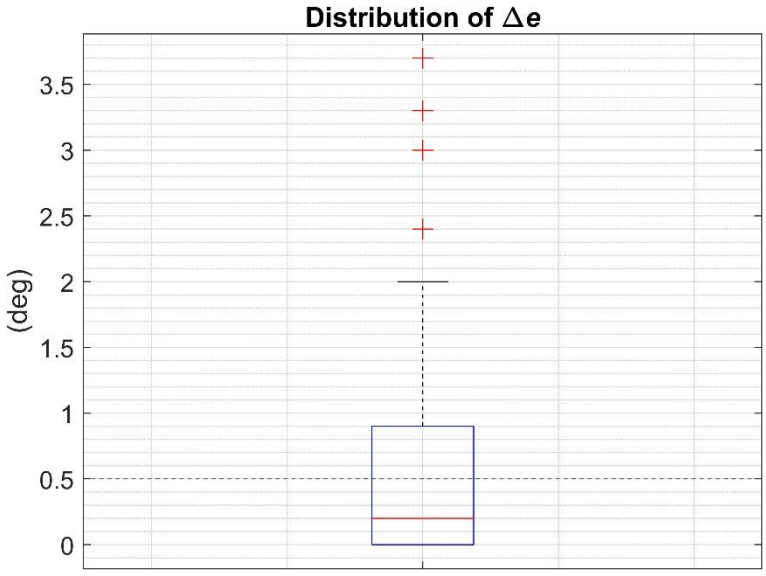

Figure 32: the boxplot distribution of the 90 Δe values. The dashed horizontal line at 0.5 deg is to highlight the threshold to consider the suboptimal errors equivalent to the optimal error.

Suboptimal regions

For each SFA, the suboptimal regions corresponding to the nine experimental scenarios are reported in the right column of the Appendix at the end of this chapter (next to the corresponding optimal regions reported on the left column). Moreover, for each suboptimal region, the centroid is also indicated with a circular marker. Figure 33 provides an example of comparison between the optimal and suboptimal regions for each experimental scenario (highlighted with different colors) when considering the LIG filter.

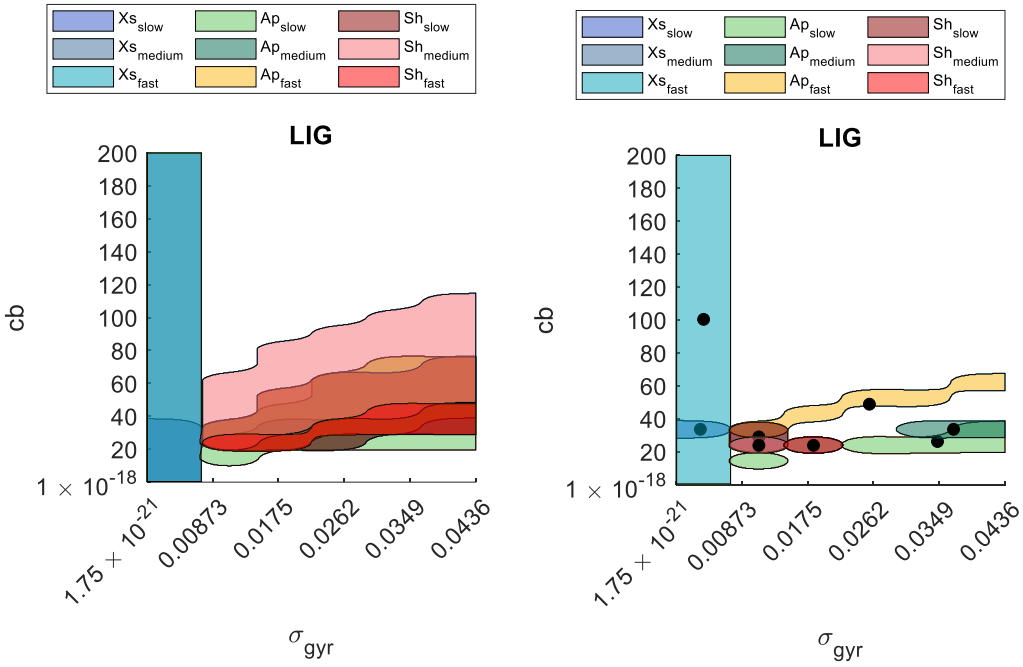

Figure 33: an example of comparison between the optimal (on the left) and suboptimal (on the right) regions for the LIG filter for each experimental scenario. Each scenario is represented using a different color.

3.4.7 Discussion

The “rigid-constraint” method was proposed to estimate suitable parameter values for the sensor fusion filters without relying on any ground-truth orientation to reflect a more common situation during the everyday use of the MIMUs. The RCM assumes that the combination of the parameter values which minimizes the relative orientation difference, is also a suboptimal choice to obtain limited orientation errors under the same specific experimental conditions. Results listed

in Table XIII showed that $\Delta\boldsymbol{e}$ were lower or equal to 0.5 deg in the 67% of the cases (60 out of 90). In the remaining 33%, residuals were between 0.5 and 1.0 deg in 10 cases, and higher than 1.0 deg in 20 cases. These results suggest the possibility to properly tune a generic SFA on different scenarios without using any orientation reference. In these 30 cases, the maximum value of $\Delta\boldsymbol{e}$ amounted to 3.7 deg, while the median and the mean values of the residual distribution amounted to 0.2 deg and 0.6 deg, respectively. As expected, the performance of the RCM worsened when the rotation rate magnitude increased. More in detail, only 4 out of 30 cases were at slow speed while 14/30 were observed at fast rotation rate. This confirmed the finding of previous studies which recognized the unfavorable effect of the rotation rate for the orientation estimation accuracy (Lebel et al., 2013, 2015; Ricci et al., 2016). As observed for the comparison under optimal conditions, also the hardware included in the different commercial devices had an influence on the accuracy of the RCM. In fact, in the 30 cases in which Δe was higher than 0.5 deg, only 5 were attributed to Xsens, while 14 to Shimmer. Furthermore, the RCM had a different effectiveness based on the specific SFA to which it was applied. In particular, for LIG only 1/9 residual was higher than 0.5 deg while VAK and MAK with the highest number of residuals (5/9). Overall, the maximum residual value was limited to 3.7 deg and it was obtained at fast rotation rate with Shimmer.

As already mentioned, some limitations must be considered when employing the RCM. In fact, when $\boldsymbol{r}$ approaches zero the assumption that the sources of noise affecting accelerometers and magnetometers are different is no longer valid. In fact, the differences in the accelerometer and magnetometer signals tend to be less evident regardless of the body accelerations (21) and ferromagnetic disturbances (22). In this situation, the relative orientation difference may be very small due to the similarity of the measurements, but it does not guarantee low absolute errors, especially if the orientations of the two MIMUs are estimated giving a high weight to the accelerometer and magnetometer readings. From a practical point of view, the authors suggest placing the two MIMUs so that $\boldsymbol{r}$ amounts to at least a few centimeters, compatibly with the size of the rigid body support. Additional investigations should be carried out to find the optimal trade-off between a value of $\boldsymbol{r}$ high enough to guarantee an adequate difference between the relevant signals and the necessity to contain the setup dimensions.

The RCM can be applied in different scenarios in which the MIMUs can be firmly attached to the body segment of interest by means of mounted rigid plastic

plates using elastic straps. An example can be found in (Bertuletti et al., 2017), where a support was designed to be attached to the foot. Alternatively, if only one MIMU is necessary for the data collection, then it would be reasonable to use the plastic case hosting both the MIMU to be employed and an additional MIMU to define the suboptimal parameter(s) values of the selected SFA on preliminary movement data acquisition which reflects the actual experimental scenarios (i.e., similar MIMU model, motor task, rotation rate magnitude, etc.). A similar approach was followed by Cardarelli *et al*., in (Cardarelli et al., 2019) where the orientation of a MIMU mounted on the lower back was estimated to remove the gravity vector from the accelerometer readings before the double-integration to obtain the displacement. Since this operation is prone to huge drifts, the authors were successful in minimizing this effect by using a weighted Fourier linear combiner whose parameters were tuned on a preliminary acquisition by replicating the same motion conditions.

References

Bergamini, E., Ligorio, G., Summa, A., Vannozzi, G., Cappozzo, A., & Sabatini, A. M. (2014). Estimating orientation using magnetic and inertial sensors and different sensor fusion approaches: Accuracy assessment in manual and locomotion tasks. *Sensors (Switzerland)*, *14*(10), 18625–18649. https://doi.org/10.3390/s141018625

Bertuletti, S., Cereatti, A., Comotti, D., Caldara, M., & Della Croce, U. (2017). Static and dynamic accuracy of an innovative miniaturized wearable platform for short range distance measurements for human movement applications. *Sensors (Switzerland)*, *17*(7), 1–15. https://doi.org/10.3390/s17071492

Cappozzo, A., Cappello, A., Croce, U. della, & Pensalfini, F. (1997). *Surface-Marker Cluster Design Criteria for 3-D Bone Movement Reconstruction*. *44*(12), 1165–1174.

Cardarelli, S., Verdini, F., Mengarelli, A., Strazza, A., Di Nardo, F., Burattini, L., & Fioretti, S. (2019). Position Estimation of an IMU Placed on Pelvis Through Meta-heuristically Optimised WFLC. In L. Lhotska, L. Sukupova, I. Lacković, & G. S. Ibbott (Eds.), *World Congress on Medical Physics and Biomedical Engineering 2018* (pp. 659–664). Springer Singapore.

Caruso, M., Sabatini, A. M., Knaflitz, M., della Croce, U., & Cereatti, A. (2021). Extension of the Rigid-Constraint Method for the Heuristic Suboptimal Parameter Tuning to Ten Sensor Fusion Algorithms Using Inertial and Magnetic Sensing. *Sensors*, *21*(18), 6307. https://doi.org/10.3390/s21186307

Caruso, M., Sabatini, A. M., Knaflitz, M., Gazzoni, M., Croce, U. della, & Cereatti, A. (2019). Accuracy of the Orientation Estimate Obtained Using Four Sensor Fusion Filters Applied to Recordings of Magneto-Inertial Sensors Moving at Three Rotation Rates. *Proceedings of the Annual International Conference of the IEEE Engineering in Medicine and Biology Society, EMBS*, 2053–2058. https://doi.org/10.1109/EMBC.2019.8857655

Caruso, M., Sabatini, A. M., Knaflitz, M., Gazzoni, M., Croce, U. della, & Cereatti, A. (2021). Orientation Estimation through Magneto-Inertial Sensor Fusion: A Heuristic Approach for Suboptimal Parameters Tuning. *IEEE Sensors Journal*, *21*(3), 3408–3419. https://doi.org/10.1109/JSEN.2020.3024806

Caruso, M., Sabatini, A. M., Laidig, D., Seel, T., Knaflitz, M., della Croce, U., & Cereatti, A. (2021). Analysis of the Accuracy of Ten Algorithms for Orientation Estimation Using Inertial and Magnetic Sensing under Optimal Conditions: One Size Does Not Fit All. *Sensors*, *21*(7), 2543. https://doi.org/10.3390/s21072543

Cavallo, A., Cirillo, A., Cirillo, P., Maria, G. de, Falco, P., Natale, C., & Pirozzi, S. (2014). Experimental Comparison of Sensor Fusion Algorithms for Attitude Estimation. In *IFAC Proceedings Volumes* (Vol. 47, Issue 3). IFAC. https://doi.org/10.3182/20140824-6-ZA-1003.01173

Chang, H., Xue, L., Qin, W., Yuan, G., & Yuan, W. (2008). An Integrated MEMS Gyroscope Array with Higher Accuracy Output. *Sensors*, *8*(4), 2886–2899. https://doi.org/10.3390/s8042886

Chardonnens, J., Favre, J., & Aminian, K. (2012). An effortless procedure to align the local frame of an inertial measurement unit to the local frame of another motion capture system. *Journal of Biomechanics*, *45*(13), 2297–2300. https://doi.org/10.1016/j.jbiomech.2012.06.009

Chiari, L., della Croce, U., Leardini, A., & Cappozzo, A. (2005). Human movement analysis using stereophotogrammetry. Part 2: Instrumental errors. *Gait and Posture*, *21*(2), 197–211. https://doi.org/10.1016/j.gaitpost.2004.04.004

Fan, B., Li, Q., & Liu, T. (2018). Improving the accuracy of wearable sensor orientation using a two-step complementary filter with state machine-based adaptive strategy. *Measurement Science and Technology*, *29*(11). https://doi.org/10.1088/1361-6501/aae125

Genovese, V., & Sabatini, A. M. (2006). Differential Compassing Helps Human-Robot Teams Navigate in Magnetically Disturbed Environments. *IEEE Sensors Journal*, *6*(5), 1045–1046. https://doi.org/10.1109/JSEN.2006.881417

Guo, S., Wu, J., Wang, Z., & Qian, J. (2017). Novel MARG-Sensor Orientation Estimation Algorithm Using Fast Kalman Filter. *Journal of Sensors*, *2017*. https://doi.org/10.1155/2017/8542153

Laidig, D., Caruso, M., Cereatti, A., & Seel, T. (2021). BROAD—A Benchmark for Robust Inertial Orientation Estimation. *Data*, *6*(7). https://doi.org/10.3390/data6070072

Lebel, K., Boissy, P., Hamel, M., & Duval, C. (2013). Inertial measures of motion for clinical biomechanics: Comparative assessment of accuracy under controlled conditions - Effect of velocity. *PLoS ONE*, *8*(11). https://doi.org/10.1371/journal.pone.0079945

Lebel, K., Boissy, P., Hamel, M., & Duval, C. (2015). Inertial measures of motion for clinical biomechanics: Comparative assessment of accuracy under controlled conditions - Changes in accuracy over time. *PLoS ONE*, *10*(3). https://doi.org/10.1371/journal.pone.0118361

Lee, S., & Lee, D. K. (2018). What is the proper way to apply the multiple comparison test? *Korean Journal of Anesthesiology*, *71*(5), 353–360. https://doi.org/10.4097/kja.d.18.00242

Ligorio, G., & Sabatini, A. M. (2015). A novel kalman filter for human motion tracking with an inertial-based dynamic inclinometer. *IEEE Transactions on Biomedical Engineering*, *62*(8), 2033–2043. https://doi.org/10.1109/TBME.2015.2411431

Ludwig, S. A., & Burnham, K. D. (2018). Comparison of Euler Estimate using Extended Kalman Filter, Madgwick and Mahony on Quadcopter Flight Data. *2018 International Conference on Unmanned Aircraft Systems, ICUAS 2018*, 1236–1241. https://doi.org/10.1109/ICUAS.2018.8453465

Luinge, H. J., & Veltink, P. H. (2004). Inclination Measurement of Human Movement Using a 3-D Accelerometer with Autocalibration. *IEEE Transactions on Neural Systems and Rehabilitation Engineering*, *12*(1), 112–121. https://doi.org/10.1109/TNSRE.2003.822759

Madgwick, S. O. H., Harrison, A. J. L., & Vaidyanathan, R. (2011). Estimation of IMU and MARG orientation using a gradient descent algorithm. *IEEE International Conference on Rehabilitation Robotics*, *2011*. https://doi.org/10.1109/ICORR.2011.5975346

Mahony, R., Hamel, T., & Pflimlin, J. M. (2008). Nonlinear complementary filters on the special orthogonal group. *IEEE Transactions on Automatic Control*, *53*(5), 1203–1218. https://doi.org/10.1109/TAC.2008.923738

Mazzà, C., Alcock, L., Aminian, K., Becker, C., Bertuletti, S., Bonci, T., Brown, P., Brozgol, M., Buckley, E., Carsin, A.-E., Caruso, M., Caulfield, B., Cereatti, A., Chiari, L., Chynkiamis, N., Ciravegna, F., del Din, S., Eskofier, B., Evers, J., … Rochester, L. (2021). Technical validation of real-world monitoring of gait: a multicentric observational study. *BMJ Open*, *11*(12), e050785. https://doi.org/10.1136/bmjopen-2021-050785

Nazarahari, M., & Rouhani, H. (2020). 40 Years of Sensor Fusion for Orientation Tracking via Magnetic and Inertial Measurement Units: Methods, Lessons Learned, and Future Challenges. *Information Fusion*, *68*(September 2020), 67–84. https://doi.org/10.1016/j.inffus.2020.10.018

Nez, A., Fradet, L., Monnet, T., & Lacouture, P. (2017). Movement analysis with inertial sensors: identification of noise covariance matrices to improve body segment orientation using Kalman filtering. *Https://Doi.Org/10.1080/10255842.2017.1382906*, *20*(s1), 151–152. https://doi.org/10.1080/10255842.2017.1382906

Olivares, A., Górriz, J. M., Ramírez, J., & Olivares, G. (2016). Using frequency analysis to improve the precision of human body posture algorithms based on Kalman filters. *Computers in Biology and Medicine*, *72*, 229–238. https://doi.org/10.1016/j.compbiomed.2015.08.007

Ricci, L., Taffoni, F., & Formica, D. (2016). On the orientation error of IMU: Investigating static and dynamic accuracy targeting human motion. *PLoS ONE*, *11*(9), e0161940. https://doi.org/10.1371/journal.pone.0161940

Roetenberg, D., Baten, C. T. M. M., & Veltink, P. H. (2007). Estimating body segment orientation by applying inertial and magnetic sensing near ferromagnetic materials. *IEEE Transactions on Neural Systems and Rehabilitation Engineering*, *15*(3), 469–471. https://doi.org/10.1109/TNSRE.2007.903946

Sabatini, A. M. (2011). Estimating three-dimensional orientation of human body parts by inertial/magnetic sensing. *Sensors*, *11*(2), 1489–1525. https://doi.org/10.3390/s110201489

Seel, T., & Ruppin, S. (2017). Eliminating the Effect of Magnetic Disturbances on the Inclination Estimates of Inertial Sensors. *IFAC-PapersOnLine*, *50*(1), 8798–8803. https://doi.org/10.1016/j.ifacol.2017.08.1534

Valenti, R. G., Dryanovski, I., & Xiao, J. (2015). Keeping a good attitude: A quaternion-based orientation filter for IMUs and MARGs. *Sensors (Switzerland)*, *15*(8), 19302–19330. https://doi.org/10.3390/s150819302

Valenti, R. G., Dryanovski, I., & Xiao, J. (2016). A linear Kalman filter for MARG orientation estimation using the algebraic quaternion algorithm. *IEEE Transactions on Instrumentation and Measurement*, *65*(2), 467–481. https://doi.org/10.1109/TIM.2015.2498998

Weber, D., Gühmann, C., & Seel, T. (2020). *Neural Networks Versus Conventional Filters for Inertial-Sensor-based Attitude Estimation*. http://arxiv.org/abs/2005.06897

Young, A. D. (2009). Comparison of orientation filter algorithms for realtime wireless inertial posture tracking. *Proceedings - 2009 6th International Workshop on Wearable and Implantable Body Sensor Networks, BSN 2009*, 59–64. https://doi.org/10.1109/BSN.2009.25

Appendix (Chapter 3)

Optimal Regions (Intervals)

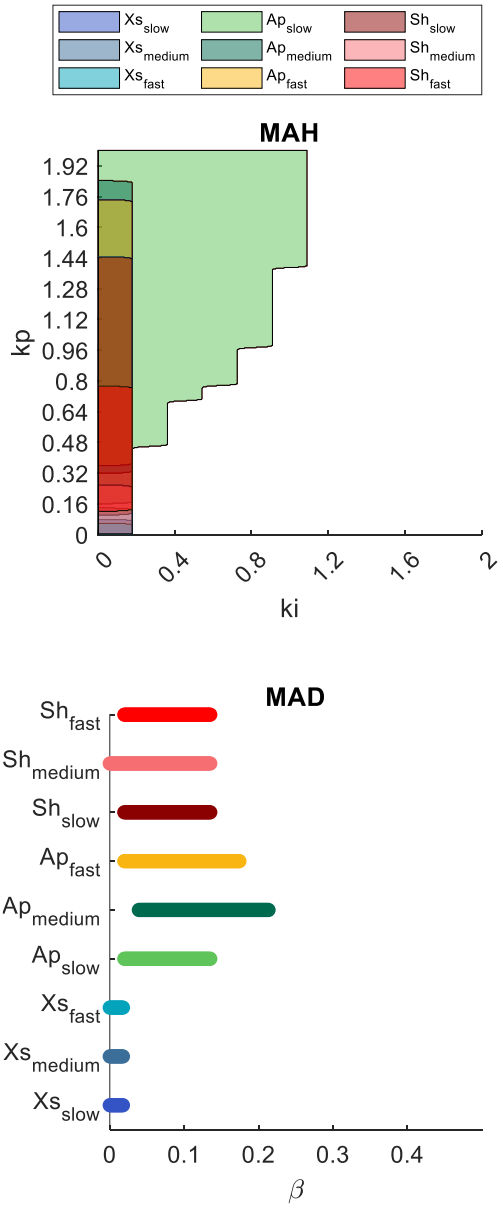

Suboptimal Regions (Intervals)

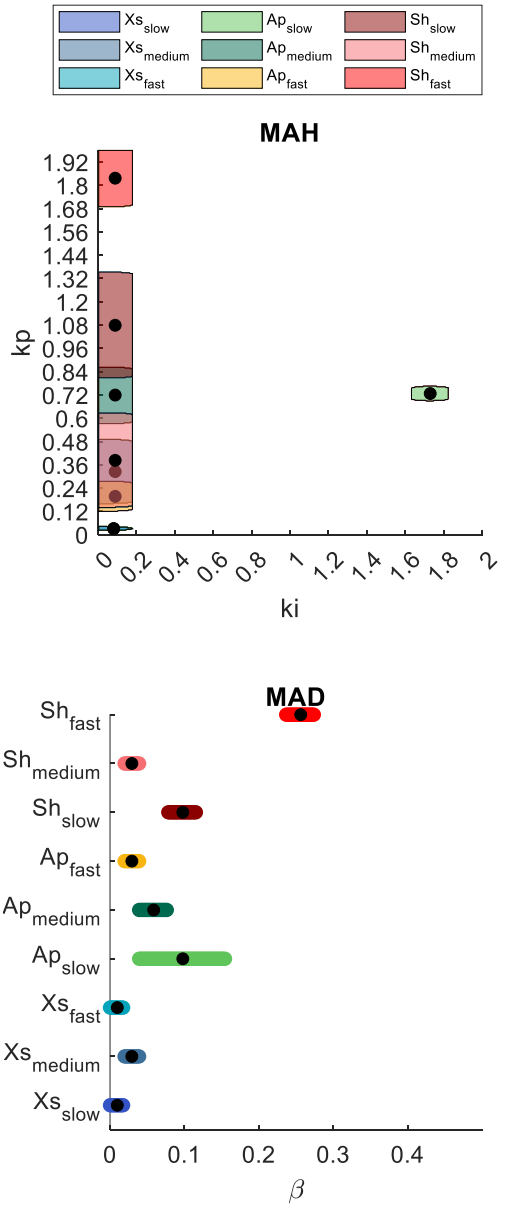

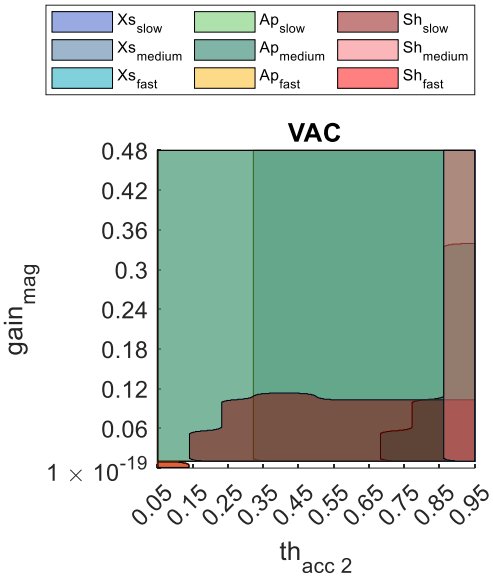
Xs slow
Ap slow
Sh slow
Xs medium
Ap medium
Sh medium
Xs fast
Ap fast
Sh fast
VAC
gain mag
0.48
0.42
0.36
0.3
0.24
0.18
0.12
0.06
1 × 10-19
0.05 0.15 0.25 0.35 0.45 0.55 0.65 0.75 0.85 0.95
th acc 2

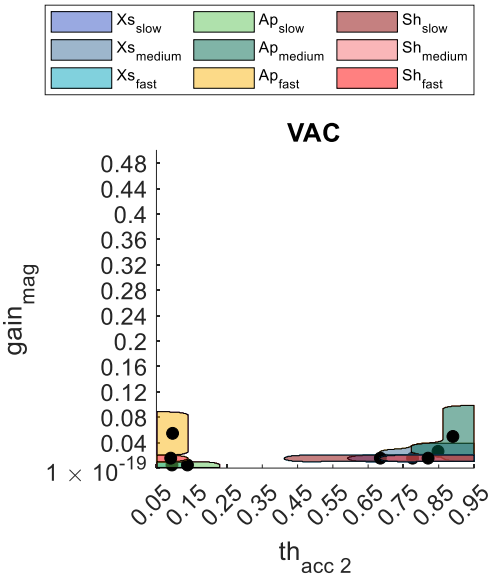
Xs slow
Ap slow
Sh slow
Xs medium
Ap medium
Sh medium
Xs fast
Ap fast
Sh fast
VAC
gain mag
0.48
0.44
0.4
0.36
0.32
0.28
0.24
0.2
0.16
0.12
0.08
0.04
1 × 10-19
0.05 0.15 0.25 0.35 0.45 0.55 0.65 0.75 0.85 0.95
th acc 2

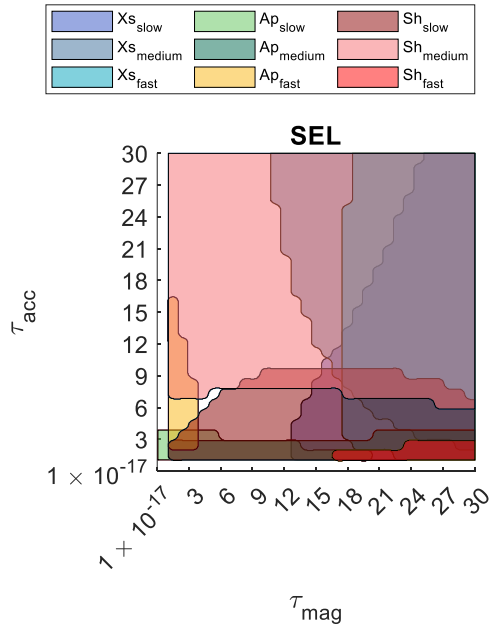
Xs slow
Ap slow
Sh slow
Xs medium
Ap medium
Sh medium
Xs fast
Ap fast
Sh fast
SEL
τacc
30
27
24
21
18
15
12
9
6
3
1 × 10-17
1 + 10-17 3 6 9 12 15 18 21 24 27 30
τmag

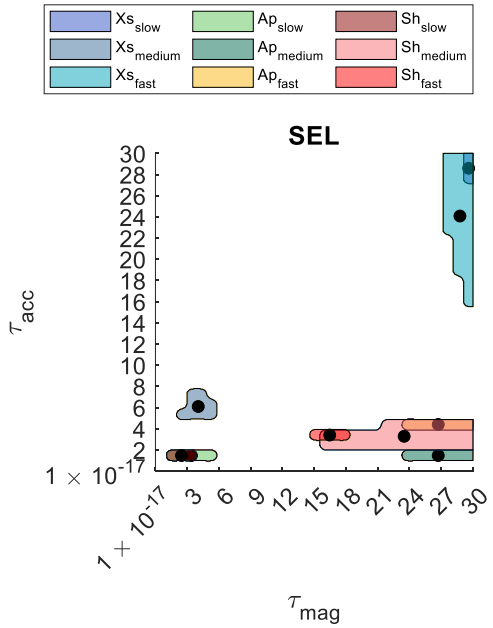
Xs slow
Ap slow
Sh slow
Xs medium
Ap medium
Sh medium
Xs fast
Ap fast
Sh fast
SEL
τacc
30
28
26
24
22
20
18
16
14
12
10
8
6
4
2
1 × 10-17
1 + 10-17 3 6 9 12 15 18 21 24 27 30
τmag

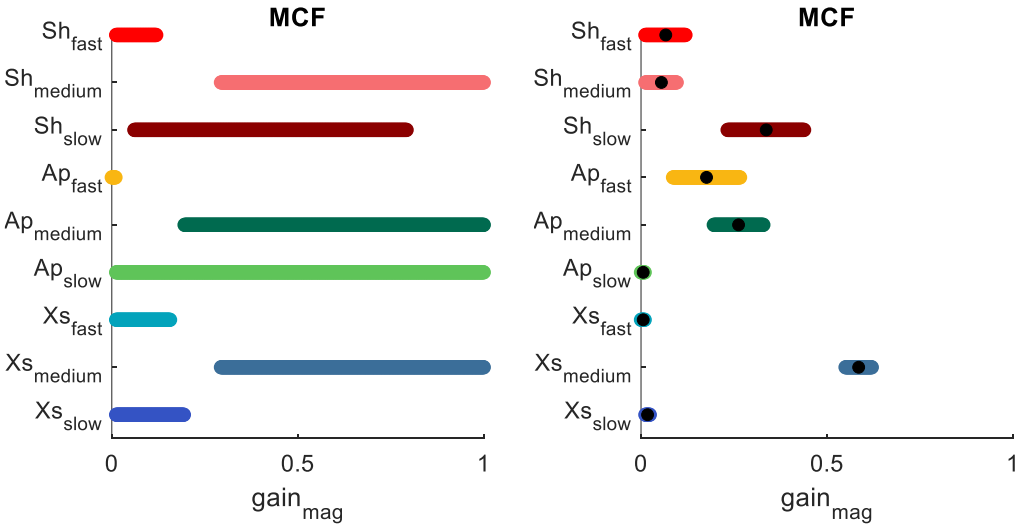
MCF
Sh fast
Sh medium
Sh slow
Ap fast
Ap medium
Ap slow
Xs fast
Xs medium
Xs slow
0
0.5
1
gain mag
MCF
Sh fast
Sh medium
Sh slow
Ap fast
Ap medium
Ap slow
Xs fast
Xs medium
Xs slow
0
0.5
1
gain mag

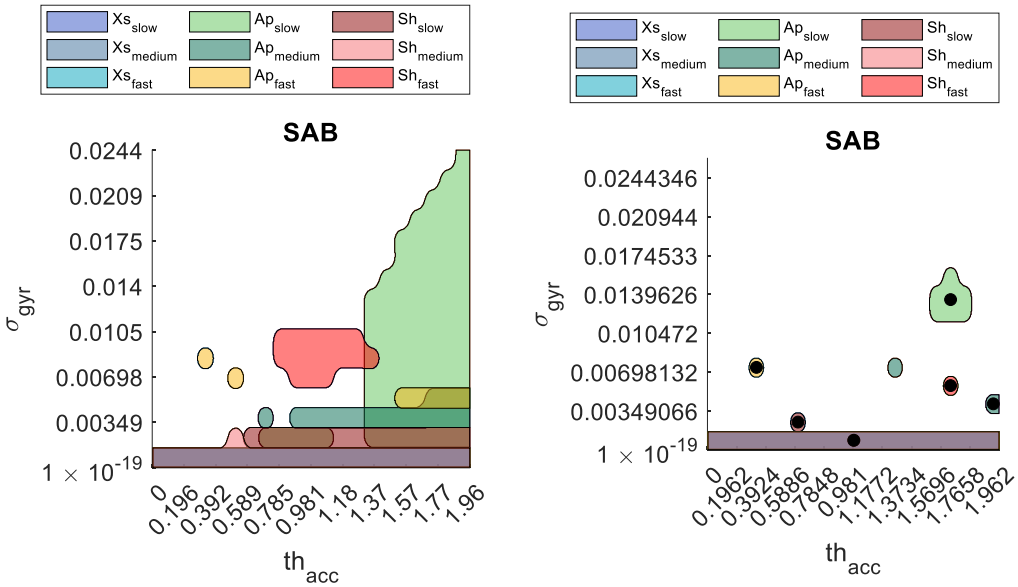
Xs slow
Ap slow
Sh slow
Xs medium
Ap medium
Sh medium
Xs fast
Ap fast
Sh fast
SAB
0.0244
0.0209
0.0175
0.014
0.0105
0.00698
0.00349
1 × 10-19
σ gyr
0
0.196
0.392
0.589
0.785
0.981
1.18
1.37
1.57
1.77
1.96
th acc
Xs slow
Ap slow
Sh slow
Xs medium
Ap medium
Sh medium
Xs fast
Ap fast
Sh fast
SAB
0.0244346
0.020944
0.0174533
0.0139626
0.010472
0.00698132
0.00349066
1 × 10-19
σ gyr
0
0.1962
0.3924
0.5886
0.7848
0.981
1.1772
1.3734
1.5696
1.7658
1.962
th acc

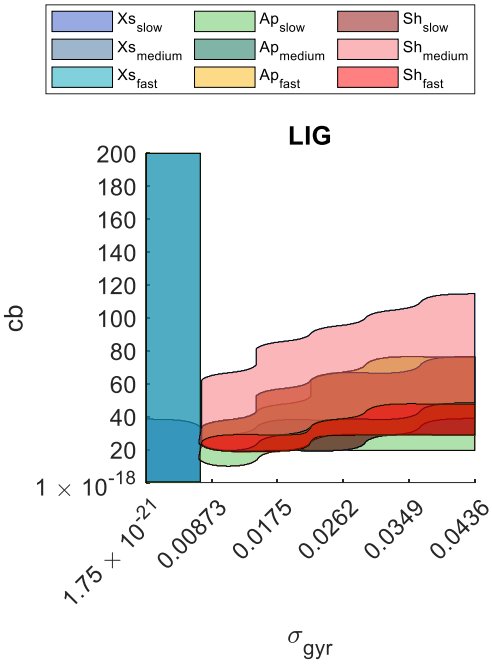
Xs slow
Xs medium
Xs fast
Ap slow
Ap medium
Ap fast
Sh slow
Sh medium
Sh fast
LIG
cb
200
180
160
140
120
100
80
60
40
20
1 × 10-18
1.75 + 10-21
0.00873
0.0175
0.0262
0.0349
0.0436
σgyr

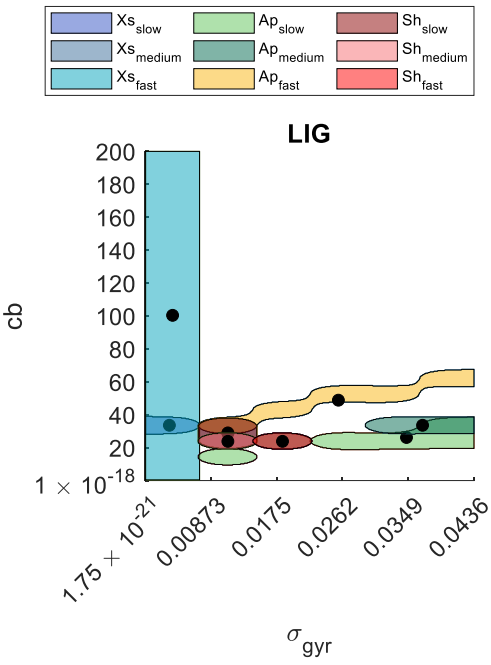
Xs slow
Xs medium
Xs fast
Ap slow
Ap medium
Ap fast
Sh slow
Sh medium
Sh fast
LIG
cb
200
180
160
140
120
100
80
60
40
20
1 × 10-18
1.75 + 10-21
0.00873
0.0175
0.0262
0.0349
0.0436
σgyr

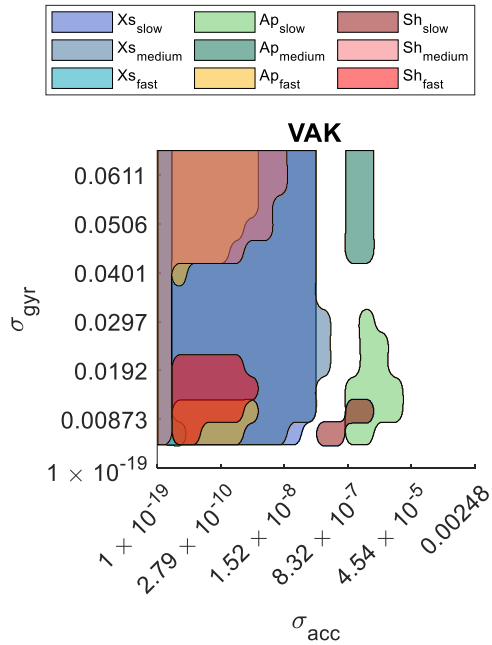
Xs slow
Xs medium
Xs fast
Ap slow
Ap medium
Ap fast
Sh slow
Sh medium
Sh fast
VAK
σgyr
0.0611
0.0506
0.0401
0.0297
0.0192
0.00873
1 × 10-19
1 + 10-19
2.79 + 10-10
1.52 + 10-8
8.32 + 10-7
4.54 + 10-5
0.00248
σacc

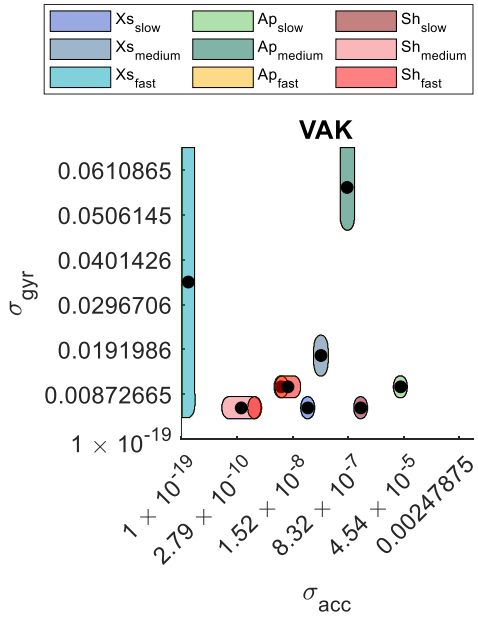
Xs slow
Xs medium
Xs fast
Ap slow
Ap medium
Ap fast
Sh slow
Sh medium
Sh fast
VAK
σgyr
0.0610865
0.0506145
0.0401426
0.0296706
0.0191986
0.00872665
1 × 10-19
1 + 10-19
2.79 + 10-10
1.52 + 10-8
8.32 + 10-7
4.54 + 10-5
0.00247875
σacc

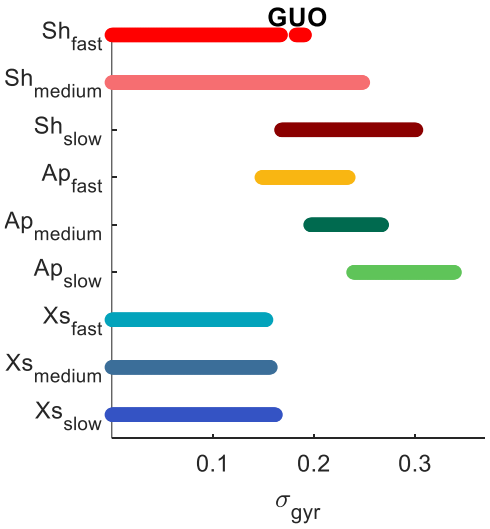
GUO
Sh fast
Sh medium
Sh slow
Ap fast
Ap medium
Ap slow
Xs fast
Xs medium
Xs slow
0.1
0.2
0.3
σ gyr

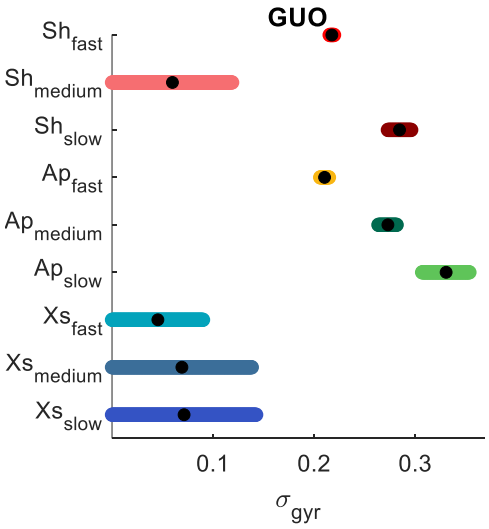
GUO
Sh fast
Sh medium
Sh slow
Ap fast
Ap medium
Ap slow
Xs fast
Xs medium
Xs slow
0.1
0.2
0.3
σ gyr

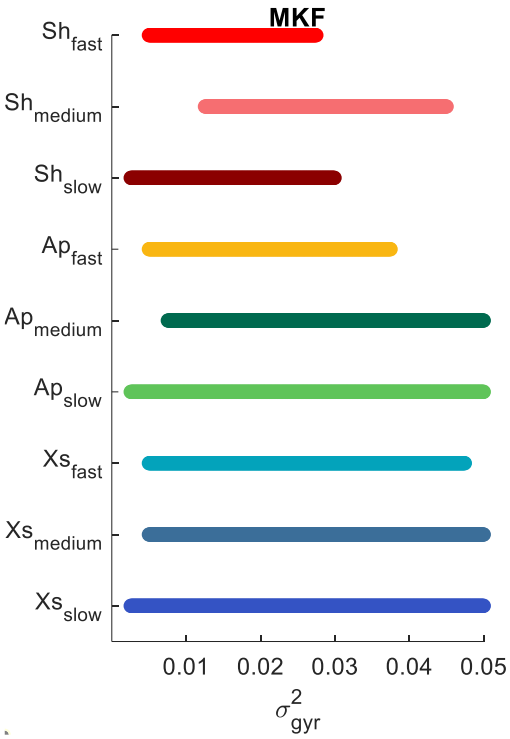
MKF
Sh fast
Sh medium
Sh slow
Ap fast
Ap medium
Ap slow
Xs fast
Xs medium
Xs slow
0.01
0.02
0.03
0.04
0.05
σ² gyr

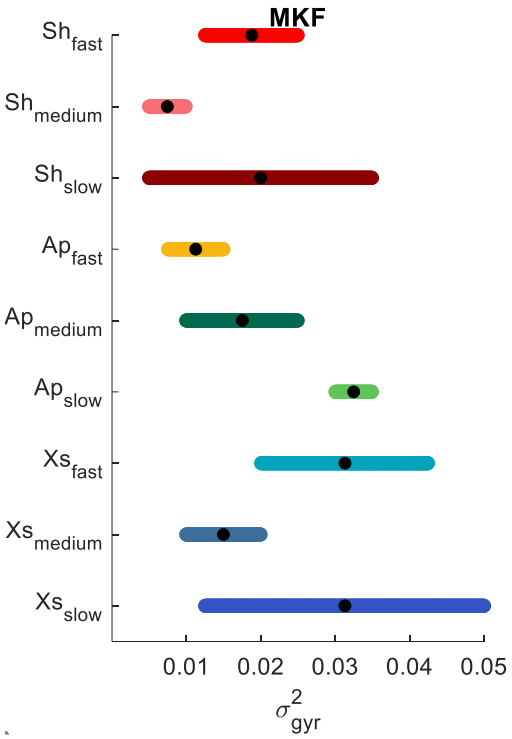
MKF
Sh fast
Sh medium
Sh slow
Ap fast
Ap medium
Ap slow
Xs fast
Xs medium
Xs slow
0.01
0.02
0.03
0.04
0.05
σ² gyr

Chapter 4

Joint kinematics estimation

4.1 Introduction

The estimation of the three-dimensional orientation of the MIMUs has enabled the tracking of the human joint kinematics using wearable sensors (Bonato, 2003; Seel et al., 2014). The accurate knowledge of the joint angles is required in several applications such as sport, ergonomics, clinical evaluation, and telerehabilitation (Bouvier et al., 2015). Each human joint can be seen as the connection between two adjacent body segments whose relative motion is characterized by a certain number of degrees of freedom (DoFs) depending on the joint under analysis. For example, the knee can be modelled as a hinge-joint with one DoF, the ankle, the wrist, and the elbow as a universal joint with two DoFs, while the shoulder and the hip as spherical joints with three DoFs. For a rigorous description, the model of the human joints should also take into account the three linear displacements due to the joint physiological laxity in all the directions, thus resulting in three additional DoFs (Roetenberg et al., 2009). However, the magnitude of these quantities is too small to be accurately detected and it will be neglected in this thesis (Cereatti et al., 2015).

The computation of the human joint kinematics requires the orientation of the two MIMUs attached to the proximal and distal segments of the considered joint to be known. In general, the LCS of a MIMU is not aligned with the anatomical coordinate system (ACS) of the corresponding segments which is defined by the guidelines of the International Society of Biomechanics (ISB), (Wu et al., 2002,

2005). Different solutions have been developed over the years to estimate the time-invariant relative orientation between the LCS of each MIMU and the relevant ACS, as discussed in the dedicated paragraph. After this realignment, the joint kinematics is defined as the distal-to-proximal relative orientation at each time step (Cereatti et al., 2017). The joint angles are finally obtained by means of the Euler decomposition following the sequence suggested by the ISB. In this context, it is clear that the accurate estimate of the MIMU orientation is crucial to obtain reliable values of the joint angles. Sensor errors such as the gyroscope bias and the disturbances affecting the sensor fusion process, e.g., linear acceleration and ferromagnetic interference, are directly reflected on the final angle estimates. This kind of approach is called unconstrained since it does not consider any additional information to mitigate the effects of an inaccurate orientation error estimates on the joint angles. However, the unconstrained joint kinematics offers the advantages to be computationally fast and accurate under particular experimental conditions such as short-time duration and absence of vigorous movements. The telerehabilitation project called DoMoMEA (Pani & Cereatti, n.d.; Zedda et al., 2020) is based on the joint angles obtained this way to provide and monitor the rehabilitation progress of survivors who had suffered from stroke. Briefly, the patients are asked to perform a battery of exercises at their home involving the main human joints. The angle time-series is used to animate the exergame (a videogame aimed at performing a physical exercise) and to compute quantitative parameters including the range of motion (ROM) and the time of execution.

In this first part of this chapter, the DoMoMEA project will be described with a specific focus to the procedures implemented to compute the joint angles without considering the magnetometer in the sensor fusion due to the unforeseeable disturbances, very likely in a domestic environment. Then, the validation protocol designed to evaluate the angular accuracy of both the joint angle time series and the ROM together with the main results and limitations will be discussed.

The second part of this chapter deals with the constrained kinematics estimation. In fact, although the DoMoMEA approach is simple and easy to be executed by the patients at their home without supervision, the inherent issues related to orientation drift and cannot be solved this way but only mitigated using precautions, e.g., by limiting the total amount of time of each exercise and by removing the gyroscope offset prior to each experimental session. For this reason, a biomechanical model of the human upper limb drew on the robotics is proposed

to increase the robustness of the quantities estimated starting from the MIMU measurements through the definition of physiological constraints. The analysis of the upper limb motion represents a fundamental operation in many different contexts such as clinics, rehabilitation, industry, sports, and ergonomics. Model validity was assessed through both synthetic data and data acquired from a real collaborative robot for more than 20 minutes of continuous motion to assess its robustness to drift during a typical amount of time for upper limb rehabilitation (Brogårdh & Sjölund, 2006).

4.2 The unconstrained joint kinematics and the DoMoMEA project

4.2.1 The stroke event and the role of telerehabilitation

The DoMoMEA is a project funded by Sardegna Ricerche aimed at developing a mobile health solution based on the wearable sensors to deliver a neurorehabilitation therapy at home of the patients who had survived a stroke. Cerebral stroke is a highly disabling pathology causing different levels of motor skills impairment primarily depending on the affected size and side (Harari & Liao, 2010). In addition, stroke is one of the major causes of death and disability with several societal and economic issues associated. Survivors have to follow a long rehabilitation programme which consists of two main phases for mild impaired patients: in the hospital and at home after discharge (Aziz et al., 2013). In the second phase, subjects are asked to autonomously follow a series of instructions (Lynch et al., 2017) focused on the daily-life activities recovery to pursue a full reintegration into the society. However, the lack of supervision during the exercises, the repetitive nature of the latter and the limited engagement often induce dropouts already in the short-medium term (Maclean et al., 2000), compromising the successful of their movement abilities recovery. It is nonetheless important to consider that additional intense rehabilitation interventions, when delivered after six months from the stroke event, can lead to further benefits if compared to the typical interventions which are limited to first four months, as highlighted in (Winters, 2002) and shown in Figure 34.

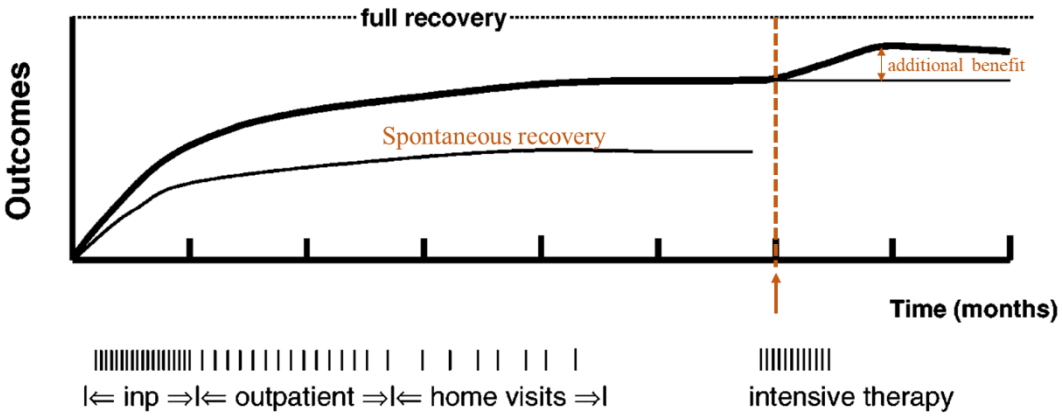

Figure 34: the typical recovery trend after a stroke. The orange vertical dashed line represents the beginning of additional intensive therapy delivered after six months from the stroke event. Figure adapted from (Winters, 2002).

In this context, wearable sensor-based telerehabilitation systems with remote monitoring may represent a potential solution to support the early discharge of the patients just after the primary hospital treatments with a consequent cost reduction for both the patients and the national health system, but still providing an adequate level of rehabilitation. In fact, as previously mentioned, some relevant biomechanical parameters can be quantitatively estimated starting from the MIMU orientation to assess the patients' performance and the compliance to the physical protocol. Additional advantages of the telerehabilitation systems include the autonomy developed by patients and the fact that the need for assistance is limited to some technical support at home rather than bringing them to the rehabilitation centres. However, the lack of supervision during the exercises can be the cause of uncorrected compensatory movements, defined as the unnatural and erroneous movements aimed to the achievement of the desired goal (Levin et al., 2009). Since the compensatory movements can determine muscle and joint pain in the long-term, their detection and reporting should be a prerogative of each telerehabilitation system.

The following section describes the DoMoMEA system which, based on wearable sensors, offers patients the possibility of a full-body rehabilitation protocol and the monitoring of the common execution errors.

4.2.2 The DoMoMEA system: description and architecture

The implementation of the exergames in Unity 3D and the telemedicine framework have been developed by the colleagues from the University of Cagliari, as published in (Zedda et al., 2020).

The general architecture of the DoMoMEA system (which in Sardinian language means “my home”) is shown in Figure 35 and it is specifically designed to guide the patient step-by-step during the rehabilitation session. The system consists of the patient’s environment and the telemedicine framework. The latter includes the clinician’s environment and a server to connect the patient with the clinician. The transmission of the rehabilitation data allows the clinician to evaluate the patients’ progress.

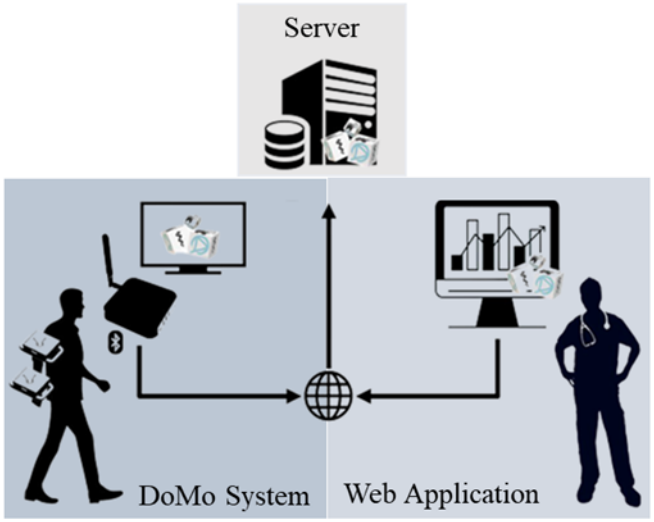

Figure 35: the DoMoMEA system includes the patient’s environment (on the left), the clinician’s environment (on the right) and the server useful to connect both environments (on the top). Data are collected locally, stored, and forwarded through the Internet to a remote server managing a database. The clinician and the patient can access the data by a web application. Figure taken from (Zedda et al., 2020).

Patient’s environment

The patient’s environment includes up to seven low-cost MIMUs (MuSe, manufactured by 221 s.r.l., Padova, Italy https://www.221e.com/muse/) to be attached to the main body segments (trunk, upper arm, forearm, hand, pelvis, thigh, shank, and foot) through custom-designed soft and flexible neoprene straps (Ortopedia Chessa, Cagliari, Italy, https://www.ortopediachessa.it/it/home3.html). The bands were made up of an open-cell 2.5 mm neoprene substrate (styrene butadiene rubber) overlaid, on one side, with a tick Velcro-plush layer for keeping the sensors firmly in a specific position during The exercises. The setup is shown in Figure 36. Each MuSe embeds a triaxial accelerometer (measurement range up to ±16 g), a triaxial gyroscope (measurement range up to ±4000 dps), a triaxial magnetometer (measurement range up to ±50 Gauss), a 32-bit ARM Cortex-M4

microprocessor, a dual-mode Bluetooth v 3.0 module, a local storage, and a rechargeable lithium battery. All the MuSe employed in this study underwent a calibration refinement and a complete characterization to assess their noise level before conducting the experiments, following the tests described in Chapter 2. The use of the MIMUs was preferred to that of RGB-D cameras due to their immunity to optical occlusion problems very likely when monitoring such a variety of human joints (Balta et al., 2020). The orientation is estimated on the microcontroller of each MIMU by fusing the gyroscope and the accelerometer signals. The magnetometer contribution is excluded due to the high probability of ferromagnetic disturbances since the DoMoMEA is conceived to be used at patients' home where a lot of electrical appliances and magnetic materials are present (Roetenberg et al., 2003). The SFA chosen for estimating the orientation is MAD since it involves the selection of a single parameter value and it is suitable for fast calculations as reported in (Caruso, Sabatini, Laidig, et al., 2021). The orientation estimated by each MIMU is sent via Bluetooth to a low-cost Android TV-box (MINIX-NEO U9-H, Android Marshmallow 6.0.1 OS, 2 GB DDR3 32-bit RAM, Mali-820 MP3 GPU, an octa-core 64-bit Cortex A53 Processor, Wi-Fi connection, and rendering video frequency equal to 60 frames per second).

Figure 36: the seven MIMUs and some elastic bands. The thick arrow on the top of each MIMU is useful for the alignment with the longitudinal axis of each body segment.

The orientation of the MIMUs attached to the segments involved in a specific exercise are sent to the MINIX via Bluetooth at 50 Hz. Then, the joint kinematics is computed in near real-time on the MINIX by means of custom-made C# routines. The joint angle time-series is used both to animate the exergames and to monitor compensatory movements reported to the subjects by a series of messages. In addition, the main parameter of amplitude and duration of each joint angle time-series are stored locally and forwarded to a server to be remotely accessible by the clinician. To maximize the patients' engagement the MINIX is connected to a wide screen through a HDMI cable where the exergames together with the motivational messages and qualitative/quantitative feedbacks are displayed using numbers, colors, text, and audio messages. Moreover, the exploitation of the TV reduces the digital divide, provide access to the technology to patients with reduced computer literacy, and do not have a care-related or stigmatizing connotation, compared to other stand-alone telerehabilitation instruments (Macis et al., 2015). As anticipated, the rehabilitation protocol has been designed by the clinicians of the University of Cagliari to help the joint recovery and muscle strengthening of the body limbs. In particular, nine planar exercises are proposed to the patients, as summarized in Table XIV.

Table XIV: the DoMoMEA rehabilitation exercises relative to upper limbs, lower limbs, and trunk.

Right and left upper limbs	• Shoulder ab/adduction • Elbow flexion/extension • Wrist flexion/extension
Right and left lower limbs	• Hip flexion /extension • Knee flexion /extension • Ankle dorsal/plantarflexion
Trunk	• Trunk rotation around the vertical axis • Trunk rotation around the antero-posterior axis • Trunk flexion/extension

One exergame for each rehabilitation exercise has been developed in Unity 3D by the colleagues from the University of Cagliari, as published in (Zedda et al., 2020) and consists of the following four main scenes:

1. In the first scene, the patient is given the instruction to properly wear the MIMUs.
2. In the second scene, a quick tutorial of the correct execution of the exercise is presented.
3. The main scene in which the interface changes according to the movements performed by the patient during the execution of the therapeutic exercise.
4. A final scene summarizing the performance achieved in that exercise (in terms of ROM and execution time).

Some exergames also include a serious interface which consists in a bar filled proportionally to the joint angle amplitude. The scene embeds additional fundamental elements such as a box which displays the number of repetitions correctly executed with respect to the total repetitions intended for that exercise, the execution time of each repetition, and an area for either motivational or warning messages. The same information is also reported in the exergame version aimed at visualizing the rehabilitation exercise by means of avatar and animation tools (e.g., paintbrush, motorcycle, arrows, balls, …).

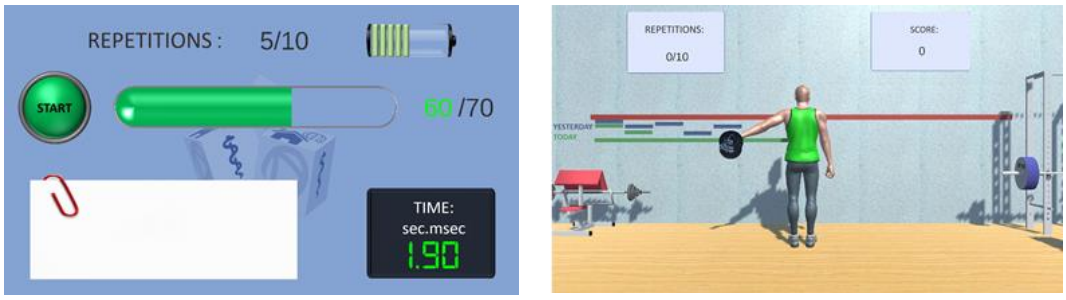

Figure 37: the serious interface (on the left) and the avatar (on the right). The feedback elements are present in both type of interfaces.

During the execution of the exercise, a real-time algorithm running on the MINIX segments the joint angle time-series in each repetition and extracts the amplitude parameters (maximum, minimum, ROM), the directional parameters (ascending and descending parts), and temporal parameters (ascending and descending time). Two additional scenes to compute the gyroscope biases and to perform the anatomical calibration of the trunk and the pelvis (as detailed in the

following paragraph) are run before the execution of the exergames. In the former, the angular velocity readings for each gyroscope are transmitted to the MINIX where the mean value is computed and sent back to the MIMU to be removed from the following measurements before running the SFA, in accordance with the Chapter 2 guidelines.

Telemedicine framework

The quantitative parameters extracted during the analysis of the exergames are collected in a *.json* file for each exercise. When the Internet connection is available these files are sent remotely using a store-and-forward approach, ensuring the constant monitoring by therapists, which can retrieve the information graphically and numerically by a custom web application. The clinician can also interact with the patient by a messaging service and to modify the parameters associated to his/her motor skills. By doing so, it is possible to adapt the goal based on the rehabilitation progresses thus obtaining a good engagement of the patient throughout the therapy. Advanced security aspects enable the safe management of the subjects' personal data: all files are sent to the server through a HTTPS protocol-based communication subjected to authenticated POSTs. Moreover, in order to ensure a secure data transfer, a SSL protocol-based virtual private network access is installed on both the client device and the server.

4.2.3 Joint kinematics estimation without the magnetometer

Developed methods

This paragraph presents the principles and the main equations adopted to estimate the joint angle time-series starting from the orientation of the two MIMUs attached to the proximal and distal segments of the joint under analysis. Let consider the general situation shown in Figure 38 in which the anatomical axes of the proximal and distal segments are represented using the "A_p" and "A_d" subscripts, respectively. The definition of both A_d and A_p is standardized by the ISB guidelines and relies on the main anatomical landmarks and underlying bone orientations (Wu et al., 2002, 2005). In general, the axes are defined to be aligned along the longitudinal, medio-lateral, and antero-posterior directions. The two segments are connected by a spherical joint which allows three DoFs. The joint kinematics is defined as the relative orientation between the A_d and A_p expressed in the A_p coordinate system, as follows:

$$^{A_p}\boldsymbol{q}_{A_d} = \boldsymbol{q}_{A_p}{}^{*} \otimes \boldsymbol{q}_{A_d} \tag{25}$$

The $\boldsymbol{q}_{A_p}$ and $\boldsymbol{q}_{A_d}$ are the actual and unknown orientation of the proximal and distal anatomical coordinate systems, respectively, and are expressed with respect to a common GCS. Then, the relative orientation $^{A_p}\boldsymbol{q}_{A_d}$ is decomposed in the corresponding Euler triplets using the sequences defined by the ISB standards.

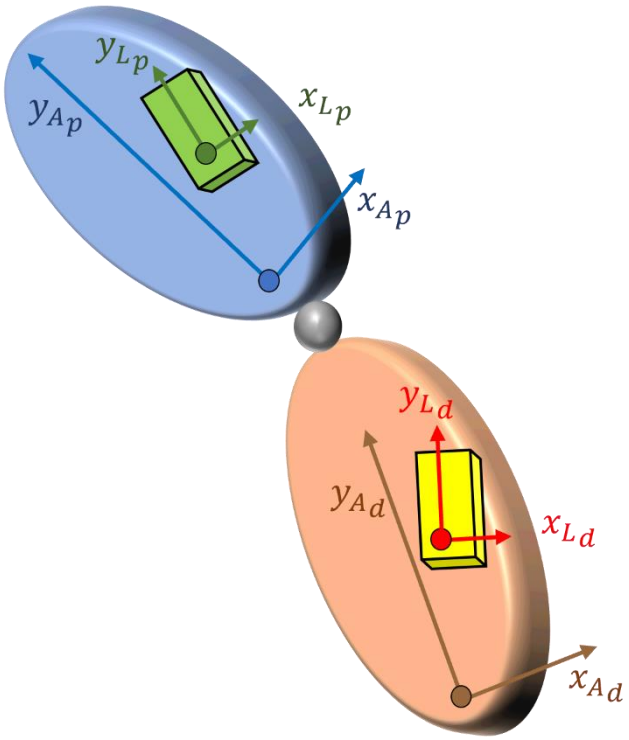

Figure 38: the proximal (in blue) and distal (in brown) segments are connected by a spherical joint. The MIMU technical axes are in general not aligned with the anatomical one. For the sake of simplicity, the z-axis of each segment and MIMU was not represented. “p” = proximal, “d” = distal.

As it can be seen in Figure 38, the first encountered limitation when estimating the joint kinematics using MIMUs is the non-alignment between the LCS of each MIMU (also known as technical axes) and the relevant anatomical axes. In fact, the MIMUs are placed on the skin in locations chosen to minimize the soft tissue artefact and to avoid movement restrictions. This means that, in general:

$$\begin{aligned} \boldsymbol{q}_{A_p} &\neq \boldsymbol{q}_{L_p} \\ \boldsymbol{q}_{A_d} &\neq \boldsymbol{q}_{L_d} \end{aligned} \tag{26}$$

The $\boldsymbol{q}_{L_p}$ and $\boldsymbol{q}_{L_d}$ are the orientation of the proximal and distal MIMUs, respectively, as estimated by a SFA. To correctly estimate the joint kinematics, it is necessary to know the rigid and time-invariant relation between the anatomical and technical axes for each segment. This operation is usually named "sensor-to-segment alignment". Different methods have been proposed in the literature over the years to face with this non-trivial issue. Among the most established it is possible to include:

- The manual alignment to match as much as possible the orientation of the technical and the anatomical axes.
- A functional calibration to estimate the orientation of the anatomical axis relative to those of the MIMU by exploiting the direction of the angular velocity vector measured during "pure rotations" of the segment along the direction of the anatomical axis of interest (Cereatti et al., 2015). This method should be performed for at least two axes.
- A direct anatomical landmark identification in which an *ad hoc* device (e.g., a caliper) carrying an extra MIMU is used to exploit the bone morphology by pointing to palpable landmarks. This method allows the direct identification of the anatomical axis direction with respect to the MIMU axes.

The advantage of the functional calibration is that it provides a direct estimation of the relation between the anatomical and technical axes of the segment under analysis. However, the accuracy of this method depends on the ability of the subjects to replicate a pure movement around a specific axis which can be hardly feasible for some joints without a dominant and well-defined DoF (e.g., the rotation about the longitudinal tibia). A recent article also highlights the ineffectiveness of the function calibration in improving the accuracy of the thorax and lumbar angles (Cottam et al., 2021). Moreover, the functional calibration can be effective when passive movements are performed by experts (Cutti et al., 2010) which is not the case of the telerehabilitation systems designed to be used without the in-person supervision. Despite the method based on the anatomical landmarks identification was proven to provide accurate results (Picerno et al., 2019), it requires an additional custom-device and an extra weel-calibrated MIMU. In addition, these two methods are time consuming and require expertise thus resulting in additional requirements not compliant with the DoMoMEA goal of

simplicity and minimum effort for patients. At the end, the manual alignment was chosen to solve the sensor-to-segment alignment issue as a trade-off between simplicity and accuracy. In fact, the user is guided by the tutorials provided in the first scenes of the exergames to properly wear the MIMUs. In addition, the main axis direction is clearly reported on the MIMU top case with a thick arrow to be aligned along the longitudinal axis of the body segment under analysis (Figure 36). Recently, a usability study (currently under review) was conducted by the University of Cagliari where participants were asked to fill two questionnaires to evaluate their experience in exercising with the DoMoMEA system. The participants were not trained on the use of the platform but only a description of the functionalities of the different components was given at the beginning. Results suggest a high usability level and highlight the simplicity of the adopted solution which avoids time consuming calibration procedures. Finally, a test-retest study is being conducted to quantify the reproducibility of the manual alignment method. For the above reasons, from herein, the technical and anatomical axes of each body segment will be considered as aligned (i.e., $\boldsymbol{q}_{A_p} \equiv \boldsymbol{q}_{L_p}$ and $\boldsymbol{q}_{A_d} \equiv \boldsymbol{q}_{L_d}$). The only two exceptions are represented by the trunk and the pelvis for which an additional refinement of the manual alignment is implemented due to the possible tilted body surfaces which may significantly prevent the MIMU technical axes from being aligned with the corresponding anatomical axes. In the following the proposed refinement is described for the thorax, but it also applies equally to the pelvis (Figure 39).

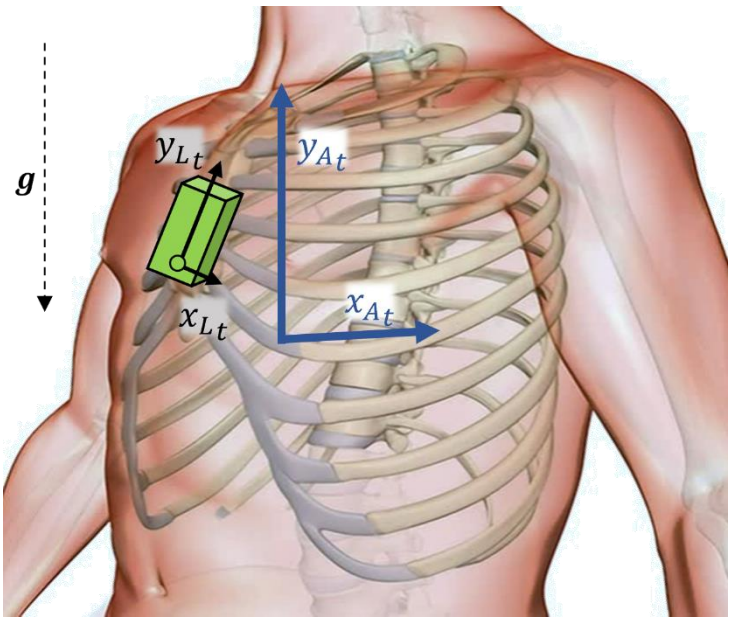

Figure 39: the LCS of the MIMU attached to the thorax and the corresponding anatomical axes. It is possible to assess that due to the physiological curved surface, the two set of axes are not aligned. Images taken from (https://figebo.it/tac/tac-torace/). "t" = thorax.

In this situation, it is possible to exploit the hypothesis that the thorax longitudinal anatomical axis (represented in blue) is aligned with the gravity direction when standing up. Thus, the realignment quaternion ${}^{L_t}\boldsymbol{q}_{A_t}$ is obtained by computing the relative inclination (in terms of a rotation angle and axis) between the gravity vector measured by the accelerometer ($\boldsymbol{a}_{L_t}$) and the ideal vector ($\boldsymbol{g}_{A_t}$, i.e., the vector that would be measured if the MIMU axes were perfectly vertical), equation (27).

$$\begin{aligned} \delta &= \cos^{-1}\left(\frac{\boldsymbol{a}_{L_t}}{|\boldsymbol{a}_{L_t}|} \cdot \frac{\boldsymbol{g}_{A_t}}{|\boldsymbol{g}_{A_t}|}\right) \\ \boldsymbol{k} &= \frac{\boldsymbol{a}_{L_t}}{|\boldsymbol{a}_{L_t}|} \times \frac{\boldsymbol{g}_{A_t}}{|\boldsymbol{g}_{A_t}|} \end{aligned} \tag{27}$$

The ${}^{L_t}\boldsymbol{q}_{A_t}$ is computed by applying the definition of quaternion, as follows:

$${}^{L_t}\boldsymbol{q}_{A_t} = \left[cos\left(\frac{\delta}{2}\right), k(1)sin\left(\frac{\delta}{2}\right), k(2)sin\left(\frac{\delta}{2}\right), k(3)sin\left(\frac{\delta}{2}\right)\right] \tag{28}$$

Finally, the orientation computed by the SFA for the MIMU attached to the thorax ($\boldsymbol{q}_{L_t}$) during the exergames is referred to A_t:

$$\boldsymbol{q}_{A_t} = \boldsymbol{q}_{L_t} \otimes {}^{L_t}\boldsymbol{q}_{A_t} \tag{29}$$

To this end, a preliminary acquisition of a few seconds with the subject still on the neutral position is acquired prior to execute the rehabilitation protocol.

A second issue when estimating the joint kinematics without using the magnetometer is the lack of information of the relative orientation between the MIMUs on the horizontal plane. In fact, the absence of the Earth's magnetic field direction makes it impossible the definition of a unique horizontal axis direction of the GCS (which is defined to have the vertical axis aligned with the gravity vector and one horizontal axis aligned with the direction of the Earth's magnetic field projected onto the horizontal plane, as explained in Chapter 3). For this reason, the orientation of two MIMUs cannot be estimated by the SFA with respect the same GCS. This situation is represented in Figure 40 taking the shoulder joint as a reference. The GCSs of the upper arm (G_{ua}) and the thorax (G_t) share the same vertical axis but differs from the direction of their respective horizontal axes.

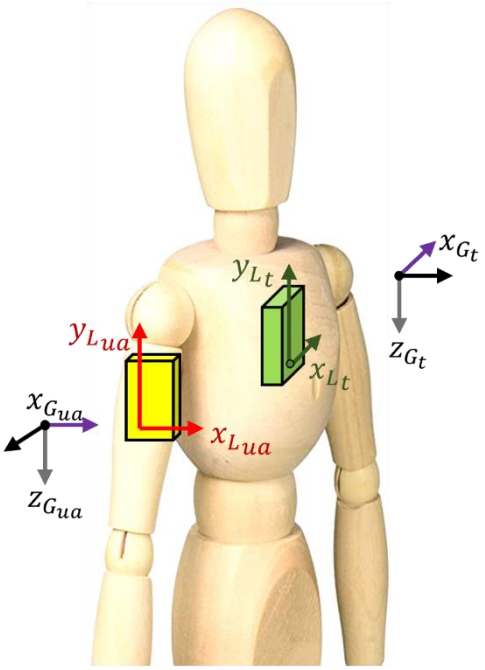

Figure 40: when the magnetometer is not employed, the orientation of each MIMU is estimated with respect a GCS which is not equally defined on the horizontal plane. "ua" = upper arm, "t" = thorax.

However, when the magnetometer contribution is neglected, it is possible to force the direction of the GCS x-axis to be coincident with the MIMU x-axis, as represented in Figure 40. If the MIMUs are properly worn, then the relative orientation between the two GCSs is known *a-priori* in the "zero-joint configuration", i.e., when the joint angle is null. In this specific example case, during the zero-configuration the time-invariant quaternion needed to realign the two GCSs (${}^{G_t}\boldsymbol{q}_{G_{ua}}$) is given by a rotation of +90 deg around the common global z-axis. In other words, this solution, which is robust to the ferromagnetic disturbances, relies on the accurate positioning of the MIMUs on the body segments to define the relationship between the relative orientation of the GCSs in the particular configuration of a null joint angle. The joint kinematics can be finally defined as (remembering that ${}^{G_{ua}}\boldsymbol{q}_{L_{ua}} \equiv {}^{G_{ua}}\boldsymbol{q}_{A_{ua}}$):

$$ {}^{A_t}\boldsymbol{q}_{A_{ua}} = \left({}^{G_t}\boldsymbol{q}_{L_t} \otimes {}^{L_t}\boldsymbol{q}_{A_t}\right)^{*} \otimes {}^{G_t}\boldsymbol{q}_{G_{ua}} \otimes {}^{G_{ua}}\boldsymbol{q}_{A_{ua}} \tag{30} $$

This procedure is then applied to all the joints under analysis since the alignment quaternion between the proximal and distal GCSs can be computed through a combination of elementary rotations. As previously said, the ${}^{A_t}\boldsymbol{q}_{A_{ua}}$ is now decomposed in the triplets of Euler angles following the ISB recommendations to obtain the joint angles of interest.

Analysis of the angle time-series

Since all the exercise included in the DoMoMEA rehabilitation protocol have been conceived to be planar, only the Euler angle corresponding to the rotation around the main axis (e.g., the shoulder ab/adduction angle) is considered both to animate the exergame and to analyze the angle time-series. The amplitude of the secondary rotations (e.g., the upper arm intra/extra rotation angle) is used to monitor the presence of compensatory movements through a threshold approach and to provide feedback.

Focusing on the main rotation, the joint angle time-series is analyzed in real time to quantitively evaluate the execution performance by counting the repetitions (through a double thresholds approach) and computing the ROM and the execution time in both ascending and descending parts. The latter are identified by calculating the derivative of the joint angle after smoothing by means of a 3-tap moving average filter (to introduce a negligible delay). As an example, the time series of the elbow flexion-extension angle is reported in Figure

41. The single repetition is identified when the angle crosses the two thresholds th_1 and th_2 following the order th_1- th_2- th_2- th_1. The execution time is defined as the time which occurs between the two crossing of th_1 in both ascending and descending order. The ROM is defined as the difference between the maximum and the minimum values of the considered angle. In particular, the maximum is searched within the interval corresponding to the repetition, while the minimum is searched within a window of one second width prior to the crossing of th_1.

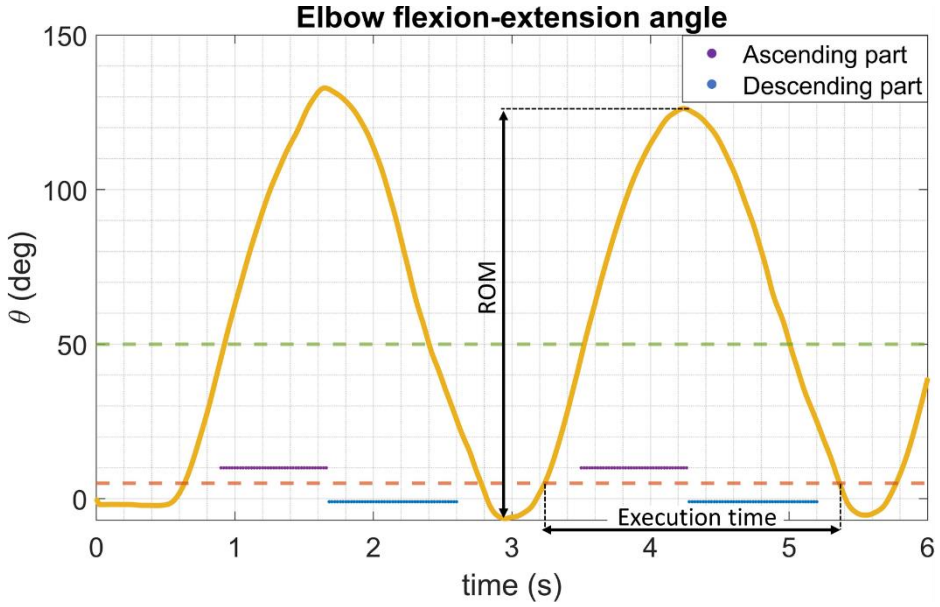

Figure 41: the elbow flexion/extension angle from which it is possible to compute the ascending/descending parts and to define the ROM and the execution time. The value of the thresholds $\boldsymbol{th_1}$ and $\boldsymbol{th_2}$ are represented with the dashed horizontal orange and green lines, respectively.

4.2.4 Validation session

Experimental protocol

To evaluate the accuracy of both the joint angle time-series and the ROM parameters, an *ad hoc* experimental protocol was designed including one healthy subject (age = 26, weight = 75 kg, height = 185 cm) for a preliminary validation. The subject was equipped with 49 markers whose trajectories were acquired by a 12-cameras SP system (Vicon Vero, VICON, Yarnton, England) at 100 Hz. The markers were placed on the skin subject following the Davis protocol (Davis et al., 1991) and the Upper Limb Model developed by GPEM (GPEM s.r.l, Pescara, Italy, https://www.gpem.net/) to include additional output for the shoulder, the

elbow, and the wrist angles. The joint angle references were computed by the VICON proprietary software (Nexus v2.10). The subject worn four MIMUs using elastic bands on the trunk, upper arm, forearm, and hand for the exercises concerning the upper limb and trunk acquisitions (and one additional MIMU on the foot). The MIMUs were then moved to the lower limb (pelvis, thigh, shank, and foot). Only the dominant side was considered. Figure 42 shows an example of the experimental setup.

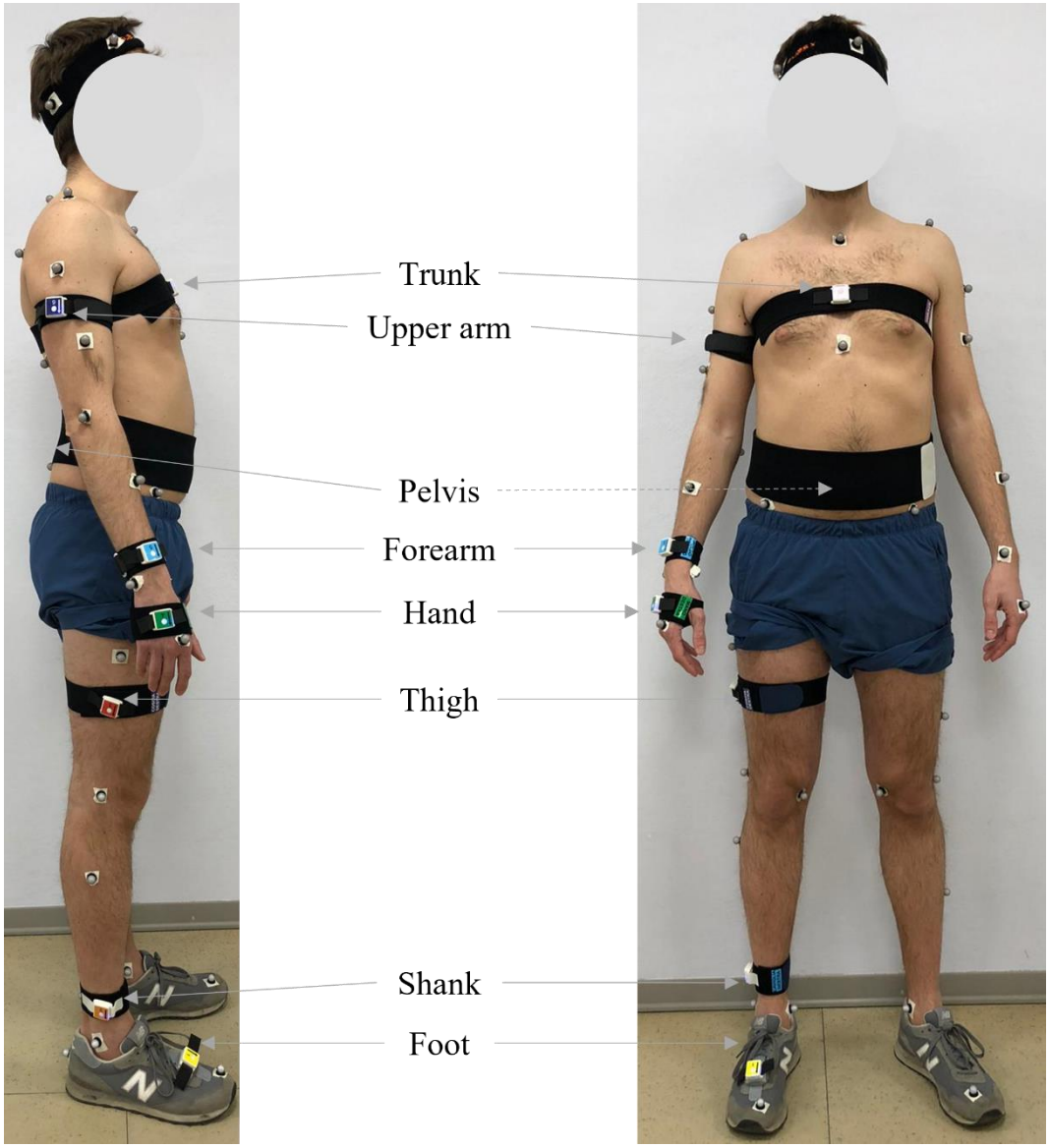

Figure 42: the experimental setup including the markers and the MIMUs.

Inertial data were fused on-board to compute the orientation without using the magnetometer. For each exercise, the quaternions from the two MIMUs involved were streamed to a laptop at 50 Hz using a non-commercial software developed by the 221e company. To synchronize the SP and MIMU systems (which were independent) the force platform integrated with the SP and the accelerometer data from the foot were always acquired to align the corresponding signals in the post-processing by means of mechanical shocks given to the platform with the foot.

The main steps of the experimental protocol are listed below.

- Before the experimental session, all the MIMUs underwent a warm-up of ten minutes to limit the temperature influence on the sensor readings.
- Then, before applying the MIMUs to the subject, the gyroscope signals were acquired in static for three minutes to compute the angular velocity offset which was stored on-board to be automatically removed from the dynamic data before computing the orientation.
- After the MIMUs were mounted to the subject segments, the anatomical calibration was performed by acquiring the trunk and pelvis accelerometer data for ten seconds (to perform the mathematical realignment).
- The subjects sat on a chair without the back support (not to occlude the markers) in the center of the capture volume and with a foot above the force platform.
- For each exercise of the nine exercises, a single recording was acquired when performing the following steps:
    1. The subject hit the force platform with the foot for three times to allow the identification of the first synchronization point in the post-processing.
    2. The subject performed the first series of the exercise for ten repetitions keeping the amplitude at about 1/3 of the possible ROM (small amplitude).
    3. After a pause of about ten seconds, the point #2 was repeated at about 2/3 of the possible ROM (medium amplitude).
    4. After a pause of about ten seconds, the point #2 was repeated at 3/3 of the possible ROM (large amplitude).
    5. Point #1 was repeated to allow the identification of the second synchronization point in the post-processing.

- The whole previous point was repeated similarly to acquire a second recording of each exercise.

To sum up, at the end of the experimental session, each of the nine exercises was repeated twice at three different amplitudes to test the accuracy of the proposed methods in accurately computing the joint angle in different scenarios.

Data processing and analysis

The SP data were processed in Nexus to provide the joint angle reference. After that, the SP and MIMU data were cut in MATLAB for each recording between the two synchronization points and then linearly interpolated at 100 Hz to have the same time length. The MIMU joint angle was obtained as described in paragraph 0. Finally, the synchronization of the SP and MIMU angle time-series was refined by applying the cross-correlation technique to minimize the horizontal (time) shift for each exercise and for each amplitude. An example of synchronized time-series obtained from MIMU and SP data is reported in Figure 43.

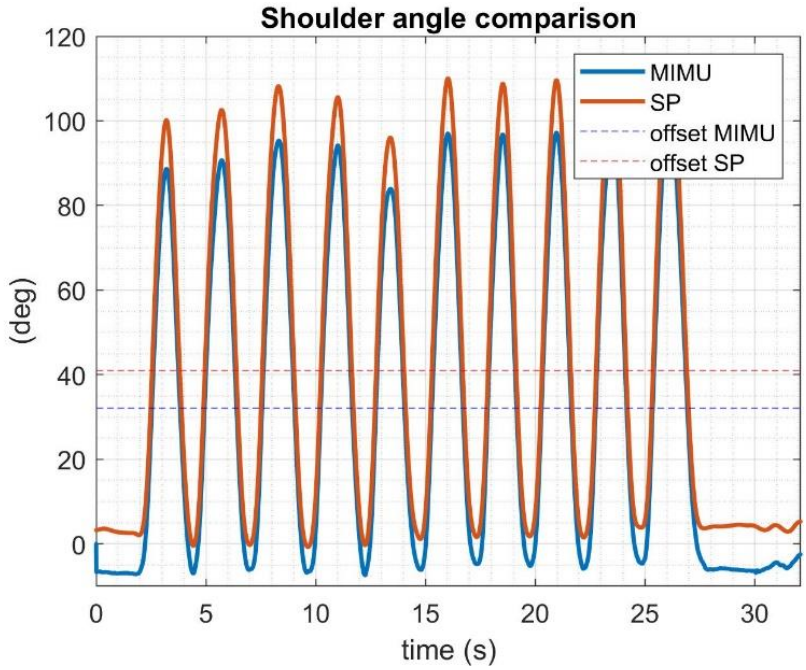

Figure 43: the synchronized time-series of the MIMU and SP-based joint angles for the large amplitude. The corresponding mean values (offsets) are also reported with dashed lines.

The accuracy of the MIMU-based joint angle was then evaluated in terms of RMS of the difference (RMSD) from the corresponding SP-based angle after having removed their mean values, as follows:

$$RMSD = RMS((W_{SP} - mean(W_{SP}) - (W_{MIMU} - mean(W_{MIMU})) \quad (31)$$

The W_{SP} and W_{MIMU} refer to the SP and MIMU-based time-series of the angles, respectively. The mean value was removed due to a different definition of the anatomical reference system from the two systems as explained in (Picerno et al., 2008) resulting in an offset shift between W_{SP} and W_{MIMU} which is meaningless for a comparison purpose.

The accuracy was also evaluated in terms of ROM which was computed for each repetition (as illustrated in Figure 41) for both SP and MIMU-based joint angles. Finally, the ROM values corresponding to the same amplitude were averaged. The average ROM error was computed for each amplitude and exercise by comparing the MIMU and SP average values. In addition, being DoMoMEA a longitudinal study, it is of particular interest the accuracy in the detection of the rehabilitation progresses in terms of amplitude of ROM. For this reason, the medium-to-small and large-to-medium differences were computed for MIMU and SP system separately and then subtracted to assess the amplitude difference error.

Results

The results of RMSD are reported in Table XV.

Table XV: the RMSD obtained for each exercise and for each amplitude. “aa” = ab/adduction, “fe” = flexion/extension, “dp” = dorsi/plantar flexion, “v” = vertical, “ap” = antero-posterior, “ml” = medio-lateral, “avg” = average.

RMSD	Upper limb			Lower limb			Trunk rotation		
(deg)	Shoulder aa	Elbow fe	Wrist fe	Hip fe	Knee fe	Ankle dp	v axis	ap axis	ml axis
S #1	1.0	3.7	3.3	0.6	1.2	0.9	2.2	0.8	1.6
S #2	1.6	3.8	2.4	0.8	1.5	0.9	1.8	0.9	2.1
M #1	1.4	4.2	3.1	0.6	1.1	1.1	2.3	1.1	2.0
M #2	2.2	5.5	2.6	0.8	1.2	1.3	2.3	0.9	2.6
L #1	2.1	4.4	3.4	0.6	1.2	1.0	2.8	0.8	3.2
L #2	2.8	4.6	2.8	0.9	1.1	1.3	3.1	0.7	3.6
Avg	**1.9±0.6**	**4.4±0.7**	**2.9±0.4**	**0.7±0.1**	**1.2±0.1**	**1.1±0.2**	**2.4±0.5**	**0.9±0.1**	**2.5±0.8**

The results relative to the average ROM errors (in bold, white background) and the medium-to-small and large-to-medium difference errors (in bold, green, and blue background) for upper limb, lower limb, and trunk are reported in Table XVI, Table XVII, and Table XVIII respectively.

Table XVI: upper limb joints. The average ROM and the corresponding errors are reported for each amplitude in the cells with white background. The medium-to-small (M-S) and large-to-medium (L-M) differences and the corresponding errors are reported in the cells with green and blue background, respectively. "Δ" = difference.

ROM	Shoulder			Elbow			Wrist		
(Deg)	MIMU	SP	**Δ**	MIMU	SP	**Δ**	MIMU	SP	**Δ**
S	52.6	54.5	**1.9**	an74.1	65.2	**-8.9**	31.1	28.6	**-2.0**
M	70.7	73.8	**3.1**	92.6	83.0	**-9.6**	46.6	43.1	**-3.5**
L	100.9	105.6	**4.7**	131.4	123.8	**-7.7**	61.5	60.1	**-1.3**
M-S	18.0	19.3	**1.3**	18.5	17.7	**-0.8**	15.5	14.5	**-1.7**
L-M	30.3	31.9	**1.6**	38.8	40.8	**2.0**	14.8	17.1	**2.3**

Table XVII: lower limb joints. The average ROM and the corresponding errors are reported for each amplitude in the cells with white background. The medium-to-small (M-S) and large-to-medium (L-M) differences and the corresponding errors are reported in the cells with green and blue background, respectively. "Δ" = difference.

ROM	Hip			Knee			Ankle		
(Deg)	MIMU	SP	**Δ**	MIMU	SP	**Δ**	MIMU	SP	**Δ**
S	18.5	17.4	**-1.1**	44.1	46.4	**2.3**	20.2	21.8	**1.6**
M	24.7	23.6	**-1.1**	55.4	57.0	**1.6**	22.8	25.6	**2.8**
L	31.7	30.4	**-1.3**	75.3	74.7	**-0.6**	25.7	28.6	**2.9**
M-S	6.1	6.2	**0.1**	11.4	10.6	**-0.8**	2.7	3.8	**1.1**
L-M	7.0	6.7	**-0.3**	19.9	17.7	**-2.2**	2.8	2.9	**0.1**

Table XVIII: trunk joint. The average ROM and the corresponding errors are reported for each amplitude in the cells with white background. The medium-to-small (M-S) and large-to-medium (L-M) differences and the corresponding errors are reported in the cells with green and blue background, respectively. "Δ" = difference.

ROM	Trunk rotation (v axis)			Trunk rotation (ap axis)			Trunk rotation (ml axis)		
(Deg)	MIMU	SP	**Δ**	MIMU	SP	**Δ**	MIMU	SP	**Δ**
S	46.1	43.7	**2.4**	32.5	28.5	**4.0**	22.3	31.6	**-9.2**
M	62.7	59.0	**3.7**	42.8	39.4	**3.4**	28.9	39.0	**-10.1**
L	98.0	94.2	**3.8**	53.8	49.0	**4.9**	54.1	68.0	**-13.9**
M-S	16.6	15.3	**1.3**	10.3	10.9	**0.6**	6.6	7.5	**-0.9**
L-M	35.3	35.2	**0.1**	11.0	9.6	**-1.4**	25.1	29.0	**-3.8**

Discussion

From the results reported in Table XV, it is possible to assess that the average RMSD values are lower than 4.5 deg. This represents an encouraging achievement being the errors lower under the acceptability threshold of 5 deg when comparing the joint kinematics estimated with two different systems (McGinley et al., 2009). In addition, results seem to be quite independent from the amplitude of motion. The elbow is the joint most affected by the different definition of the anatomical axes as highlighted by the higher errors. In particular, the most critical factor is the different definition of the upper arm axes which, for the SP, relies on the shoulder joint center which in turn is influenced by the shoulder ante/retropulsion which cannot be detected by the MIMU positioned on the upper arm. Regarding the average ROM errors reported in Table XVI, Table XVII, and Table XVIII all the values are lower than 5 deg but for the elbow and the trunk rotation around the medio-lateral axis (i.e., flexion/extension) whose values amount to 8.7 and 11.1 deg, respectively. In particular, the errors increased with the amplitude for the trunk flexion/extension. This could be explained by the fact that during such a movement the trunk can no longer be considered as a single rigid body due to the curvature of the spine which increases with the flexion angle. While the SP defines the trunk angles also considering the pelvis, in DoMoMEA the trunk motion is monitored using a single MIMU mounted on the stern, thus making a meaningful comparison impossible. Considering the medium-to-small and large-to-medium differences, it is possible to assess that all the errors are lower than 4 deg and equal to 1.2 deg on average. As previously said, one of the goals of the DoMoMEA project is the long-time monitoring of the patients' rehabilitation progress. To this end, an accurate detection of the changes

in the ROM values is central. In general, it is worth noting that since MIMU and the markers are attached on the subject's skin in different locations, the relevant measurements are necessarily affected by different soft tissue artifacts which may have enhanced the errors. To conclude, it must be also recognized that the limited acceleration magnitudes typical of this kind of rehabilitation protocols represent a favorable effect for the SFA which can rely on the accelerometer measurements to compensate for the inclination drift.

Limitations and future developments

The absence of the magnetometer, necessary to avoid unforeseeable ferromagnetic disturbances, has required the development of joint kinematics algorithms to rely on the predefined MIMU positioning on the subjects' skin. However, despite its simplicity, this solution has inherent limitations such as the round surfaces which prevent the MIMUs from being accurately aligned along the segment axes. Furthermore, the assumption of the sensor-to-segment alignment to be time invariant may not be always true due to the soft tissue artifacts which can be different among the patients (Leardini et al., 2005; Peters et al., 2010). A test-retest is currently being conducted to analyze the reproducibility of the manual alignment and its influence on the result accuracy. Ten healthy subjects have been enrolled one week after the test to repeat the exercise at the maximum amplitude which, among the three, ensures the most reproducible results. As opposite to the sensor fusion methods employing both the accelerometer and the magnetometer, the lack of the magnetic reference no longer allows to mitigate the drift due to the angular velocity integration along the vertical axis. This forces the use of the MIMUs to a limited amount of time (e.g., few minutes). For this reason, the exergames were designed to be reinitialized after each series of ten repetitions ($\approx$ one minute). In addition, every time that the system is powered on, the gyroscope bias is computed and removed from the angular velocity readings before estimating the orientation. Despite helpful, this procedure is not completely effective. In fact, the bias exhibits non-negligible run-to-run changes resulting in a time-variant residuals which cannot be completely compensated for. At the current time, maintaining this simple setup, the above-mentioned limitations could be only overcome using higher performant sensors conceived for military and tactical uses (Cereatti et al., 2017). Future investigations are needed to analyze the joint kinematics accuracy on post-stroke patients in *ad hoc* clinical trials.

4.3 The constrained joint kinematics: applications to a robotic arm

4.3.1 A new approach to strengthen the joint kinematics estimation

In the light of the limitations discussed in the previous section, it is necessary to develop additional modelling strategies to overcome the inherent issues related to the use of MIMU when estimating the joint kinematics. Considering the situation illustrated in Figure 40, as previously explained, when the movement does not involve the trunk (TR), a first simple solution to estimate the shoulder angles consists in aligning the upper arm (UA) MIMU with the humerus anatomical axes and computing the relative orientation with respect to an initial anatomical posture. The elbow angles can be estimated as the relative orientation between the UA MIMU and the MIMU attached to the forearm (FA) and aligned with its anatomical axes. A clinically relevant joint kinematics description in terms of Euler angles can be then obtained by decomposing relative orientations according to ISB standard sequences. Even if easy and fast to apply, this technique (referred as model-free) does not consider the joints physiological range of motion nor the maximum angular change at each time step. This means that errors in the MIMUs orientation directly affect the quality of joint kinematics estimates, possibly reflecting in non-physiological joint angular accelerations and ranges of motion. Finally, another limitation of the model-free approach is the possibility of mathematical singularities when performing exercises characterized by large amplitudes. For these reasons, it is worth introducing a biomechanical model of the human limb to increase the robustness of the estimated quantities through the definition of physiological constraints. Reasonable constraints would include the possibility to set the limit for each joint range and to restrict the maximum angular variation between two consecutive time steps. Considering all the joints of the upper (lower) limb as a whole and not separately represents the strength of this approach. The Denavit-Hartenberg (DH) robotic convention (Siciliano & Khatib, 2009) can be applied in a biomechanical context considering the analogy between the human limb and a robotic chain (Cornagliotto et al., 2021). The DH provides an efficient way to model a chain of rigid links allowing the description of a roto-translation in terms of only four variables instead of the canonical six ones. Focusing on the upper limb and following the ISB definitions, the corresponding joint kinematics can be described through a sequence of five

rotations (three at the shoulder and two at the elbow) and one subject-specific parameter, the carrying angle (Wu et al., 2005).

The aim of this section is to propose a DH model to track the upper limb motion consistently with the corresponding ISB convention. The five angles of the model are obtained at each time step by optimizing (i.e., minimizing) the difference between the modelled UA and FA orientation (with the DH) and the one computed with the SFA combining the accelerometer and gyroscope signals without the aid of the magnetometer (to avoid ferromagnetic disturbances). Relevant angular joint limits are set based on physiological constraints also considering the *a-priori* knowledge of the kinematics variables of the executed movements in terms of both amplitude and maximum angular velocity. The validity of this approach was assessed on synthetic and experimental data acquired on a robotic arm reflecting typical rehabilitation gestures (Brogårdh & Sjölund, 2006). In both cases, to verify the influence of a considerable drift on the final joint angle accuracy, the length of the recordings amounted to about 20 minutes, a typical amount of time for upper limb rehabilitation (Brogårdh & Sjölund, 2006). Finally, a comparison was made between the joint kinematics estimated within the model-optimization framework and the one computed with the model-free approach.

4.3.2 The Denavit-Hartenberg model of the human upper limb

Previous works

Previous literature works have adopted the DH convention to model human upper limbs for generic biomechanical investigations (Cutti et al., 2008; El-Gohary & McNames, 2012; Yang et al., 2009), for rehabilitative purposes (Bertomeu-Motos et al., 2015; Parasuraman et al., 2009; Rahman et al., 2010) or for the improvement of human-robot interaction (Zanchettin et al., 2011). However, some of these works only concentrate on the shoulder and not on the complete upper limb (Yang et al., 2009). Other studies define their DH model without following ISB guidelines (Bertomeu-Motos et al., 2015; Cutti et al., 2008; El-Gohary & McNames, 2012; Parasuraman et al., 2009; Rahman et al., 2010; Zanchettin et al., 2011). Two other works are worth mentioning although not based on the DH convention. The work from (Tagliapietra et al., 2018) exploits the physiological constraints in an optimization framework (openSim) to prevent the joint angle from unfeasible configurations. However, the total amount of experimental time was limited to less than 100 seconds. In similar recent research

by (al Borno et al., 2022) a constrained approach was implemented in OpenSim 4.2 (Delp et al., 2007) to compute the lower limb joint kinematics using a set of eight IMUs during 10-minute walking trials.

The DH convention fundamentals

A graphical representation of the DH convention is shown in Figure 44. The DH defines the pose matrix ${}^{i-1}A_i$ (i.e., orientation and position) of the i^{th} link with respect to the pose of the $i\text{-}1^{\text{th}}$ link by means of four parameters: two distances (d_i and a_i) and two angles (θ_i and α_i). According to the DH convention (Siciliano et al., 2009), each joint is modeled with a single DOF φ_i. If all joints are revolute, then d_i, a_i, and α_i are constant depending only on the geometry of connections between consecutive joints. On the contrary, θ_i is time-varying including φ_i in addition to the geometric parameter. Moreover, the definition of the reference coordinate system orientation (and hence of the four parameters) is not arbitrary but follows the rules imposed by the DH convention.

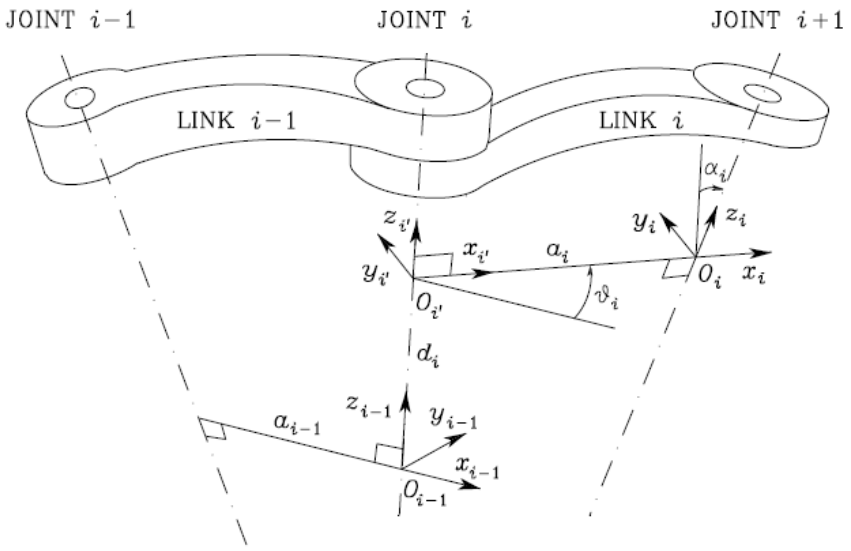

Figure 44: the standard Denavit-Hartenberg convention. Picture taken from (Siciliano et al., 2009).

Once the axes and the parameters are assigned, the DH convention defines the transformation matrix of the i^{th} link with respect to the previous, as follows:

$$ {}^{i-1}A_i = \begin{bmatrix} \cos\theta & -\sin\theta\cos\alpha & \sin\theta\sin\alpha & a\cos\theta \\ \sin\theta & \cos\theta\cos\alpha & -\cos\theta\sin\alpha & a\sin\theta \\ 0 & \sin\alpha & \cos\alpha & d \\ 0 & 0 & 0 & 1 \end{bmatrix} \quad (32) $$

Upper limb model design

In this work, the standard DH convention was adopted to model the human upper limb as a chain of two rigid links: the UA and the FA (represented in Figure 45 in green and in yellow). The length of the two segments amounted to l_{UA} and l_{FA}, respectively. Six revolute joints were defined in agreement with the guidelines of ISB in terms of the rotation sequence and axis orientation. In detail, the shoulder was considered a spherical joint with three DOFs: the elevation plane angle (φ_1), the elevation (φ_2), and the intra-extra rotation (φ_3). The elbow was considered a universal joint with two DOFs: the flexion-extension (φ_4) and the pronation-supination (φ_6). Moreover, a constant subject-specific carrying angle (φ_5) was introduced to model the physiological abduction of FA with respect to UA (Cutti et al., 2008). Since all the joints were revolute, the θ_i was the only variable value depending on φ_i. Considering this model, the DH parameters were defined as reported in Table XIX.

Table XIX: the DH parameters defined to model the upper limb chain.

Link	$\boldsymbol{\theta_i}$	$\boldsymbol{d_i}$	$\boldsymbol{a_i}$	$\boldsymbol{\alpha_i}$
1	φ_1	*0*	*0*	*π/2*
2	φ_2	*0*	*0*	*-π/2*
3	$\varphi_3 - \pi/2$	*-l_{UA}*	*0*	*-π/2*
4	$\varphi_4 - \pi/2$	*0*	*0*	*-π/2*
5	$\varphi_5 - \pi/2$	*0*	*0*	*-π/2*
6	$\varphi_6 - \pi/2$	*-l_{FA}*	*0*	*-π/2*

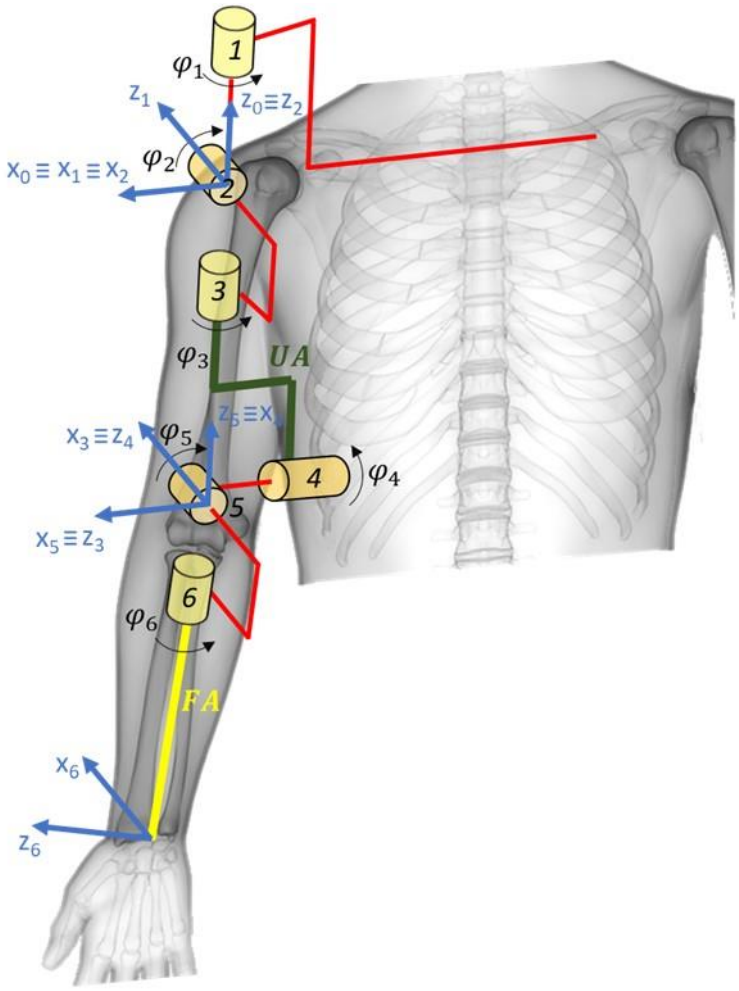

Figure 45: the DH model of the human upper limb in agreement with the guidelines of ISB. The six joints are numbered from 1 to 6. The upper arm and forearm links (3 and 6) are represented in green and yellow, respectively. Links represented in red are characterized by a null length.

Reference system	***center***	***axes***
TR (fixed)	O_0	$(x_0 \quad y_0 \quad z_0)$
UA	O_3	$(x_3 \quad y_3 \quad z_3)$
FA	O_6	$(x_6 \quad y_6 \quad z_6)$

Thus, it is straightforward to obtain the elbow and wrist pose, ${}^{0}_{UA}A$ and ${}^{0}_{FA}A$, respectively, where (x_0, y_0, z_0) is the fixed frame whose axes can be assumed coincident with those of TR.

$$\begin{aligned} {}^{0}A_{UA} &= {}^{0}A_{3} = {}^{0}A_{1}\ {}^{1}A_{2}\ {}^{2}A_{3} \\ {}^{0}A_{FA} &= {}^{0}A_{6} = {}^{0}A_{3}\ {}^{3}A_{4}\ {}^{4}A_{5}\ {}^{5}A_{6} \end{aligned} \tag{33}$$

From ${}^{0}A_{UA}$ and ${}^{0}A_{FA}$ it is possible to identify the 3x3 matrices representing the orientation of the elbow and wrist (${}^{0}R_{UA}$ and ${}^{0}R_{FA}$) and the positions of the two joint centers contained in the three elements of the last columns.

Optimization framework

The idea is to reconstruct the joint configuration time-series $\boldsymbol{\varphi}$ = [φ_1, φ_2, φ_3, φ_4, φ_5, φ_6] starting from the estimates of the UA and FA orientation (from here on referred as "measurements"). In this work, the latter quantities are provided using a SFA fed with MIMU signals and expressed in terms of rotation matrices obtained from the conversion of the corresponding quaternions (Siciliano & Khatib, 2009). More in detail, the estimation of $\boldsymbol{\varphi}$ is performed within an optimization framework based on minimizing the difference between the measurements and the predicted UA and FA orientation (with the DH) consistently with the set constraints. This process and, in particular, the definition of the objective function, are described in Figure 46 for each time-step. In fact, by applying (32) and (33) it is possible to predict the UA and FA orientation given a joint configuration $\boldsymbol{\varphi}$. When the objective function reaches its minimum point then the optimal $\boldsymbol{\varphi}_{opt}$ is found. The goal is to exploit the optimization process to obtain the joint angles consistent as much as possible with the constraints defined. Ideally this process aspires to separate the errors from the measurements and to confine them into the residuals.

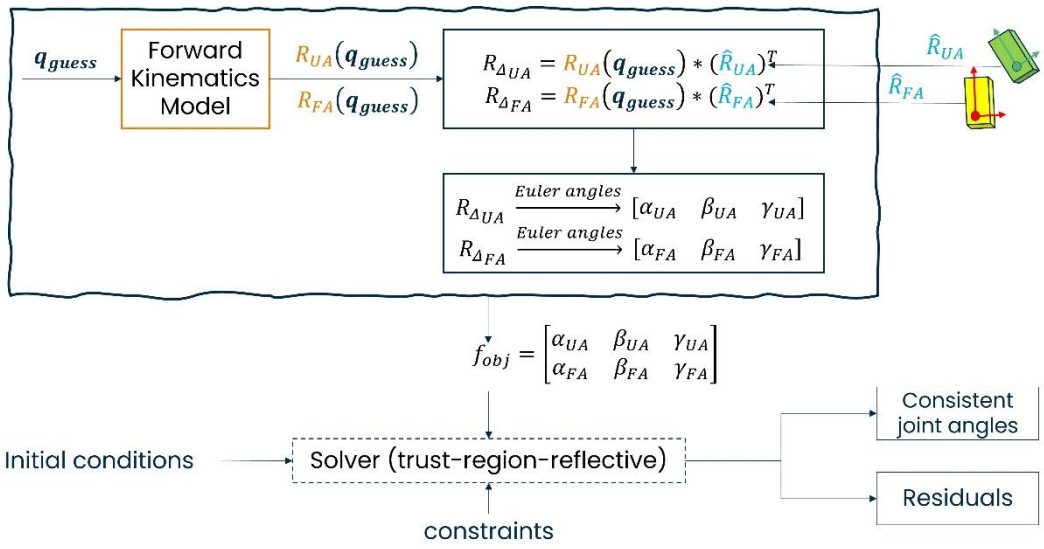

Figure 46: the optimization process to obtain the optimal joint configuration $\boldsymbol{\varphi_{opt}}$ at each time step.

In particular, the working principle is detailed below for each time step:

- Starting from a joint configuration $\boldsymbol{\varphi}$ the UA and FA orientation $R_{UA}(\boldsymbol{\varphi})$ and $R_{FA}(\boldsymbol{\varphi})$ is predicted by applying the forward kinematics described in equations (32) and (33). The initial conditions are usually defined by the initial joint configuration during the static portions at the beginning of the trial.
- The corresponding orientation ($\hat{R}_{UA}$ and $\hat{R}_{FA}$) are estimated using a SFA.
- The differences (in terms of relative orientation) between the predicted orientation $R_{UA}(\boldsymbol{\varphi})$ and $R_{FA}(\boldsymbol{\varphi})$ and their corresponding measurements $\hat{R}_{UA}$ and $\hat{R}_{FA}$ are computed and stored in $R_{\Delta UA}(\boldsymbol{\varphi})$ and $R_{\Delta FA}(\boldsymbol{\varphi})$, which are then decomposed in two sequences of three Euler angles $\boldsymbol{eul}_{UA}(\boldsymbol{\varphi}) = [\alpha_{UA}, \beta_{UA}, \gamma_{UA}]$ and $\boldsymbol{eul}_{FA}(\boldsymbol{\varphi}) = [\alpha_{FA}, \beta_{FA}, \gamma_{FA}]$, respectively (ZYX sequence).
- The objective function $f_R(\boldsymbol{\varphi})$ is defined as the ensemble of $\boldsymbol{eul}_{UA}(\boldsymbol{\varphi})$ and $\boldsymbol{eul}_{FA}(\boldsymbol{\varphi})$.
- The $f_R(\boldsymbol{\varphi})$ is then minimized by using the trust region reflective nonlinear least-squares solver (Coleman & Li, 2006). The minimization starts at the point $\boldsymbol{\varphi}_{guess}$ and finds the minimum of the sum of squares elements contained in $f_R(\boldsymbol{\varphi})$ to obtain $\boldsymbol{\varphi}_{opt}$. In addition, the lower and upper bounds of each component of the $\boldsymbol{\varphi}$ vector are specified by means of

Lagrange multipliers, based on both the physiological range of motion of each joint and, if known *a-priori*, the range of the movement under analysis (Begon et al., 2018). Furthermore, it is possible to constrain the maximum angular change of each $\varphi_i$between two consecutive time-steps based on the expected angular velocity. The minimization is carried out using a "trust-region-reflective" algorithm (Coleman & Li, 2006).

- The $\boldsymbol{\varphi}_{opt}$ is then used to define the next $\boldsymbol{\varphi}_{guess}$ to reduce the time needed by the solver to converge.

It has to be pointed out that when the $\boldsymbol{\varphi}_{guess}$ leads to $R_{UA}(\boldsymbol{\varphi})$ and $R_{FA}(\boldsymbol{\varphi})$ close to the sensor-fusion based orientation, the $f_R(\boldsymbol{\varphi})$ is small thus not resulting in singularities of the Euler angles. This means that this optimization framework is quite insensitive to the chosen Euler sequence to decompose the rotation matrices into the corresponding Euler angles. The output of this process is the vector of the consistent $\boldsymbol{\varphi}_{opt}$ at the current time-step. For a successful optimization, in presence of errors, the residual should not be equal to zero but should contains all the non-idealities which are thus separated from the segment orientation.

4.3.3 Validation session

The proposed optimization method was tested using synthetic and robot MIMU data. In both cases, data were relative to a single motion involving variation in three DoFs which mimicked a shoulder flexion-extension, an elbow flexion-extension, and a forearm prono-supination, simultaneously.

Experimental protocol and data collection

- Synthetic data

In this paragraph the process to obtain realistic noisy accelerometer and gyroscope data is described. To simulate the desired motion φ_1 and φ_3 were set to 90 and -90 deg, while φ_2, φ_4 and φ_6 were varied from 0 to 150 deg and back in three seconds. The trajectory was designed using a 5^{th} order polynomial and imposing to zero the joint angular velocity and acceleration at 0 and 150 deg (Siciliano & Khatib, 2009). This trajectory was repeated for 400 cycles at a sampling frequency equal to 100 Hz for a total amount of time of about 20 minutes to obtain the angular joint configuration reference $\boldsymbol{\varphi}_{ref}$. A recursive process linking accelerations and angular velocities to the $\boldsymbol{\varphi}_{ref}$ was applied to

generate the corresponding ideal MIMU signals. For each MIMU the gravity vector projected on the local coordinate system was then subtracted from the acceleration to obtain the accelerometer output. After that, noise was added to the accelerometer and gyroscope signals of each MIMU. Stochastic characteristics of the added noise in terms of density, bias instability, and velocity (angle) random walk were derived from those computed in static for 18 Xsens – MTw (Xsens, The Netherlands) using the Allan Variance as described in Chapter 2. Table XX reports the selected values for accelerometers and gyroscopes which were equal to the mean value plus three times the standard deviation to simulate a challenging scenario. The deterministic errors were assumed to be perfectly compensated for both the accelerometer and the gyroscope.

Table XX: the selected characteristics of the additive noise for the accelerometer and gyroscope.

Xsens – MTw (18 IMUs)	Accelerometer (mean + 3 STD)		Gyroscope (mean + 3 STD)	
Noise Density	0.0012	$(m/s^2)/\sqrt{Hz}$	0.0079	$dps/\sqrt{Hz}$
Bias Instability	0.0013	m/s^2	0.0054	dps
VRW - ARW	6.9181×10^{-5}	$(m/s^2)/\sqrt{Hz}$	0.0004	$dps/\sqrt{Hz}$

The static noise was generated using the IMU simulation model (Sensor Fusion and Tracking Toolbox, MATLAB R2021b). To simulate the bias residual of the gyroscope (due to run-to-run variation and the stochastic effects described in Chapter 2), two static recordings were generated starting from the same seed. Then, the mean value of the first recording was subtracted from the second gyroscope time-series to replicate what it is commonly performed in the practice. Average residuals amounted to [0.0233, 0.0270, 0.0184] and [-0.0215 -0.0076 -0.0119] dps for UA and FA data, respectively, and are represented superimposed to the corresponding static signals in Figure 47.

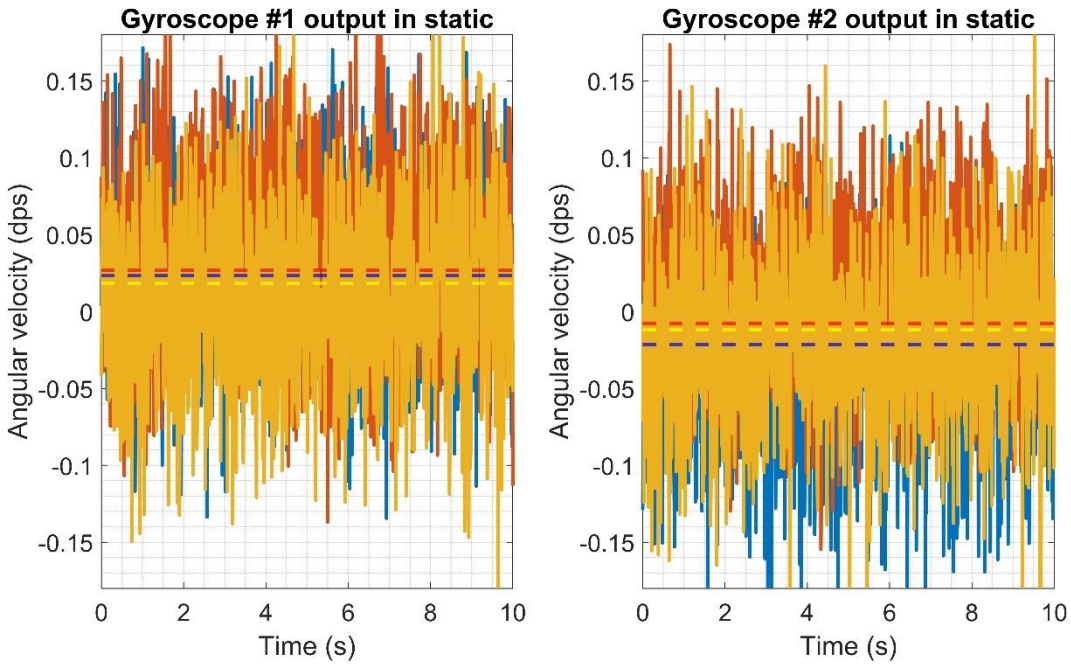

Figure 47: ten seconds of additive gyroscope noise for each MIMU. The offset of each axis is represented with a dashed line (blue = x, red = y, yellow = z).

- Robot data

The collaborative robot chosen for the test was the Kinova Jaco2 (Quebec, Canada) whose maximum angular velocity was 36 dps for all shoulder and elbow actuators, but for prono-supination (48 dps). The robot was firmly fixed on a table. An Ethernet connection was established between the robot and a PC to record data. Acquisitions were made through the software MATLAB at a sampling frequency of about 100 Hz. The inertial motion capture system was composed of two wireless Xsens-MTw MIMUs, both containing a tri-axial accelerometer (range ± 160 m/s^2) and a tri-axial gyroscope (range ± 2000 dps). Before the acquisition, a warm-up period of ten minutes was executed to limit the influence of the temperature on the gyroscope readings. Then, a static acquisition was performed to compute the gyroscope biases. Then, the MIMUs were positioned on the UA and FA of the robot (Figure 48). Each unit was fixed by manually aligning its y-axis with the longitudinal axis of the correspondent robot link. Data were acquired through the Xsens proprietary software MT Manager (v. 4.6) at a sampling frequency of 100 Hz. The robot was positioned in a starting configuration, $\boldsymbol{\varphi}$ = [90 50 -90 0 0 0] and it was programmed to reach the final $\boldsymbol{\varphi}$ = [90 120 -90 150 0 100] at its maximum speed. The robot executed this movement for 20 consecutive minutes (~ 150 cycles). As an example, the time series of the

reference joint kinematics is shown in Figure 50 with dashed lines. It has to be noted that the employed robot axes were coincident to those of the DH model of the upper limb represented in Figure 45.

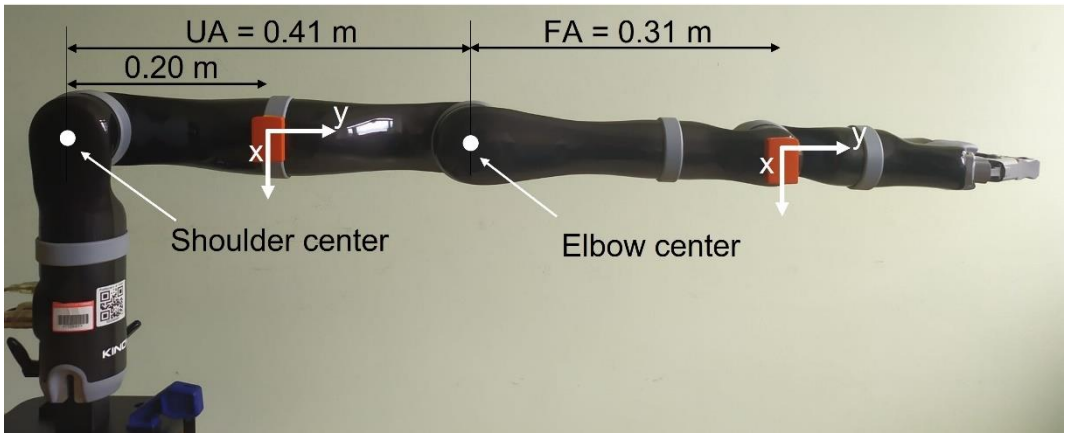

Figure 48: the experimental setup to collect MIMU data during the motion of the collaborative robot. The relevant axes of the MIMUs were aligned to those of the UA and FA and represented in white.

Signal pre-processing and kinematics estimation

- Synthetic data

The orientation of both UA and FA MIMUs was obtained using the MAD filter, separately. Since the parameter value (β) of the SFA plays a central role in determining the accuracy of the estimates (as highlighted in Chapter 3), in this work the orientation was computed using the optimal β value for each MIMU (i.e., the value which minimized the average orientation error with respect to the reference in a grid-search approach). The orientation of the two MIMUs was obtained in the quaternion form and then converted into rotation matrices (to obtain $\hat{R}_{UA}$ and $\hat{R}_{FA}$).

- Robot data

The robot data were resampled at 100 Hz using the recorded timestamp to obtain $\boldsymbol{\varphi}_{ref}$ and then synchronized to MIMU signals through the cross-correlation (Caruso, Sabatini, Laidig, et al., 2021). IMU signals were low-pass filtered (8^{th} order Butterworth, cut-off frequency set to 4 Hz) to remove the high-frequency oscillation due to the robot motor vibrations. Then the bias computed in static was removed from the gyroscope readings. To improve the alignment accuracy

between MIMUs and the robot surface a rotation matrix was computed exploiting the gravity vector (similarly to the procedure described in paragraph "*Developed methods*"). This small rotation was then used to virtually rotate all the measurements. As done for the synthetic signals, the orientation of each unit was obtained using MAD with the corresponding optimal β values and then converted into rotation matrix (to obtain $\hat{R}_{UA}$ and $\hat{R}_{FA}$).

In both synthetic and robot data, the $\hat{R}_{UA}$ and $\hat{R}_{FA}$ matrices were used in the optimization process to obtain the $\boldsymbol{\varphi}_{opt}$ vector. Since the motion was planar, φ_1 and φ_3 were bounded between 90 ± 1 deg, while the others were allowed to span between -5 and 160 deg (but for the carrying angle φ_5 which was set to zero since the robot UA and FA axes are not skewed). Moreover, the maximum angular change between two consecutive time-steps was limited to 2 deg for φ_2 φ_4, and φ_6, and forced to be null for φ_6. Finally, to compare the optimization with the model-free approach, the $\hat{R}_{UA}$ and $\hat{R}_{FA}$were also used to compute the Euler angles (stored in $\boldsymbol{\varphi}_{model-free}$) using the standard sequence proposed by the ISB convention for the shoulder and the elbow (i.e., by applying the unconstrained method).

Error evaluation

For each case, to evaluate the accuracy of the estimates, the following quantities were computed: $\boldsymbol{e}_{opt}$ = RMS($\boldsymbol{\varphi}_{opt} - \boldsymbol{\varphi}_{ref}$) and $\boldsymbol{e}_{model-free}$ = RMS($\boldsymbol{\varphi}_{model-free} - \boldsymbol{\varphi}_{ref}$).

Results

The $\boldsymbol{e}_{opt}$ and $\boldsymbol{e}_{model-free}$ obtained from synthetic and robot data were reported in Table XXI. In addition, the optimal β values for the parameter of MAD amounted to 0.0224 and 0.0005 rad/s for the UA and FA MIMUs during simulated data and to 0.001 and 0.9 rad/s, respectively when using robot data. The trend of the orientation errors when varying β is represented in Figure 49 for both cases together with the corresponding optimal β values. Figure 50 shows the comparison between the optimized time-series of φ_2, φ_4, and φ_6 and the corresponding robot reference kinematics. Figure 51 shows the norm of the residuals of $\boldsymbol{\varphi}_{opt}$ for a given time-step when performing the optimization for the robot data. The average time required by the optimization process to perform a single estimate amounted to 30.5 ms (Intel® Core™ i7-10510U CPU @ 1.80 GHz—Microsoft™ Windows 11).

Table XXI: the joint angle errors obtain with the constrained and unconstrained method for both synthetic and robot data.

	(deg)	φ_1	φ_2	φ_3	φ_4	φ_5	φ_6
synthetic	$\boldsymbol{e}_{opt}$	0.9	3.7	0.9	3.2	0	7.9
	$\boldsymbol{e}_{model-free}$	13.2	3.8	0.1	3.9	16.1	16.2
robot	$\boldsymbol{e}_{opt}$	1.0	0.4	0.9	3.0	0	1.0
	$\boldsymbol{e}_{model-free}$	10.2	0.2	1.4	3.1	8.2	6.0

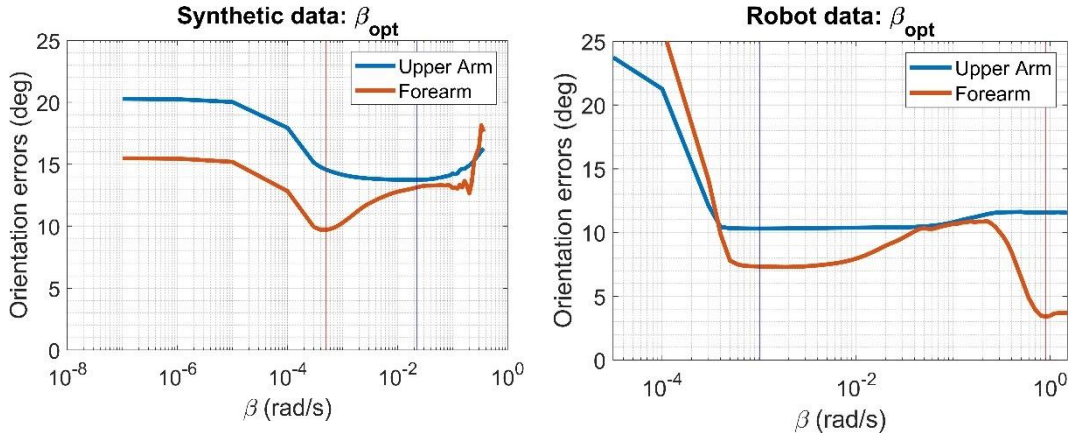

Figure 49: The trend of the orientation errors when varying β together with the optimal β values for UA (blue vertical line) and FA (red vertical line) for both synthetic and robot data.

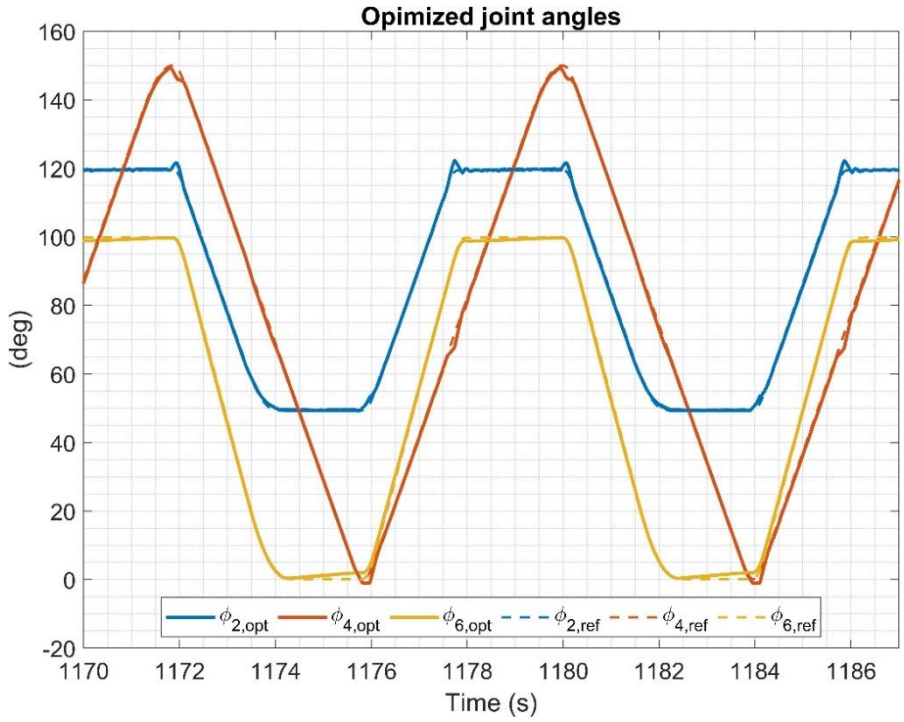

Figure 50: Optimized robot kinematics ($\boldsymbol{\varphi_{opt}}$) vs reference kinematics ($\boldsymbol{\varphi_{ref}}$) for $\boldsymbol{\varphi_2}$, $\boldsymbol{\varphi_4}$, and $\boldsymbol{\varphi_6}$.

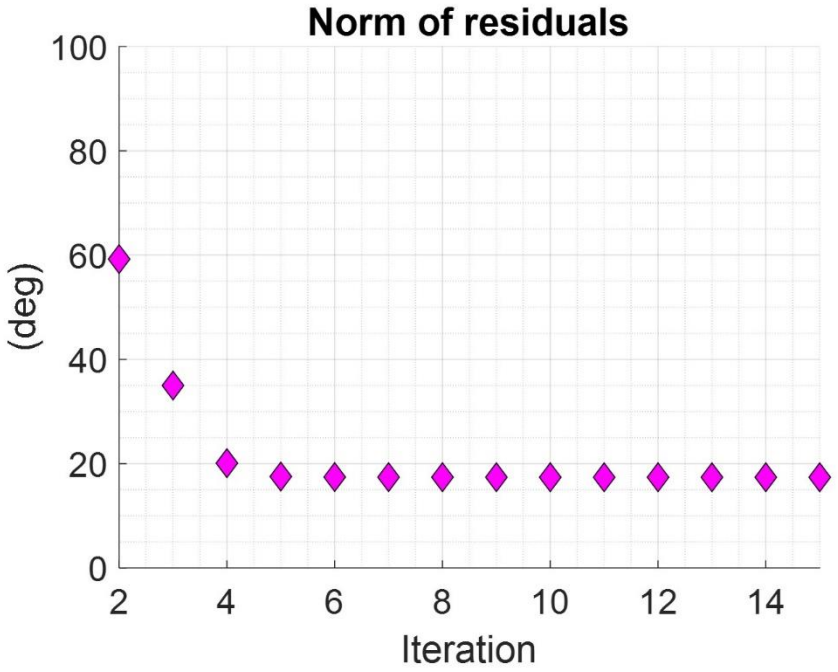

Figure 51: Optimization residuals for a given time-step vs number of iterations (robot data). It is possible to appreciate the non-null values of the residual norm.

Discussion, limitations, and future developments

One of the main critical limitations when estimating the joint kinematics using the low-cost inertial technology over long period consists in the angular drift accumulated as time increases due to the integration of the gyroscope bias residuals. Despite the low values of the latter, the integration over twenty minutes can led to a huge drift, as reported in Table XXI, even if the sensor fusion filter was driven with an optimal parameter value for each MIMU in both cases. It is also interesting to observe that different types of motion require to set different optimal parameter values, in line with (Caruso, Sabatini, Knaflitz, et al., 2021; Caruso, Sabatini, Laidig, et al., 2021; Laidig et al., 2021), as shown in Figure 49. When the joint angles were computed with the model-free approach ($\boldsymbol{e}_{model-free}$), the errors amounted to very large values, especially for the φ_i estimated when MIMU axes were orientated along the vertical direction during the motion. During this situation the drift cannot be compensated for by exploiting the gravity direction. In this work, a DH model of the upper limb was defined to express the joint angle accordingly to the ISB guidelines and to allow the definition of the proper biomechanical constraints. Since the characteristics of motion in terms of speed and range were known *a-priori*, it was possible to

introduce these limits in the optimization framework thus leading to lower RMS joint angle errors: 2.8 vs 8.9 deg for synthetic data and 1.1 vs 8.9 deg for robot data, respectively, on average. In addition, φ_2, φ_4, and φ_6, errors related to the robot data were in general slightly lower when compared to the synthetic ones, since the simulation was thought to be more challenging in terms of speed and intensity than the motion characteristics achievable with the robot, due to the technical limitations of the latter. In fact, a higher motion intensity results in higher acceleration values corrupting the gravity direction estimation. Finally, it must be acknowledged that the proposed optimization framework could not be completely effective in reducing the drift for φ_2, φ_4, and φ_6 as they spanned a large range of motion. However, contrary to the model-free approach, the proposed method offers the possibility to limit variations between two consecutive time steps within reasonable values, thus mitigating the sensor fusion errors. it has to be stressed that the lower errors obtained using the proposed approach are due to the *a-priori* knowledge of the motion which allowed to separate the errors from the joint angles and to increase the residual which does not reach zero (as shown in Figure 51). In other words, the *a-priori* knowledge of the performed motion allowed to constraint the model despite the errors affecting the measurements. To sum up, the higher the *a-priori* knowledge, the higher the optimization accuracy. Current efforts are devoted to exploit the complementary information carried by the linear accelerations and the angular velocities. Indeed, the minimization of multiple objective functions derived from measurements with different source of errors may improve the compensation of the drift, as done for the RCM method described in Chapter 3.

References

al Borno, M., O'Day, J., Ibarra, V., Dunne, J., Seth, A., Habib, A., Ong, C., Hicks, J., Uhlrich, S., & Delp, S. (2022). OpenSense: An open-source toolbox for inertial-measurement-unit-based measurement of lower extremity kinematics over long durations. *Journal of NeuroEngineering and Rehabilitation*, *19*(1), 1–11. https://doi.org/10.1186/S12984-022-01001-X/FIGURES/4

Aziz, A. F. A., Aziz, N. A., Mohd Nordin, N. A., Ali, M., Sulong, S., & Aljunid, S. (2013). What is next after transfer of care from hospital to home for stroke patients? Evaluation of a community stroke care service based in a primary care clinic. *Journal of Neurosciences in Rural Practice*, *4*(4), 413–420. https://doi.org/10.4103/0976-3147.120243

Balta, D., Salvi, M., Molinari, F., Figari, G., Paolini, G., della Croce, U., & Cereatti, A. (2020). A two-dimensional clinical gait analysis protocol based on markerless recordings from a single RGB-Depth camera. *2020 IEEE International Symposium on Medical Measurements and Applications (MeMeA)*, 1–6. https://doi.org/10.1109/MeMeA49120.2020.9137183

Begon, M., Andersen, M. S., & Dumas, R. (2018). Multibody Kinematics Optimization for the Estimation of Upper and Lower Limb Human Joint Kinematics: A Systematized Methodological Review. *Journal of Biomechanical Engineering*, *140*(3), 1–11. https://doi.org/10.1115/1.4038741

Bertomeu-Motos, A., Lledó, L. D., Díez, J. A., Catalan, J. M., Ezquerro, S., Badesa, F. J., & Garcia-Aracil, N. (2015). Estimation of human arm joints using two wireless sensors in robotic rehabilitation tasks. *Sensors (Switzerland)*, *15*(12), 30571–30583. https://doi.org/10.3390/s151229818

Bonato, P. (2003). Wearable Sensors/Systems and Their Impact on Biomedical Engineering. *IEEE Engineering in Medicine and Biology Magazine*, *22*(3), 18–20. https://doi.org/10.1109/MEMB.2003.1213622

Bouvier, B., Duprey, S., Claudon, L., Dumas, R., & Savescu, A. (2015). Upper limb kinematics using inertial and magnetic sensors: Comparison of sensor-to-segment calibrations. *Sensors (Switzerland)*, *15*(8), 18813–18833. https://doi.org/10.3390/s150818813

Brogårdh, C., & Sjölund, B. H. (2006). Constraint-induced movement therapy in patients with stroke: A pilot study on effects of small group training and of extended miit use. *Clinical Rehabilitation*, *20*(3), 218–227. https://doi.org/10.1191/0269215506cr937oa

Caruso, M., Sabatini, A. M., Knaflitz, M., della Croce, U., & Cereatti, A. (2021). Extension of the Rigid-Constraint Method for the Heuristic Suboptimal Parameter Tuning to Ten

Sensor Fusion Algorithms Using Inertial and Magnetic Sensing. *Sensors*, *21*(18), 6307. https://doi.org/10.3390/s21186307

Caruso, M., Sabatini, A. M., Laidig, D., Seel, T., Knaflitz, M., della Croce, U., & Cereatti, A. (2021). Analysis of the Accuracy of Ten Algorithms for Orientation Estimation Using Inertial and Magnetic Sensing under Optimal Conditions: One Size Does Not Fit All. *Sensors*, *21*(7), 2543. https://doi.org/10.3390/s21072543

Cereatti, A., della Croce, U., & Sabatini, A. M. (2017). Three-Dimensional Human Kinematic Estimation Using Magneto-Inertial Measurement Units. In B. Müller, S. I. Wolf, G.-P. Brueggemann, Z. Deng, A. McIntosh, F. Miller, & W. S. Selbie (Eds.), *Handbook of Human Motion* (pp. 1–24). Springer International Publishing. https://doi.org/10.1007/978-3-319-30808-1_162-1

Cereatti, A., Trojaniello, D., & Croce, U. della. (2015). Accurately measuring human movement using magneto-inertial sensors: Techniques and challenges. *2nd IEEE International Symposium on Inertial Sensors and Systems, IEEE ISISS 2015 - Proceedings*, 1–4. https://doi.org/10.1109/ISISS.2015.7102390

Coleman, T. F., & Li, Y. (2006). An Interior Trust Region Approach for Nonlinear Minimization Subject to Bounds. *Http://Dx.Doi.Org/10.1137/0806023*, *6*(2), 418–445. https://doi.org/10.1137/0806023

Cornagliotto, V., Digo, E., & Pastorelli, S. (2021). Using a Robot Calibration Approach Toward Fitting a Human Arm Model. *Mechanisms and Machine Science*, *102*, 199–207. https://doi.org/10.1007/978-3-030-75259-0_22

Cottam, D. S., Campbell, A. C., Davey, P. C., Kent, P., Elliott, B. C., & Alderson, J. A. (2021). Functional calibration does not improve the concurrent validity of magneto-inertial wearable sensor-based thorax and lumbar angle measurements when compared with retro-reflective motion capture. *Medical and Biological Engineering and Computing*, *59*(11–12), 2253–2262. https://doi.org/10.1007/S11517-021-02440-9/FIGURES/3

Cutti, A. G., Ferrari, A., Garofalo, P., Raggi, M., Cappello, A., & Ferrari, A. (2010). "Outwalk": A protocol for clinical gait analysis based on inertial and magnetic sensors. *Medical and Biological Engineering and Computing*, *48*(1), 17–25. https://doi.org/10.1007/S11517-009-0545-X/TABLES/2

Cutti, A. G., Giovanardi, A., Rocchi, L., Davalli, A., & Sacchetti, R. (2008). Ambulatory measurement of shoulder and elbow kinematics through inertial and magnetic sensors. *Medical and Biological Engineering and Computing*, *46*(2), 169–178. https://doi.org/10.1007/s11517-007-0296-5

Davis, R. B., Õunpuu, S., Tyburski, D., & Gage, J. R. (1991). A gait analysis data collection and reduction technique. *Human Movement Science*, *10*(5), 575–587. https://doi.org/10.1016/0167-9457(91)90046-Z

Delp, S. L., Anderson, F. C., Arnold, A. S., Loan, P., Habib, A., John, C. T., Guendelman, E., & Thelen, D. G. (2007). OpenSim: Open-source software to create and analyze dynamic simulations of movement. *IEEE Transactions on Biomedical Engineering*, *54*(11), 1940–1950. https://doi.org/10.1109/TBME.2007.901024

El-Gohary, M., & McNames, J. (2012). Shoulder and elbow joint angle tracking with inertial sensors. *IEEE Transactions on Biomedical Engineering*, *59*(9), 2635–2641. https://doi.org/10.1109/TBME.2012.2208750

Harari, O. A., & Liao, J. K. (2010). NF-κB and innate immunity in ischemic stroke. In *Annals of the New York Academy of Sciences* (Vol. 1207, pp. 32–40). https://doi.org/10.1111/j.1749-6632.2010.05735.x

Laidig, D., Caruso, M., Cereatti, A., & Seel, T. (2021). BROAD—A Benchmark for Robust Inertial Orientation Estimation. *Data*, *6*(7). https://doi.org/10.3390/data6070072

Leardini, A., Chiari, A., della Croce, U., & Cappozzo, A. (2005). Human movement analysis using stereophotogrammetry: Part 3. Soft tissue artifact assessment and compensation. *Gait & Posture*, *21*(2), 212–225. https://doi.org/10.1016/J.GAITPOST.2004.05.002

Levin, M. F., Kleim, J. A., & Wolf, S. L. (2009). What do motor "recovery" and "compensationg" mean in patients following stroke? *Neurorehabilitation and Neural Repair*, *23*(4), 313–319. https://doi.org/10.1177/1545968308328727

Lynch, E. A., Cadilhac, D. A., Luker, J. A., & Hillier, S. L. (2017). Inequities in access to inpatient rehabilitation after stroke: An international scoping review. *Topics in Stroke Rehabilitation*, *24*(8), 619–626. https://doi.org/10.1080/10749357.2017.1366010

Macis, S., Loi, D., Pani, D., Rijnen, W., & Raffo, L. (2015). A TV-based ICT platform for active ageing, tele-care and social networking. *ICT4AgeingWell 2015 - Proceedings of the 1st International Conference on Information and Communication Technologies for Ageing Well and e-Health*, 219–227. https://doi.org/10.5220/0005448802190227

Maclean, N., Pound, P., Wolfe, C., & Rudd, A. (2000). Qualitative analysis of stroke patients' motivation for rehabilitation. *BMJ (Clinical Research Ed.)*, *321*(7268), 1051–1054. https://doi.org/10.1136/bmj.321.7268.1051

McGinley, J. L., Baker, R., Wolfe, R., & Morris, M. E. (2009). The reliability of three-dimensional kinematic gait measurements: a systematic review. *Gait & Posture*, *29*(3), 360–369. https://doi.org/10.1016/J.GAITPOST.2008.09.003

Pani, D., & Cereatti, A. (n.d.). *DoMoMEA project*. http://sites.unica.it/domomea-project/

Parasuraman, S., Kee, C. Y., & Oyong, A. (2009). Human upper limb and arm kinematics for robot based rehabilitation. *IEEE/ASME International Conference on Advanced Intelligent Mechatronics, AIM*, 845–850. https://doi.org/10.1109/AIM.2009.5229906

Peters, A., Galna, B., Sangeux, M., Morris, M., & Baker, R. (2010). Quantification of soft tissue artifact in lower limb human motion analysis: A systematic review. *Gait & Posture*, *31*(1), 1–8. https://doi.org/10.1016/J.GAITPOST.2009.09.004

Picerno, P., Caliandro, P., Iacovelli, C., Simbolotti, C., Crabolu, M., Pani, D., Vannozzi, G., Reale, G., Rossini, P. M., Padua, L., & Cereatti, A. (2019). Upper limb joint kinematics using wearable magnetic and inertial measurement units: an anatomical calibration procedure based on bony landmark identification. *Scientific Reports*, *9*(1), 1–10. https://doi.org/10.1038/s41598-019-50759-z

Picerno, P., Cereatti, A., & Cappozzo, A. (2008). Joint kinematics estimate using wearable inertial and magnetic sensing modules. *Gait and Posture*, *28*(4), 588–595. https://doi.org/10.1016/j.gaitpost.2008.04.003

Rahman, M. H., Ouimet, T. K., Saad, M., Kenné, J. P., & Archambault, P. S. (2010). Development and control of a wearable robot for rehabilitation of elbow and shoulder joint movements. *IECON Proceedings (Industrial Electronics Conference)*, 1506–1511. https://doi.org/10.1109/IECON.2010.5675459

Roetenberg, D., Luinge, H., & Slycke, P. (2009). Xsens MVN: full 6DOF human motion tracking using miniature inertial sensors. *Xsens Motion Technologies BV, …*, 1–7. http://www.xsens.com/images/stories/PDF/MVN_white_paper.pdf

Roetenberg, D., Luinge, H., & Veltink, P. (2003). Inertial and magnetic sensing of human movement near ferromagnetic materials. *Proceedings - 2nd IEEE and ACM International Symposium on Mixed and Augmented Reality, ISMAR 2003*, 268–269. https://doi.org/10.1109/ISMAR.2003.1240714

Seel, T., Raisch, J., Schauer, T., Seel, T., Raisch, J., & Schauer, T. (2014). IMU-Based Joint Angle Measurement for Gait Analysis. *Sensors*, *14*(4), 6891–6909. https://doi.org/10.3390/s140406891

Siciliano, B., & Khatib, O. (2009). Springer handbook of robotics. In *Choice Reviews Online* (Vol. 46, Issue 06). Springer. https://doi.org/10.5860/CHOICE.46-3272

Siciliano, B., Sciavicco, L., Villani, L., & Oriolo, G. (2009). *Robotics*. https://doi.org/10.1007/978-1-84628-642-1

Tagliapietra, L., Modenese, L., Ceseracciu, E., Mazzà, C., & Reggiani, M. (2018). Validation of a model-based inverse kinematics approach based on wearable inertial sensors. *Computer Methods in Biomechanics and Biomedical Engineering*, *21*(16), 834–844. https://doi.org/10.1080/10255842.2018.1522532

Winters, J. M. (2002). Telerehabilitation research: Emerging opportunities. *Annual Review of Biomedical Engineering*, *4*, 287–320. https://doi.org/10.1146/annurev.bioeng.4.112801.121923

Wu, G., Siegler, S., Allard, P., Kirtley, C., Leardini, A., Rosenbaum, D., Whittle, M., D'Lima, D. D., Cristofolini, L., Witte, H., Schmid, O., & Stokes, I. (2002). ISB recommendation on definitions of joint coordinate system of various joints for the reporting of human joint motion—part I: ankle, hip, and spine. *Journal of Biomechanics*, *35*(4), 543–548. https://doi.org/10.1016/S0021-9290(01)00222-6

Wu, G., van der Helm, F. C. T., Veeger, H. E. J., Makhsous, M., van Roy, P., Anglin, C., Nagels, J., Karduna, A. R., McQuade, K., Wang, X., Werner, F. W., & Buchholz, B. (2005). ISB recommendation on definitions of joint coordinate systems of various joints for the reporting of human joint motion - Part II: Shoulder, elbow, wrist and hand. *Journal of Biomechanics*, *38*(5), 981–992. https://doi.org/10.1016/j.jbiomech.2004.05.042

Yang, J., Feng, X., Kim, J. H., Xiang, Y., & Rajulu, S. (2009). Joint Coupling for Human Shoulder Complex. *Lecture Notes in Computer Science (Including Subseries Lecture Notes in Artificial Intelligence and Lecture Notes in Bioinformatics)*, *5620 LNCS*, 72–81. https://doi.org/10.1007/978-3-642-02809-0_9

Zanchettin, A. M., Rocco, P., Bascetta, L., Symeonidis, I., & Peldschus, S. (2011). Kinematic analysis and synthesis of the human arm motion during a manipulation task. *Proceedings - IEEE International Conference on Robotics and Automation*, 2692–2697. https://doi.org/10.1109/ICRA.2011.5979654

Zedda, A., Gusai, E., Caruso, M., Bertuletti, S., Baldazzi, G., Spanu, S., Riboni, D., Pibiri, A., Monticone, M., Cereatti, A., & Pani, D. (2020). DoMoMEA: A Home-Based Telerehabilitation System for Stroke Patients. *Proceedings of the Annual International Conference of the IEEE Engineering in Medicine and Biology Society, EMBS*, *2020-July*, 5773–5776. https://doi.org/10.1109/EMBC44109.2020.9175742

Chapter 5

Conclusions and “good practice guidelines”

General conclusions

The aim of this thesis was to propose the methods and to provide the guidelines to accurately estimate the human joint kinematics starting from the accelerometer, the gyroscope, and the magnetometer signals of the Magneto-Inertial Measurement Units. As highlighted by the second chapter, a comprehensive battery of tests was needed to completely characterize the sources of errors affecting the quality of the MIMU measurements. These tests were particularly useful to spot non-working devices and to understand whether a sensor should undergo a refinement of the calibration coefficients through the definition of nine parameters. Since till today there are no recognized acceptability values to distinguish between a well calibrated sensor and an uncalibrated one, researchers should define the threshold values of each test based on the specific application under analysis. It is worth highlighting that these tests do not require specialized laboratories and can be conducted using simple equipment.

The third chapter was mainly focused on the methods to accurately estimate the orientation of each MIMU starting from its measurements combined by means of sensor fusion algorithms. Since each SFA exposes a certain number of parameters whose values need to be properly set to obtain an accurate orientation

estimate, to perform a "fair" comparison among the performance of different SFAs it was central to put all of them under the same optimal working conditions. It was observed, in accordance with previous studies, that that the selection of the value of each parameter is crucial to obtain a satisfying performance of a generic SFA, despite its filtering class or mathematical formulation. On the contrary, the use of fixed parameter values may be not suitable for every scenario since, in general, the optimal value regions did not intersect. The most important finding was that all the errors fall within a range from 3.8 deg to 7.1 deg thus making it impossible to rank the ten implemented SFAs. In other words, it was not possible to draw any conclusions about the best performing SFA since no statistically significant differences were found. In addition, the orientation accuracy was heavily influenced by the experimental variables such as the kinematics parameters and the specific MIMU models selected to perform the acquisitions. To the best of authors' knowledge, this study performed the most extensive comparison (10 SFAs × 3 motion intensities × 3 commercial products). However, additional aspects should be considered when evaluating the accuracy of SFAs, such as the effect of translations, long uninterrupted motion phases, and the influence of magnetic disturbances. Recently, a dataset including 39 different experimental scenarios was made available. Four algorithms among those implemented in this study were considered and the preliminary results confirmed the findings reported in this thesis. After that, since the optimal approach cannot be suitable from the perspective of an unconstrained motion monitoring, a novel method to estimate the most suitable parameter values for a given SFA without relying on any orientation reference was designed. The proposed "rigid-constraint" approach exploited the hypothesis that a set of aligned MIMUs has a null and constant relative orientation over time. The RCM is based on the difference of the sources of errors and disturbances which affect the relevant sensors of the two different MIMUs. The validity of the RCM was tested on the ten SFAs with encouraging results, since the maximum residual between the optimal error and the error obtained using the estimated suboptimal parameter values amounted to 3.7 deg and to 0.6 deg on average. The findings of the current study move in the direction of the unconstrained assessment of the subjects' motor capacity which, for example, can be performed by means of tele-rehabilitation systems at patients' home where the joint kinematics is monitored in absence of the ground-truth orientation.

In the fourth chapter, two methods for estimating the joint kinematics starting from the MIMU orientation were proposed and analyzed. Both were designed to

work without exploiting the magnetometer contribution being the latter too prone to the ferromagnetic disturbances. The first method, called unconstrained, relies on the *a-priori* knowledge of the MIMU positioning on the human segments to get around the problem of the lack of knowledge about the MIMU relative orientation on the horizontal plane. The unconstrained method is simple being based on the traditional Euler inversion of the relative orientation and can provide accurate joint angle estimates in real time. However, the author suggests employing the unconstrained joint kinematics for short time only since this approach has no way to mitigate the drift error around the vertical axis because the information about the Earth's magnetic north direction is missing. To overcome this limitation, a more complex method, called constrained, was developed by designing a biomechanical model of the upper limb based on the Denavit-Hartenberg robotic convention. The idea was to minimize the difference between the MIMU-based segment orientation and the one predicted by the model in an optimization framework. In addition, reasonable physiological constraints were defined based on the *a-priori* knowledge of the task under analysis in terms of maximum angular variations between two consecutive time-steps and maximum amplitude. This allowed to contain the drift errors within 3 deg at most for a recording of twenty minutes length of a continuous robot motion (the corresponding errors obtained with the unconstrained method were higher than 10 deg). Despite more accurate it must be considered that the processing time required by the constrained method is limited by the optimization speed which in turn depends on how far the estimate is from the minimum point. At the current stage, the average time required to perform a single optimization update is not suitable to work at a frequency higher than 30 Hz thus constituting an upper limit for the exercise velocity execution. However, such a limit does not represent a criticism for home based telerehabilitation applications in which the typical gesture does not involve fast movements. The obtained joint angular errors suggest the feasibility of employing these solutions in the rehabilitation programs to properly plan the treatment and to accurately evaluate the outcomes.

To conclude, the contribution of this thesis was conceived to enable an accurate estimation of the human joint kinematics in the patients' ecological environments with a view towards the main goal of facilitating the transition from the lab-based analysis to the free-living conditions monitoring.

Good practice guidelines

As pointed out by the title, this thesis would like to propose some guidelines to researchers facing the same practical issues of the daily use of the inertial sensors to estimate the orientation and the kinematics of the human joints. In particular, the main suggestions are reported for each level of the bottom-up approach followed by this thesis.

Calibration and characterization of the MIMU signals

In general, as the performances of low-cost sensors may deteriorate over time, a refinement of the accelerometer, gyroscope, and magnetometer calibration coefficients is necessary when using a new of factory MIMU to allow both the acquisition of good quality measurements and to ensure results comparability among different studies. This is particularly useful when sensor signals are integrated to compute quantitative information to prevent measurement errors from accumulating over time. In this perspective, a considerable number of algorithms have been proposed and the majority of them rely on the accurate alignment of the sensor axes along the vertical direction. However, most of the MIMUs available on the market have rounded surfaces not suitable for this purpose. In this case, it is important to develop and use additional devices which may help in this direction.

From the perspective of estimating the MIMU orientation, the calibration refinement of the accelerometer mainly acts to compensate for misalignment and non-orthogonality of the sensor axes. Then, it is no longer necessary to repeat this refinement frequently unless some huge mechanical shocks are experienced by the sensor which may skew the sensor axes and change their relative orientation with respect to the axes of the housing. On the contrary, this does not apply to the gyroscope for which changes in the angular velocity bias are very common (run-to-run variation) depending on the sensor electronics and the temperature. It is thus fundamental to acquire the gyroscope bias and remove its value from the gyroscope readings before running any sensor fusion algorithms for which the integration of the angular velocity represents the main step. To this end, after a warm-up of the MIMUs for a few minutes, a short static acquisition of 60-120 seconds should be recorded. Furthermore, the magnetometer represents a fundamental added value to compensate for the orientation drift along the vertical direction and it is not influenced by the motion intensity as it happens for the accelerometer. However, based on my personal experience, the magnetometer

calibration is the most instable in time and should be repeated very often, going against the practicality of the MIMU. It is then advisable to test and characterize the magnetometer in absence of ferromagnetic disturbances by performing simple experiments to verify the compliance of the signals with the hypotheses and thus determine their reliability.

Finally, the characterization of the MIMU signals may be helpful on one hand to know the sensor noise level and to develop models to be integrated, for example, within a sensor fusion framework. On the other hand, the knowledge of the strength of the sensor deterministic errors allows to monitor their performance and understand when an additional calibration refinement is required to ensure the best performance achievable with this technology.

Sensor fusion algorithms for orientation estimation

After having verified the quality of the magnetic and inertial signals, the next step to compute the joint kinematics is the estimation of the MIMU orientation. Several sensor fusion algorithms have been designed over the decades but there are no practical guidelines available to select the most suitable one for a specific purpose. A first selection could be based on the execution time which differs between the SFAs. In fact, for some applications the “real time” represents a fundamental requirement (e.g., telerehabilitation) and a fast SFA should be employed. After that, to compare the accuracy of the orientation estimates among the different SFAs, it is necessary to put them under the same working conditions. This could be only ensured by selecting the proper parameter values. When available, the gold standard orientation could be exploited to find the optimal parameter values according to the specific experimental scenario under analysis, since it has been demonstrated that motion intensities and the commercial products have a strong influence on the orientation errors. If, after the comparison, no substantial differences emerged between the accuracy of the SFAs, the advice is to select the simplest filter in terms of number of parameters. Regardless of the specific SFA selected, as already said, it is necessary to remove the gyroscope bias using an acquisition recorded just before the actual experiments. Then, the initial conditions should be provided using a gyro-free approach (i.e., using only the accelerometer and the magnetometer) to drastically reduce the convergence time.

As anticipated, the choice of the most suitable parameter values is still an open issue, especially when the gold standard orientation is not available, which is

expected since the MIMUs are intended to be used under unsupervised conditions outside the laboratory. At the moment, to the best of my knowledge, there are no methods to select these values using a single MIMU in absence of the orientation reference. In this work, the rigid-constraint method was proposed to estimate the parameter values using two MIMUs attached to the same rigid body. The method has proved to be effective although it requires one additional MIMUs and space. Alternatively, if only one MIMU is available, one can estimate the optimal parameter values using the orientation reference trying to replicate the same experimental conditions (in terms of motion intensity and the specific commercial product) during a preliminary acquisition and to use the same values on the actual experiments. In any case, it is advisable to gain confidence and experience with the selected SFA in order to know which parameter values allow its best performance.

One final consideration consists in the use of the magnetometer to estimate the orientation which allows to compensate for the gyroscope drift, especially along the vertical axis. The orientation estimated this way is more robust and in absence of ferromagnetic disturbances could be very accurate since it benefits from the complementary information of the three sensors. However, for some indoor applications (such as telerehabilitation), the ferromagnetic disturbances may strongly jeopardize the orientation accuracy thus compromising the usability of the MIMUs. In this case, avoiding the magnetometer could represent a reasonable choice despite loosing the reference on the horizontal plane, as detailed in Chapter 4.

Joint kinematics estimation using inertial sensing

The estimation of the joint kinematics requires different choices in terms of both sensor-to-segment alignment methods and approaches to combine the orientation recorded by the MIMUs.

Regarding the sensor-to-segment alignment, a first choice is the approach to express the relative orientation difference between the axes of the MIMUs and those of the anatomical segments which, in general, are not coincident. Some solutions are available in the literature including the functional movement and the manual positioning. The former requires the subject to perform pure movements around the anatomical axis/axes of interest. This solution is time consuming and has been proven to be effective only with the supervision of an expert operator, which is not the case of home-based applications. For these reasons, the manual

alignment may be preferred due to its simplicity. Additional equipment, such as housing and straps, could be involved to help the subjects with the alignment of the MIMUs along the relevant anatomical axes. Moreover, simple static standing postures can be exploited to perform a virtual realignment of the MIMU axes with the vertical direction. This is particularly useful for those segments whose longitudinal axis is aligned along the gravity during the standing position (e.g., trunk and pelvis). Finally, when the orientation is estimated in absence of the magnetic field reference, it is advisable to position the proximal and distal MIMUs with a known initial configuration to make up for the unknown relative orientation on the horizontal plane.

Two approaches are available to compute the joint angles. The first, referred as "model-free", does not rely on any model and constraints. The model-free approach computes the joint angles as the relative orientation difference between the orientation of the proximal and distal MIMUs to the joint of interest. The relative orientation is then decomposed using a proper Euler sequence. However, any orientation errors due to the SFAs would be completely reflected on the final joint angles which may be no longer compatible with the functional anatomy and the physiological joint constraints. On the other hand, this approach is very fast from a computational point of view and very simple to implement. The suggestion is to use the model-free only when the joint kinematics is computed for a very few minutes so as not to accumulate the orientation errors. In addition, it would be beneficial to split the acquisitions into different recordings rather than acquiring all the trials in a unique one. This allows to reset the orientation errors each time a new recording is started. The second approach, referred as "model-based", is useful to set appropriate constraints on the joint angles, operation suitable when computing the joint kinematics for longer time (e.g., tens of minutes). In this work, the constraints were set based on both the physiological limits of the human joints and the *a-priori* knowledge of the performed motion. The model-based approach could be implemented within an optimization framework to obtain robust joint angle solutions. The main drawback may be represented by the higher computational time compared to that of the model-free. Finally, in accordance with the literature, to obtain clinically meaningful values, it is necessary to express the joint angles using a proper Euler sequence compliant with the International Society of Biomechanics suggestions, regardless of the specific approach employed. This would make it also possible a comparison among the results obtained from different studies.

As a final consideration, the adoption of shared guidelines could simplify and improve the harmonization of the results produced by the different research group and the movement analysis community should move in this direction.

List of publications

Peer-review paper

Caruso, M.; Sabatini, A.M.; Knaflitz, M.; Gazzoni, M.; Croce, U.D; Cereatti, A. Orientation Estimation through Magneto-Inertial Sensor Fusion: A Heuristic Approach for Suboptimal Parameters Tuning. *IEEE Sens. J.* **2021**, *21*, 3408–3419, doi:10.1109/JSEN.2020.3024806.

Caruso, M.; Sabatini, A.M.; Laidig, D.; Seel, T.; Knaflitz, M.; Della Croce, U.; Cereatti, A. Analysis of the Accuracy of Ten Algorithms for Orientation Estimation Using Inertial and Magnetic Sensing under Optimal Conditions: One Size Does Not Fit All. *Sensors* **2021**, *21*, 2543, doi:10.3390/s21072543.

Laidig, D.; **Caruso**, M.; Cereatti, A.; Seel, T. BROAD—A Benchmark for Robust Inertial Orientation Estimation. *Data* **2021**, *6*, 72, doi:10.3390/data6070072.

M. **Caruso**, A. M. Sabatini, M. Knaflitz, U. Della Croce, and A. Cereatti, "Extension of the Rigid-Constraint Method for the Heuristic Suboptimal Parameter Tuning to Ten Sensor Fusion Algorithms Using Inertial and Magnetic Sensing," *Sensors*, vol. 21, no. 18, p. 6307, Sep. 2021 [Online]. Available: http://dx.doi.org/10.3390/s21186307

Mazzà C, Alcock L, Aminian K, ***et al*** Technical validation of real-world monitoring of gait: a multicentric observational study *BMJ Open* 2021;**11:**e050785. doi: 10.1136/bmjopen-2021-050785

Bonci, T., Salis, F., Scott, K., Alcock, L., Becker, C., Bertuletti, S., Buckley, E., **Caruso, M**., Cereatti A., Din, S. del, Gazit, E., Hansen, C., Hausdorff, J. M., Maetzler, W., Palmerini, L., Rochester, L., Schwickert, L., Sharrack, B., Vogiatzis, I., & Mazza, C. (1 C.E.). An algorithm for accurate marker-based gait event detection in healthy and pathological populations during complex motor tasks. *Frontiers in Bioengineering and Biotechnology*, *0*, 754. https://doi.org/10.3389/FBIOE.2022.868928 (*in press*)

Conference Proceedings published on International Journals (indexed in Scopus)

Digo, E., Gastaldi, L., Antonelli, M., Pastorelli, S., Cereatti, A., & **Caruso, M**. (2022). Real-time estimation of upper limbs kinematics with IMUs during typical industrial gestures. *Procedia Computer Science*, *200*, 1041–1047. https://doi.org/10.1016/J.PROCS.2022.01.303

A. Zedda **et al**., "DoMoMEA: a Home-Based Telerehabilitation System for Stroke Patients," 2020 42nd Annual International Conference of the IEEE Engineering in Medicine & Biology Society (EMBC), 2020, pp. 5773-5776, doi: 10.1109/EMBC44109.2020.9175742.

M. **Caruso**, A. M. Sabatini, M. Knaflitz, M. Gazzoni, U. D. Croce and A. Cereatti, "Accuracy of the Orientation Estimate Obtained Using Four Sensor Fusion Filters Applied to Recordings of Magneto-Inertial Sensors Moving at Three Rotation Rates," 2019 41st Annual International Conference of the IEEE Engineering in Medicine and Biology Society (EMBC), 2019, pp. 2053-2058, doi: 10.1109/EMBC.2019.8857655.

R. Rossanigo, M. **Caruso**, F. Salis, S. Bertuletti, U. D. Croce and A. Cereatti, "An Optimal Procedure for Stride Length Estimation Using Foot-Mounted Magneto-Inertial Measurement Units," 2021 IEEE International Symposium on Medical Measurements and Applications (MeMeA), 2021, pp. 1-6, doi: 10.1109/MeMeA52024.2021.9478604.

F. Salis **et al**., "A wearable multi-sensor system for real world gait analysis," 2021 43rd Annual International Conference of the IEEE Engineering in Medicine & Biology Society (EMBC), 2021, pp. 7020-7023, doi: 10.1109/EMBC46164.2021.9630392.

Pending proceedings to be published on International Journals (indexed in Scopus)

M. Caruso, L. Gastaldi, S. Pastorelli, A. Cereatti, and E. Digo "An ISB-consistent Denavit-Hartenberg model of the human upper limb for joint kinematics optimization: validation on synthetic and robot data during a typical rehabilitation gesture" 2022 44th Annual International Conference of the IEEE Engineering in Medicine & Biology Society (EMBC), 2022

R. Nicola, G.L. Cerone, **M. Caruso**, R. Rossanigo, A. Cereatti, and T. Vieira "On the Detection of High-Quality, High-Density Electromyograms During 80m Sprints: a Case Study" to 2022 IEEE International Symposium on Medical Measurements and Applications (MeMeA)

M. **Caruso**, D. Laidig, A.M. Sabatini, M. Knaflitz, U. Della Croce, T. Seel, and A. Cereatti "Comparison of the performances of six magneto-inertial sensor fusion filters for orientation estimation in movement analysis". In *Proceedings of Seventh National Congress of Bioengineering (GNB)*, Trieste 2020.

R. Rossanigo, S. Bertuletti, M. **Caruso**, M. Knaflitz, U. Della Croce and A. Cereatti "Estimation of the base of support during gait with an unobtrusive wearable system". In *Proceedings of Seventh National Congress of Bioengineering (GNB)*, Trieste 2020.

F. Salis, S. Bertuletti, M. **Caruso**, T. Bonci, K. Scott, R. Rossanigo, U. Della Croce, C. Mazzà and A. Cereatti "A novel multi-sensor system for gait assessment in real-world conditions: preliminary results". In *Proceedings of Seventh National Congress of Bioengineering (GNB)*, Trieste 2020.

A. Zedda, E. Gusai, M. **Caruso**, S. Bertuletti, S. Spanu, G. Baldazzi, K. Masciavé, A. Pibiri, M. Monticone, A.Cereatti, L. Raffo and D. Pani "DoMoMEA: a home neuromotor telerehabilitation system for stroke patients". In *Proceedings of Seventh National Congress of Bioengineering (GNB)*, Trieste 2020.

Conference Proceedings (not indexed in Scopus)

M. **Caruso**, A. Zedda, E. Gusai, S. Bertuletti, S. Spanu, A. Pibiri, M. Monticone, D. Pani and A. Cereatti "Real-time joint kinematics estimation in tele-rehabilitation". In *Proceedings of XXVIII Congress of the International Society of Biomechanics (ISB2019)*, Stockholm 2021.

M. **Caruso**, A. Sabatini, V. Camomilla, M. Knaflitz, M. Gazzoni, U. Della Croce, A. Cereatti: "Investigation on the accuracy of five sensor fusion algorithms for orientation estimation". In *Proceedings of 3-D Analysis of Human Movement (3Dahm)*, Ames 2021.

M. **Caruso**, R. Rossanigo, A. M. Sabatini, M. Knaflitz, M. Gazzoni, U. Della Croce, A. Cereatti "Towards an automatic parameter setting for MIMU sensor fusion algorithms". In: Proceedings of XX Annual Congress of the Italian Society for analysis of movement in the clinic (SIAMOC 2019), Bologna 2019. https://doi.org/10.1016/j.gaitpost.2019.07.453

F. Salis, S. Bertuletti, M. **Caruso**, U. Della Croce, C. Mazzà, A. Cereatti "Multi-sensor integration and data fusion for enhancing gait assessment In and Out of the laboratory". In: Proceedings of XX Annual Congress of the Italian Society for analysis of movement in the clinic (SIAMOC 2019), Bologna 2019. https://doi.org/10.1016/j.gaitpost.2019.07.493

E. Gusai, A. Zedda, M. **Caruso**, S. Bertuletti, S. Spanu, A. Pibiri, M. Monticone, A. Cereatti, D. Pani "A home-based tele-rehabilitation system for stroke patients exploiting magneto-inertial measurement units". In: Proceedings of XX Annual Congress of the Italian Society for analysis of movement in the clinic (SIAMOC 2019), Bologna 2019. https://doi.org/10.1016/j.gaitpost.2019.07.499

M. **Caruso**, A. M. Sabatini, M. Knaflitz, M. Gazzoni, U. Della Croce, and A. Cereatti "Accuracy of the orientation estimate obtained from four sensor fusion filters applied to magneto-inertial recordings of rotations performed at three different rates". In *Proceedings of XXVII Congress of the International Society of Biomechanics (ISB2019)*, Calgary 2019.

A. Cereatti, S. Bertuletti, M. **Caruso**, F. Salis "Multi-sensor integration and data fusion for enriching gait assessment In and Out of the laboratory". In *Proceedings of XXVII Congress of the International Society of Biomechanics (ISB2019)*, Calgary 2019.

M. **Caruso**, T. Bonci, M.Knaflitz, U. Della Croce, and A. Cereatti "A comparative accuracy analysis of five sensor fusion algorithms for orientation estimation using magnetic and inertial sensors". In: *Gait & Posture 66*. DOI: https://doi.org/10.1016/j.gaitpost.2018.07.114

M. **Caruso**, A. Cereatti, and M.Knaflitz "A comparative analysis of different sensor fusion algorithms for orientation estimation using magnetic and inertial sensing". In *Proceedings of International Society of Electrophysiology and Kinesiology (ISEK)*, Dublin 2018.

M. **Caruso**, A. Cereatti, and M.Knaflitz "Assessment of the performances of different sensor fusion algorithms for determining orientation using inertial and magnetic sensing". In *Proceedings of 3-D Analysis of Human Movement (3Dahm)*, Manchester 2018.

M. **Caruso**, M.Knaflitz, and A. Cereatti "An innovative MIMU-based procedure for the estimate of the knee flexion-extension angle". In *Proceedings of Sixth National Congress of Bioengineering (GNB)*, Milan 2018.